Spin-dependent electrical and thermal transport in magnetic tunnel junctions

by

Zhaohui Zhang

A Thesis submitted to the Faculty of Graduate Studies of
The University of Manitoba
in partial fulfillment of the requirements of the degree of

Doctor of Philosophy

Department of Physics and Astronomy
University of Manitoba
Winnipeg

Thesis advisor

Can-Ming Hu

Author

Zhaohui Zhang

Spin-dependent electrical and thermal transport in magnetic tunnel junctions

Abstract

As thermoelectricity can directly convert a temperature difference to a voltage or a charge current, research in this area has been very active. Recently, the development of spin caloritronics introduced spin as another degree of freedom into traditional thermoelectrics. This discovery bodes a new generation of magnetic random access memories (MRAMs), where thermal spin-transfer torque (TSTT) rather than spin-transfer torque (STT) driven by a dc voltage is used to switch the magnetization in magnetic tunnel junctions (MTJs). Involved in the rising trend of spin caloritronics, the coupling of charge, spin, and heat flow during electron transport in MTJs was systematically studied in this thesis.

The static transport properties of MTJs was studied by modeling current dependent tunnel magnetic resistance (TMR). The experimentally observed decrease of TMR with bias current is attributed to the change of spin polarization of the free ferromagnetic layer. Without going deeply into the details of the tunneling process and the interface properties, a phenomenological model has been built based on the current dependent polarization, which well explains our experimental results for MTJs with different dimensions and at various temperatures.

Next, the dynamic transport properties were studied and the Seebeck rectification effect in MTJs was revealed. By applying a microwave current to MTJs, an intrinsic thermoelectric coupling effect in the linear response regime of MTJs was discovered. This intrinsic thermoelectric coupling contributes to a nonlinear correction to Ohm's law and exists even in the linear response regime, where the charge and heat current is driven by the first order of driving forces (i.e. the gradient of electrochemical potential and the gradient of temperature). This nonlinear correction enables a novel Seebeck rectification effect. In addition, this effect can be controlled magnetically since the Seebeck coefficient is related to the magnetization configurations.

Then, TSTT was systematically studied. Here, a laser heating technique was employed to induce a temperature difference across the tunnel barrier and the ferromagnetic resonance spectra were measured electrically through spin rectification. By analyzing the evolution of the ferromagnetic resonance (FMR) spectra under temperature differences, evidence for the existence of a TSTT in MTJs was observed. It is found that the sum of the in-plane and the out-of-plane components of TSTT is proportional to the temperature difference. Additionally, the angular dependence of TSTT was found to be different from the dc-biased STT. Also, the generalized Landau-Lifshitz-Gilbert equation was solved by including STT, and the calculation well explained our experimental observations.

The discovery in Seebeck rectification refines the previous understanding of magneto-transport and microwave rectification in MTJs and provides a new possibility for utilizing spin caloritronics in high-frequency applications. The study of TSTT in MTJs shows clear experimental evidence of TSTT in MTJs. Further optimization of the

design of MTJs may succeed in decreasing the necessary switching fields strength or even achieve a switching by only TSTT in MTJs.

Contents

List of Figures

Acknowledgments

Firstly, I would like to thank my advisor, Dr.Can-Ming Hu, for the ample time he has paid for my research and career. He is an outstanding physicist. It is his professional guidance and excellent teaching that has lead me to complete this thesis.

Next, I would like to thank Dr.Yongsheng Gui, who is a very kind and considerate person. I have learned so much from him since the first day I came to the lab. During the last period of my Ph.D., he helped me a lot in thesis writing and defense preparation. He is a person who can always give me inspiring and helpful advice. In the most difficult time during my Ph.D., he gave me tremendous amount of help and encouragement.

I would also like to thank Dr. Lihui Bai. I have learned multiple experimental and data analysis skills from him, which are crucial bricks for my Ph.D. degree and future career. I will always remember these.

Furthermore, I would like to acknowledge Dr. Gwyn Williams, Dr. Byron Southern, Dr. Arkady Major and Dr. Mingzhong Wu as my thesis committee. I would also like to thank the Department of Physics and Astronomy at the University of Manitoba for their general support during my graduate studies. Especially, thanks to Ms. Susan Beshta and Ms. Wanda Klassen for their support.

I would also like to acknowledge Dr. Desheng Xue and Dr. Xiaolong Fan for introducing me to join the dynamic spintronics group here.

I would like to thank Sandeep Kaur, Alex Reimer, Paul Hyde, Michael Harder, and Christopher Dyck, for their help in language polishing. Their help made Dr. Major, one of my committee members to say that he enjoyed reading my thesis as if he was reading a novel.

I would like to acknowledge the useful and inspiring discussions I had with Dr. Gerrit E. W. Bauer, Dr. Jiang Xiao, Dr. Hong Guo, Dr. Xiaobin Chen, Dr. Simon Hemour, Dr. Lei Fu, Dr. Yangping Zhao, Dr. Bimu Yao, Dr. Jiandong Wu, Jinwei Rao and Yutong Zhao, as well as all of the people mentioned above.

I would also like to thank the support from China Scholarship Council and University of Manitoba Graduate Fellowship.

I am extremely grateful to my parents for their constant love and support, they taught me the most important lessons of my life, which made me what I am today. Without them, I might have never accomplished this achievement. I would also like to thank my beloved wife, Chen. She is a beautiful angel who came to my life and stood by my side to support me through all the difficult and struggling times.

Last but not the least, I would like to thank all my friends for being considerate and supportive.

To My Beloved Parents and Wife.

Chapter 1

Introduction

Magnetism, which originates from the spin of the electrons or nuclei, involves physical phenomena mediated by magnetic fields. The magnetic properties of lodestones, rocks rich in iron oxide Fe_3O_4, were first addressed in 600 BC by a Greek philosopher Thales of Miletus. It was also claimed that the Chinese used a magnetic device, referred to as the 'directional spoon', as a compass sometime before 2500 BC. [1, 2]. As a venerable subject, the central concepts of magnetism, such as hysteresis, were discovered by Sir James Alfred Ewing who attempted to describe the behavior of magnetic materials around 1890. Hysteresis results from the existence of multiple stable states in the absence of any external applied magnetic field and laid the foundation for modern digital recording technology, such as hard disk drives (HDDs). HDDs have been widely used for data storage and have experienced an enhancement in their data storage capacity by a factor of a million. This can be seen from the first HDD (IBM 350 disk storage unit) developed in 1956 [3], which had the capacity to store 3.75 megabytes of data, to the most modern version, which has the capacity of

10 terabytes [4].

Although both charge and spin are inherent properties of electrons, spin has been neglected for a long time. This picture began to change in the late 1980s, when the observation of spin-polarized electron injection from a ferromagnetic metal to a normal metal was achieved by Mark Johnson and R. H. Silsbee [5]. In addition, the discovery of giant magnetoresistance (GMR), offered a method to generate and manipulate spin current efficiently. The early ideas of GMR effect can be traced back to Mott in the 1930s [6], and the GMR effect has been studied in bulk nickel in 1968 [7]. The GMR effect has been re-attracted people's attention since the discoveries of GMR effect independently by Albert Fert et al. on Fe/Cr(001) multilayers [8] and Peter Grünberg et al. on Fe/Cr/Fe(001) trilayers [9]. GMR effect triggered the emergence of *spintronics* (meaning spin transport electronics). The development of *spintronics* generated novel nano-structured spintronic devices based on the interaction between magnetization dynamics and charge currents. Among these devices, magnetic tunnel junctions (MTJs) are one of the most important structures and are currently widely used for read-heads of HDDs and non-volatile magnetoresistive random-access memories (MRAMs). Instead of using the charge properties as done by semiconductor memory devices, MRAM uses magnetic hysteresis to store data and magnetoresistance to read data. It combines non-volatility, relatively high read and writing speeds, and unlimited endurance. Therefore, MRAM is believed to eventually become a universal memory technology [10–12].

Magnetoresistance (MR) is a key property of magnetic devices. It is defined as $\Delta R/R = (R_{max} - R_{min})/R_{min}$, where R_{max} and R_{min} are the maximum and minimum

resistance values respectively, controlled by an external magnetic field. MR in ferromagnetic materials can be traced back to 1851 when William Thomson discovered the anisotropic magnetoresistance (AMR) by varying the magnetization direction using an external magnetic field. The value of AMR in that study was around 5 % [13]. In 1991 IBM adapted the AMR effect for read heads, resulting in a rapid increase in the rate of storage area density of HDDs by up to 60 % per year [14]. In the 1980s, the advancement in technology for structuring materials within a nanoscale size made spin-dependent electron transport become more significant. This is because the mean free path of spins is from several nanometers to tens of nanometers in thin metallic layers.

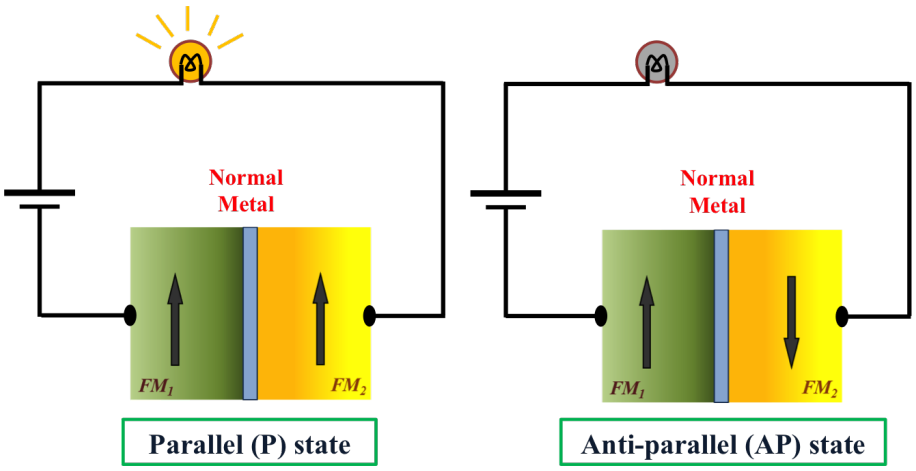

Figure 1.1: Sketches of the two magnetization configurations of a spin-valve.

Figure 1.1 illustrates the GMR effect in a ferromagnetic (FM)/non-magnetic/FM metal sandwiched structure (also known as a *spin valve*), with a thickness of approximately a few nanometers. The magnetizations of two FM layers can be aligned in either a parallel (P) state or an anti-parallel (AP) state, resulting in either a smaller

resistance (R_P) or a larger resistance (R_{AP}) respectively, because of spin-dependent scattering. To quantitatively understand the GMR effect, comprehensive theories including interfacial scattering and quantum confinement of electrons in the layers must be taken into account [15, 16]. The two magnetization states in GMR devices can be used for data storage, corresponding to two-bit states 0 and 1, and thus have a potential for building MRAM. Spin-valve based MRAM was developed in the late 1990s [11] but was not widely used, possibly because that the low metallic resistance as well as the low MR (approximately 10 %) can not be easily adapted to CMOS electronics [17].

In contrast to a full metallic GMR device, a magnetic tunnel junction (MTJ) replaces the non-magnetic metallic spacer layer with a thin ($1 \sim 2$ nm) non-magnetic insulating layer. The intrinsic high resistance (with resistance area products above $1\ \Omega \cdot \mathrm{cm}^2$) of an MTJ is more easily adaptable to nano-electronics, and thus allows the development of MRAM. In 2006, Freescale (which started as a division of Motorola, and later spun-off into EverSpin) provided the first commercialized MRAM (approximately 25 bits per chip) and was voted 'Product of the Year' by Electronics Products Magazine in January of 2007, demonstrating the potential of MRAM in the data-storage market.

Again, the tunneling magnetoresistance (TMR) property of MTJs is not brand new, as it was originally discovered in 1975 by M. Julliere [18] in Fe/Ge/Co junctions at 4.2 K with a relatively low change of resistance (approximately 14 %) and thus did not attract much attention. The impact of MTJs on storage applications only appeared after the beginning of the 21st century when crystalline magnesium oxide

(MgO) was developed for tunnel barriers. MgO-based MTJs have higher TMRs than other MTJs since MgO filters the tunneling electrons with a particular symmetry, which are fully spin-polarized within the current flow across the FM layer. Thus in the P state electrons of this symmetry dominate the tunneling current, resulting in a low resistance. By contrast, in the AP state, the channel corresponding to this symmetry is blocked, such that electrons with the next most favorable symmetry dominate the tunneling current, resulting in a high resistance [19, 20]. The observed room-temperature TMR was as great as 600 % [21] and the theoretically predicted value can be up to 10,000 % [22].

In the first-generation of MRAM commercialized in 2006, a local magnetic field was used to switch the magnetic states of MTJs for writing information. The requirement of conducting wires not only increased the difficulty of circuit integration but also limited the achievable densities and downscaling. This is a result of the limitation in current density of around 10^7 A/cm^2 due to electromigration, which is a gradual movement of ions in a conductor due to the momentum transferred from conduction electrons [23, 24]. Although novel technologies such as thermally assisted magnetization switching [25, 26] and microwave-assisted magnetization switching [27, 28] could decrease writing currents, they can not completely suppress the need for magnetic fields to switch the magnetization.

A breakthrough was achieved and generated the second generation of MRAM by adapting the concept of spin-transfer torque (STT). STT is an effect in which spin-polarized current acts on the magnetization of the free layer in an MTJ and switches the magnetization in the free layer by transferring angular momentum from the cur-

rent. This was considered theoretically for the first time in 1978 [29, 30]. In following experimental work, a current of up to 45 Ampere was required to observe the STT in millimeter scale samples [31, 32], which delayed future work in this area. With the rapid development of nanotechnology since the early 1990s, nanometer scale samples guaranteed high current density for an STT large enough to affect the magnetization in magnetic materials. In 1996, Slonzwski [33] and Berger [34] independently rediscovered STT, proposing that the STT could reorient or even reverse the magnetization in magnetic multilayer structures. Measurements of the magnetization reorientation [35, 36] and switching [37, 38] by an *in-plane* (lies in the FM layer's plane) STT in magnetic multilayers were quickly achieved. Besides the *in-plane* STT, Edwards et al. [39] and Zhang et al. [40] predicted the existence of the *out-of-plane* (perpendicular to the FM layer's plane) STT in metallic spin-valves. This torque was ignored previously since it is much smaller than the *in-plane* torque in traditional metallic spin-valves [39, 40], however, the strength of the *out-of-plane* torque can be as large as 30 % of the *in-plane* torque in MTJs [41, 42]. In 2007, for the first time, Sankey quantified both the components of STT in an MTJ by analyzing the ferromagnetic resonance (FMR) spectra and measuring a significant perpendicular component of STT with a bias voltage [41]. This quantitative understanding of STT was important for the development and optimization of STT-based MRAM.

Since 2007, the research and development of MRAM have been moving towards STT-based MRAM, which has two major advantages compared to the first generation of MRAM. The one is that the MRAM element structure can be scaled down to as small as 100 nm due to the removal of wires for inducing a magnetic field for

magnetization switching. The other advantage is that by using the same amplitude of the current, the generated STT, which is based on a quantum exchange interaction between spin current and local magnetization, is orders of magnitude stronger than the induced magnetic field. When I started my Ph.D. thesis in 2011, companies were racing to commercialize the STT-based MRAM. In November 2012, Everspin unveiled a 64Mb STT-based MRAM. To reduce the critical current density for magnetization switching, many efforts were made including the optimization of the composition of the multilayers in MTJs [43], and/or fabrication of MTJs with magnetization perpendicular to the films [44]. Overall, STT-based MRAM requires much less write current than the first generation of MRAM. However, a critical current density of up to 10^6 to 10^7 A/cm^2 is still required to produce an STT strong enough for magnetization switching [43, 44]. Encouraged by the emerging technology of *spin caloritronics* [45], dealing with the coupling of charge, spin, and heat currents in electron transport in (mostly) magnetic structures and devices, researchers are contemplating about the next generation of MRAM, where a thermal spin-transfer torque (TSTT) is used for switching the magnetization.

TSTT is an STT generated by a temperature gradient, which is one of the most exciting effects in the newly emerging field named *spin caloritronics* [45]. The pioneering work in *spin caloritronics* was done in the late 1980s by Mark Johnson and R. H. Silsbee [5]; they studied the principle of the spin-related charge and thermal transport properties based on the methods of non-equilibrium thermodynamics. The recently invigorated field of *spin caloritronics* focuses on the interaction of spins with heat currents [45] and predicated new concepts and phenomena [46–60].

In 2007, Hatami et al. predicted that a temperature gradient would induce an STT which could excite a magnetic precession [55]. Later, it was predicted that a temperature gradient of 0.2 K/nm could work efficiently as a charge current density of 10^7 A/cm^2 for re-orientating a magnetization in typical permalloy structures [56], indicating the potential of using TSTT for magnetic switching in ferromagnetic materials. In 2011, Jia et al. theoretically predicted that the TSTT may be very large in a 3 monolayer MgO-based MTJ, and found that TSTT is dependent on the relative angle of the magnetization between two FM layers in MTJs [61], which is sensitive to the thickness and the roughness of the tunneling barriers [57]. In contrast to many theoretical works, there are few experimental observations of TSTT in multilayer magnetic structures possibly due to the limited understanding of TSTT and technical difficulties. The first evidence of TSTT was observed by Yu et al. in 2010 on Co/Cu/Co spin valves by studying shifts of the FMR peak positions induced by TSTT [58]. The observation of TSTT in the same system was followed by Fitoussi et al., where they observed magnetoresistance changes due to out-of-equilibrium magnetization under TSTT [59]. Recently, Pushp et al. observed that STT would affect the switching fields of MTJs when the magnetization switched from an AP to a P state, but would not when the magnetization switched back. The reason behind this thermal torque was attributed to the asymmetry of the resistance of MTJs at positive and negative dc voltage biases [60]. However, the relationship of TSTT with local temperature gradients across the barrier or the magnetization configuration remains to be understood, preventing the application of TSTT for the next generation of MRAM. Thus, a systematic study of the behavior of TSTT as well as the related

spin-dependent thermoelectric properties is clearly needed.

One of the goals of this thesis is to bridge the present gap between the theoretical prediction for and the experimental observation of TSTT in MTJs. A comprehensive experimental system was designed to achieve this goal. This system combines the abilities of magnetization precession generation, local temperature gradient control, magnetization configuration adjustment, and electrical spin dynamics detection. Specifically, to study TSTT, magnetization precession is generated by a microwave current; then a TSTT is applied by local laser heating; finally, the impact of TSTT on the spin dynamics is electrically detected, by sweeping the magnetic field, based on the spin rectification effect. Here the spin rectification effect converts an ac signal to a dc signal via spin dynamics, i.e., a coherent nonlinear coupling between a microwave current and an oscillating resistance due to magnetization precession. The Dynamic Spintronics group at the University of Manitoba is the leading research group in the field of electrical detection of FMR [62–64], which benefited this thesis research by providing advanced experimental methods.

My Ph.D. research began after joining the Dynamic Spintronic group in 2011. Motivated by the rapid development in the area of coupling of charge, spin, and heat current, this research focused on the study of spin related charge and thermal transport properties in nano-devices, and mainly researched the following issues:

Current dependent magnetoresistance [65]:

The fact that TMR of an MTJ will decrease with an applied current has been observed experimentally [66–69]. This behavior is described by various approaches such as interface spin excitation [70], a reduced polarization for hot electron states and

spin dependent wave-vector mismatch [71], and defects in MTJ tunnel barriers [72]. These approaches consider the physical characteristics of the barrier and interfaces, which are complicated, and vary sample to sample. As a preparation for studying the dynamic thermoelectrical effect and TSTT in this thesis, the current dependent magnetoresistance of MTJs was studied in chapter 4. In addition, a phenomenological model was introduced, which well explains the experimental data.

Spin-dependent Seebeck rectification effect [73]:

Spin-dependent Seebeck effects in MTJs subjected to external heating and the static thermoelectric response have been recently studied [50, 52]. In these studies, the MTJs can be characterized by an absolute thermal power which can be magnetically controlled. Based on these studies and with the insight from the study of intrinsic thermoelectric transport in a metal performed by William Thomson, the current work investigated the Seebeck rectification effect in MTJs enabled by the localized Joule heating. It also investigated the intrinsic spin-dependent thermoelectrical transport in MTJs carrying a tunneling current in the absence of external heat sources, which leads to a nonlinear correction to Ohm's law.

Thermal spin-transfer torque [74]:

Systematic studies of TSTT in MTJs were also made by electrical detection of the FMR spectra. Similar to dc-biased STT [41], TSTT also adjusts the FMR line shapes. By studying the FMR line shapes and comparing the results with the effects of dc-biased STT, the differences of TSTT and dc-biased STT were revealed. This work presented evidence for the existence of TSTT in MTJs and provides the possibility of achieving magnetization switching by using TSTT in MTJs. It was also demonstrated

that the electrically detected FMR can be used as a sensitive tool for the measurement of TSTT in MTJs, making this work of general interest to the spintronics community.

Overall, my thesis presents a systematic study and comprehensive understanding of the coupling of charge, spin, and heat flows in nano-structured MTJ devices. Particularly, it was found that Joule heating induced by a microwave current produces a Seebeck rectification voltage. This observation has been successfully used for microwave imaging [75] and energy harvesting [76]. For the first time, TSTT at the FMR condition was systematically studied using the newly developed electrical detection technique. In addition, the difference between TSTT and dc-biased STT was demonstrated. The results indicate that the interplay among coupling, spin, and heat flows not only offers several novel methods for manipulating and detecting magnetization in MTJ devices, but also paves the way for utilizing spin caloritronics devices for high-frequency applications.

The following part of this thesis is organized as follows:

Chapter 2 provides the background theories related to this thesis.

Chapter 3 contains the composition of our MTJ structures and the experimental setups.

Chapter 4 focuses on the dc current response of TMR and resistance of MTJs.

Chapter 5 discusses the Seebeck rectification effect in MTJs.

Chapter 6 includes the study of thermal spin-transfer torques in MTJs.

Chapter 7 is the conclusion and possible future work.

Chapter 2

Background and theory

In order to understand the unique spin-dependent thermoelectric transport in magnetic tunnel junctions (MTJs), a brief discussion of the interplay of spin, charge, and heat current in nanostructure MTJ devices will be provided in the first section of this chapter with the focus on static properties. Starting from the two current model, the origin of the tunnel magnetoresistance (TMR) effect is explained. Here, the magnetoresistance and TMR ratio are determined by the spin-dependent tunneling possibilities, which are related to the electron density of states near the Fermi level for different spin states in the ferromagnetic (FM) layers. Similar to the TMR effect, the Seebeck coefficients in MTJs are also spin-dependent, as it is determined by the log-derivative of conductivity to energy at Fermi energy according to Mott's formula [77].

We then move to dynamics properties in MTJs under a microwave current, where ferromagnetic resonance (FMR) is a sensitive tool for studying spin-transfer torque (STT) [41, 74], since the effect caused by STT is magnified when resonance occurs.

Section 2 of this chapter provides a detailed discussion of FMR in MTJs based on the Landau-Lifshitz-Gilbert (LLG) equation, which describes the precessional motion of magnetization in an FM material. First, the conventional FMR measurement for a single FM layer excited by an oscillating magnetic field is considered; subsequent focus is on the solution of the generalized LLG equation in an MTJ, where the FMR is mainly excited by a microwave current. The results show that the magnetization precession in an MTJ is dependent on both the in-plane and out-of-plane STTs.

Historically, three generations of techniques for FMR detection have been developed, while each technique has its own advantages and disadvantages. In the last section of this chapter, a brief discussion of the evolution of these techniques is presented. In this thesis, the technique of electrical detection of FMR is employed in the nano-scale samples, as the measured dc voltage in this technique is not determined by the size but the resistance of the sample. It is also shown that STT can be quantitatively measured by carefully analyzing the FMR line shape detected electrically [41, 74].

2.1 Static transport properties in magnetic tunnel junctions

2.1.1 Spin-dependent charge transport properties in MTJs

TMR is one of the most basic properties of MTJs, which implements the application of MTJs in read heads of hard disks and non-volatile memories [78–84].

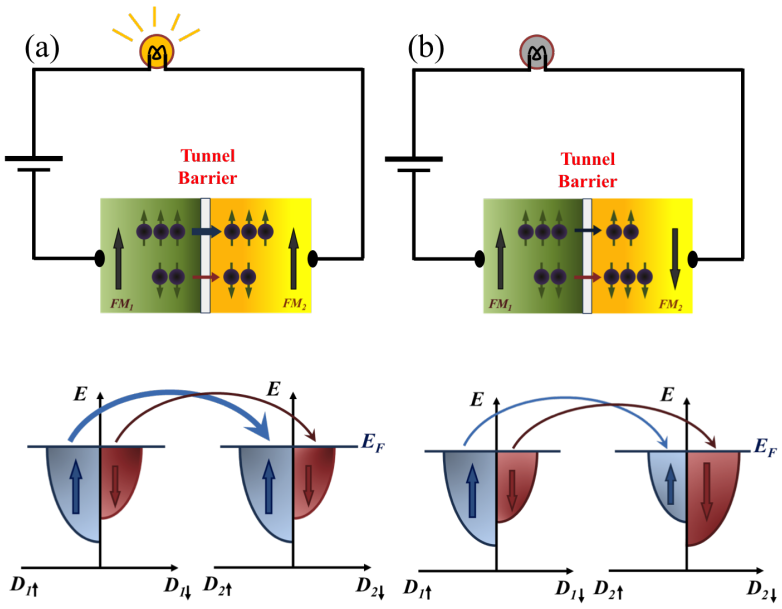

Figure 2.1: Schematic figures of the spin-dependent transport in an MTJ. Electrons can only tunnel to the sub-band of the same spin direction. The conductance of an MTJ is proportional to the tunneling possibility, which is proportional to the product of electron density of states (D) in the two FM layers. A change from (a) the parallel configuration to (b) the antiparallel configuration results in an exchange of the spin-up and spin-down sub-band, and thus the conductance of parallel configuration is larger than the conductance of anti-parallel configuration.

Jullière adopted the two current model to describe the TMR effect [18]. The basic idea of this model is that the total conductance is the sum of two parallel conductances for spin-up and spin-down electron channels, respectively. Here, the two spin-dependent channels are assumed to be independent of each other.

Schematic figures of the TMR mechanism based on the two current model are shown in Fig. 2.1. D is the electron density of states near Fermi energy level E_F. E_F is the highest energy at absolute zero temperature at which the electrons exist in quasi-continuous electronic states. The subscripts $\uparrow$ and $\downarrow$ denote spin-up and spin-down, respectively, and 1 and 2 denote the first and second FM layers, respectively.

Jullière's theory shows that the tunneling possibility is proportional to the product of D in the two FM layers. For the P state, the tunneling possibility is proportional to $D_{1\uparrow}D_{2\uparrow} + D_{1\downarrow}D_{2\downarrow}$, and for the AP state, the tunneling possibility is proportional to $D_{1\uparrow}D_{2\downarrow} + D_{1\downarrow}D_{2\uparrow}$. The tunneling conductance of P (G_P) and AP (G_{AP}) states are $G_P = G_{\uparrow\uparrow} + G_{\downarrow\downarrow} \propto D_{1\uparrow}D_{2\uparrow} + D_{1\downarrow}D_{2\downarrow}$ and $G_{AP} = G_{\uparrow\downarrow} + G_{\downarrow\uparrow} \propto D_{1\uparrow}D_{2\downarrow} + D_{1\downarrow}D_{2\uparrow}$, respectively. Here spin-up is the majority state, thus $D_{1\uparrow}D_{2\uparrow} + D_{1\downarrow}D_{2\downarrow}$ is larger than $D_{1\uparrow}D_{2\downarrow} + D_{1\downarrow}D_{2\uparrow}$, resulting in a greater electrical resistance in the AP state compared to the P state. Then,the TMR ratio η can be written as

$$\eta = \frac{G_P - G_{AP}}{G_{AP}} = \frac{(D_{1\uparrow}D_{2\uparrow} + D_{1\downarrow}D_{2\downarrow}) - (D_{1\uparrow}D_{2\downarrow} + D_{1\downarrow}D_{2\uparrow})}{(D_{1\uparrow}D_{2\downarrow} + D_{1\downarrow}D_{2\uparrow})}. \tag{2.1}$$

The spin-polarization is defined as $P_S \equiv \frac{D_\uparrow(E_F) - D_\downarrow(E_F)}{D_\uparrow(E_F) + D_\downarrow(E_F)}$. Then the TMR ratio strongly depends on the spin-polarization of both FM layers as

$$\eta = 2P_{S1}P_{S2}/(1 - P_{S1}P_{S2}). \tag{2.2}$$

In the P or AP state, the relative angle, θ, of the two magnetizations in the two FM layers is 0 or 180 °. When θ is between 0 and 180 °, the conductance of an MTJ is in the ranging between G_P and G_{AP}, and the corresponding resistance is in the ranging between R_P and R_{AP}. Here, R_P and R_{AP} are the resistance at P and AP state, respectively. The resistance of an MTJ ($R(\theta)$) is proportional to $\cos\theta$ as [85, 86]

$$R(\theta) = \frac{1}{2}(R_P + R_{AP}) + \frac{1}{2}(R_P - R_{AP})\cos\theta. \tag{2.3}$$

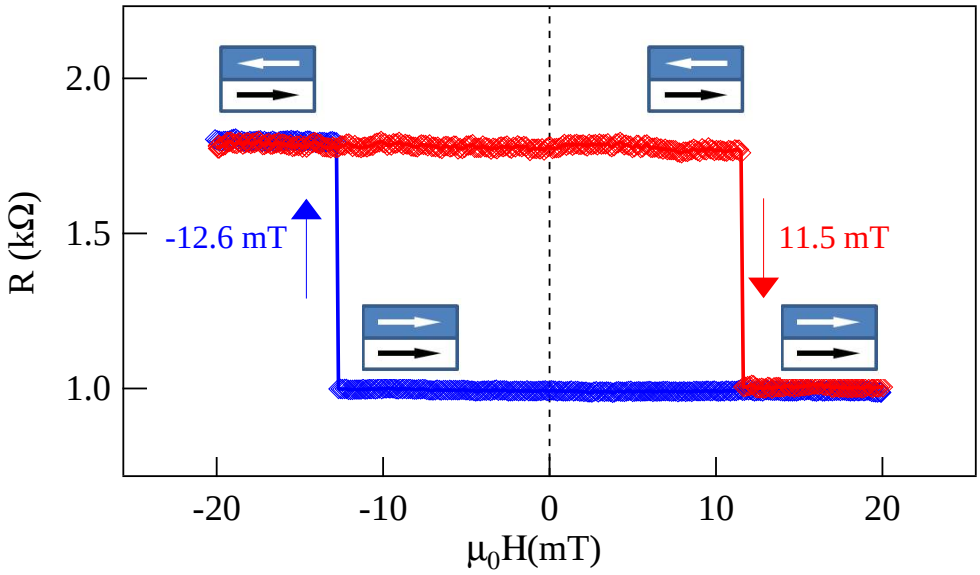

Figure 2.2: A typical resistance loop of one of the MTJs measured at room temperature with a bias current of 1 μA.

In a MgO-based MTJ, the magnetization of one FM layer is pinned by an antiferromagnetic (AFM) layer via exchange interaction, resulting in a larger coercivity force compared to the other FM layer. Correspondingly, the FM layer pinned by an AFM layer is called the *fixed layer* and the other FM layer is called the *free layer*. Figure 2.2 shows a resistance loop of one of the MTJs measured by sweeping the external magnetic field H. At a larger negative value of H, the magnetizations of the two FM layers are in an AP state. By increasing H, at 11.5 mT, the magnetization of the free layer reverses, while the direction of the magnetization of the fixed layer remains the same, resulting in a P state. When H is swept from a positive to a negative value, the reversal of the free layer magnetization occurs at -12.6 mT. The difference between the positive and negative coercivity forces is due to the bias exchange interaction between the two FM layers [87].

2.1.2 Spin-dependent Seebeck effect in magnetic tunnel junctions

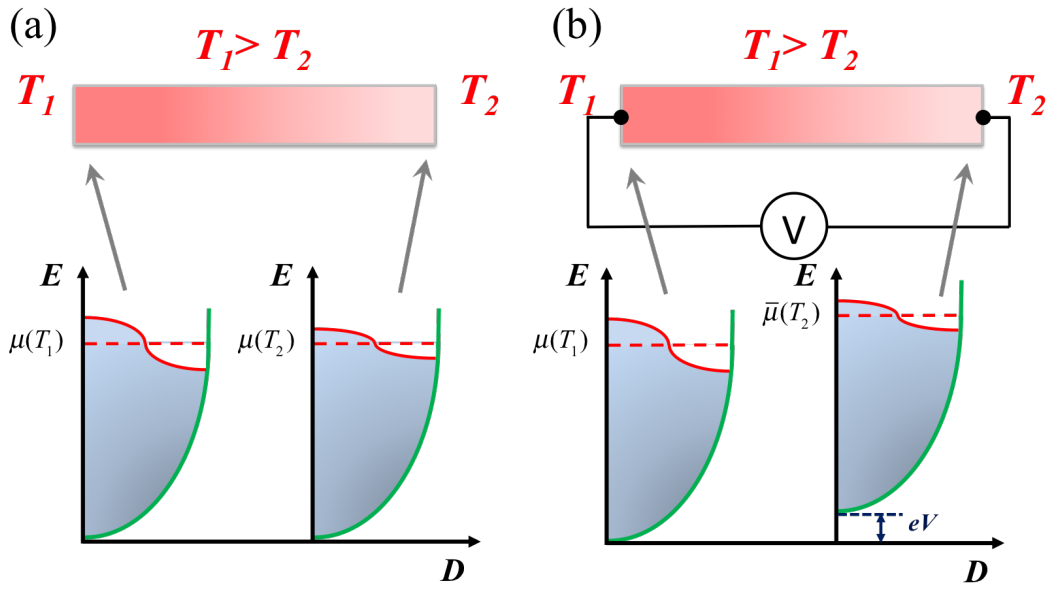

Figure 2.3: The density of states as a function of energy at the two ends of a metallic conductor (a) before and (b) after equilibrium.

The Seebeck effect results from a conversion of a temperature difference to a dc voltage signal. This conversion is caused by a change of the Fermi-Dirac distribution for electrons in materials due to a temperature difference [88]. At a given temperature T, the possibility ($f(E)$) of electron occupation of an energy state (E) is governed by the Fermi-Dirac distribution function $f = 1/(1+e^{(E-\mu_C)/k_BT})$. Here, k_B is Boltzmann constant, μ_C is the electron charge chemical potential and is defined as the required energy to add or remove an electron from a system at a given temperature at zero electrostatic potential V. In a free-electron metal, the chemical potential is calculated

as [89]

$$\mu_C = E_F - \frac{\pi^2 k_B^2 T^2}{12 E_F} + \cdots, \tag{2.4}$$

where μ_C has the highest value at absolute zero temperature and decreases when the temperature increases.

As shown in Fig. 2.3(a), considered a metallic conductor, aluminum, for example, and heat one end. At the hotter end, the tail of the distribution spreads to higher energies than at the colder end. The energy of the hotter end is shown lowered in accordance with Eq. 2.4. Thus, the electrons move from the hotter to the colder end. This is actually how heat is conducted in a metal. The negative charge will then accumulate at the colder end, due to which, a potential difference V will be built between the two ends of the conductor as shown in Fig. 2.3(b). A dynamic equilibrium will be built between the electrons forced by the temperature gradient from the hotter to the colder end, and the electrostatic repulsion due to the accumulation of electrons at the colder end. Thus, the number of electrons passing through a cross section normal to the flow at a unit time in both the directions will be equal, resulting in no actual transfer of charge. At this dynamic equilibrium, the charge electrochemical potential, $\bar{\mu}_C$, defined as

$$\bar{\mu}_C = \mu - |e|V, \tag{2.5}$$

is not the same at both ends of the conductor. The voltage (V) observed here is proportional to the temperature difference (ΔT) between the two ends and can be written as

$$V = -S\Delta T, \tag{2.6}$$

where S is the Seebeck coefficient determined by the intrinsic properties of the ma-

terial. In common metals such as aluminum and copper, S is on the order of several μV/K.

In a ferromagnetic metal, the Seebeck coefficients for spin-up and spin-down channels are usually different, due to the spin-dependent transport property [5, 90]. Thus, in MTJs, the Seebeck coefficient is also related to the relative angle between the two magnetizations in the FM layers. This spin-dependent Seebeck effect in MTJ was first reported by Walter et al. [52]. It was found that in MTJs, the Seebeck coefficient may be greater than hundred μV/K. The spin-dependent Seebeck effect in MTJ not only opened a door for the application of MTJs as thermoelectricity devices [17], but also paved a way to understand spin-dependent thermoelectricity [50, 52, 91].

2.1.3 Coupling of charge, spin and heat currents in electron transport

In chapter 5, it is shown that the spin-dependent Seebeck effect can be also generated by a thermoelectrical coupling based on the Onsager's linear dependence in electron transport. In Onsager's linear dependence, the charge, spin, and heat currents are linearly driven by an electrochemical potential, a spin accumulation, and a temperature gradient.

Following the Onsager's linear dependence, the coupling of charge, spin, and heat current in electron transport was summarized by Mark Johnson [5] in 1987, and a new field called spin caloritronics (from *calor*, the Latin word for heat) emerged [45].

This coupling is described by a 3×3 matrix as [45]:

$$\begin{pmatrix} J_C \\ J_S \\ J_Q \end{pmatrix} = \sigma \begin{pmatrix} 1 & P_S & ST \\ P_S & 1 & P'_S ST \\ \Pi & P'_S ST & \kappa T/\sigma \end{pmatrix} \begin{pmatrix} \nabla \bar{\mu}_C/e \\ \nabla \mu_S/2e \\ -\nabla T/T \end{pmatrix}. \tag{2.7}$$

Here J_C, J_S, and J_Q are the charge, spin, and heat current density, respectively; $P_S = (G\uparrow - G\downarrow)/G$ and $P'_S = \partial_\epsilon(G\uparrow - G\downarrow)|_{\epsilon_F}/\partial_\epsilon G|_{\epsilon_F}$ stand for the spin-polarization of the conductivity and its energy derivative, where $G\uparrow$, $G\downarrow$ and G are the conductivity for spin-up, spin-down, and the sum of both spin-up and -down electrons, respectively; μ_S stands for the spin accumulation; Π is the Peltier coefficient; κ and σ are the thermal and electrical conductivities, respectively; S is Seebeck coefficient; and T is temperature.

The three flows on the left are driven by a linear combination of the three driving forces $\nabla\bar{\mu}_C$, $\nabla\mu_S$, and ∇T. The elements in the 3×3 matrix on the right side of Eq. 2.7 denote different physical laws and effects, which can be summarized as follows:

Ohm's law	Charge current driven by spin accumulation [5]	Normal Seebeck effect
Spin current driven by voltage [5]	Spin-dependent Ohm's law	Spin-dependent Seebeck effect [46–52]
Normal Peltier effect	Spin-dependent Peltier effect [48, 49, 53, 54]	Fourier's law

The symmetry of this 3×3 matrix is a result of Onsager's reciprocity relation [92], which links the Peltier and Seebeck coefficients as $\Pi = ST$. This relation indicates

that the Seebeck and Peltier effects are inverse effects of each other. From Eq. 2.7, a spin current can be driven by a temperature gradient, which corresponds to the spin-dependent Seebeck effect [46–52]. Also, a heat current can be driven by spin accumulation, which corresponds to the spin-dependent Peltier effect [48, 49, 53, 54]. This 3×3 matrix also provides two different methods for generating a spin current, which is applying a voltage or a temperature gradient. The injection of a spin current from an FM metal to a normal metal by these methods has been achieved since about three decades ago [5, 48, 49].

2.2 Spin dynamics in MTJs

At a certain frequency for a given external magnetic field, a ferromagnetic material strongly absorbs microwave energy. This effect is called ferromagnetic resonance (FMR). The first observation of FMR was performed by Griffiths in 1946, although he attributed his observation as a result of abnormal electron paramagnetic resonance [93]. One year after this observation, Kittel recalculated and explained Griffiths' work [94] as a result of FMR. Later, Kittel laid down the foundation of magnetization dynamics in his paper named *On the theory of ferromagnetic resonance absorption* [95].

It is a challenge to detect the FMR signal in nanostructures such as MTJs by using the traditional detection methods based on the microwave transition measurement since the magnitude of the detected signal is proportional to the size of the sample. In this thesis, a newly developed electrical detection technique is employed to measure FMR. In this section, the mechanism of FMR is briefly reviewed by solving the

Landau-Lifshitz-Gilbert (LLG) equation, and the principle of the electrical detection of FMR is also introduced.

2.2.1 Ferromagnetic resonance and the Landau-Lifshitz-Gilbert equation

Since the thickness of the FM layer of the MTJs is nanometers in scale, it is in a single domain regime, which is called the 'macro-spin approximation' [96] as shown in Fig. 2.4. Based on this approximation, the magnetization of the FM layer is treated as a uniform angular momentum $\mathbf{m}$, and the unit vector of this magnetization is defined as $\hat{\mathbf{m}} = \mathbf{m}/M_s$, where M_s is the saturation magnetization.

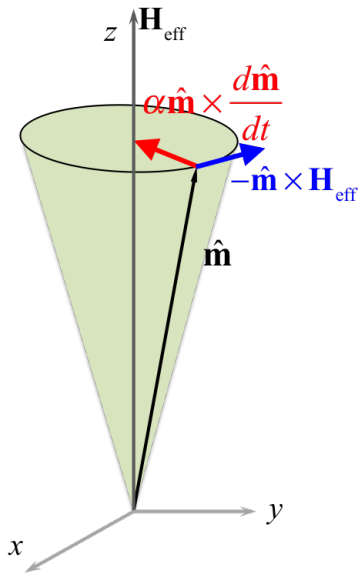

Figure 2.4: The sketch of a uniform anglar momentum precession. The effective magnetic field, $\mathbf{H}_{\text{eff}}$, is along the z direction. The magnetization vector $\hat{\mathbf{m}}$ is precessing along the direction of $\mathbf{H}_{\text{eff}}$. The directions of the field torque $\hat{\mathbf{m}} \times \mathbf{H}_{\text{eff}}$ and the Gilbert damping $\alpha\hat{\mathbf{m}} \times \frac{d\hat{\mathbf{m}}}{dt}$ are also shown on the sketch.

The LLG equation describing the precession of the magnetization of the free FM layer can be written as

$$\frac{d\hat{\mathbf{m}}}{dt} = -\gamma\hat{\mathbf{m}} \times \mathbf{H}_{\text{eff}} + \alpha\hat{\mathbf{m}} \times \frac{d\hat{\mathbf{m}}}{dt}. \tag{2.8}$$

Here α is the dimensionless Gilbert damping coefficient; γ is the absolute gyromagnetic ratio linking the magnetization with the angular momentum; and $\mathbf{H}_{\text{eff}}$ is the effective magnetic field, which is defended as $\mathbf{H}_{\text{eff}} = \mathbf{H} - \mathbf{N}\cdot\mathbf{M}$, where $\mathbf{H}$ is an external magnetic field, and $\mathbf{N}$ and $\mathbf{M}$ are the demagnetization factor and the magnetization $\mathbf{M}$ of the material, respectively.

The left side of Eq. 2.8 is the time differential of magnetization which describes the change of $\hat{\mathbf{m}}$ with time by the applied torques on $\hat{\mathbf{m}}$. These torques are listed on the right side of Eq. 2.8, where the first term is a torque produced by the effective magnetic field and the second term is the Gilbert damping. The magnetization precesses around the effective magnetic field $\mathbf{H}_{\text{eff}}$. Without a continuous torque acting on the magnetization, this precession slows down due to damping, leaving $\hat{\mathbf{m}}$ to align with the direction of $\mathbf{H}_{\text{eff}}$.

To maintain the precession of $\hat{\mathbf{m}}$, a continuous driving force is required to compete with damping. For example, a microwave magnetic field ($\mathbf{h}$-field), $\mathbf{h}$, acting as an oscillating magnetic field torque $\tau_h = -\gamma\hat{\mathbf{m}} \times \mathbf{h}$ can achieve this purpose. Usually, this oscillating h-field is much smaller than the static effective magnetic field ($|\mathbf{h}| \ll |\mathbf{H}_{\text{eff}}|$), and thus the solution of the LLG equation with microwave $\mathbf{h}$-field torque is,

$$\begin{pmatrix} m_x \\ m_y \\ m_z \end{pmatrix} = \begin{pmatrix} \chi_{xx} & i\chi_{xy} & 0 \\ -i\chi_{yx} & \chi_{yy} & 0 \\ 0 & 0 & 0 \end{pmatrix} \begin{pmatrix} h_x \\ h_y \\ h_z \end{pmatrix} = \chi_h \begin{pmatrix} h_x \\ h_y \\ h_z \end{pmatrix}. \tag{2.9}$$

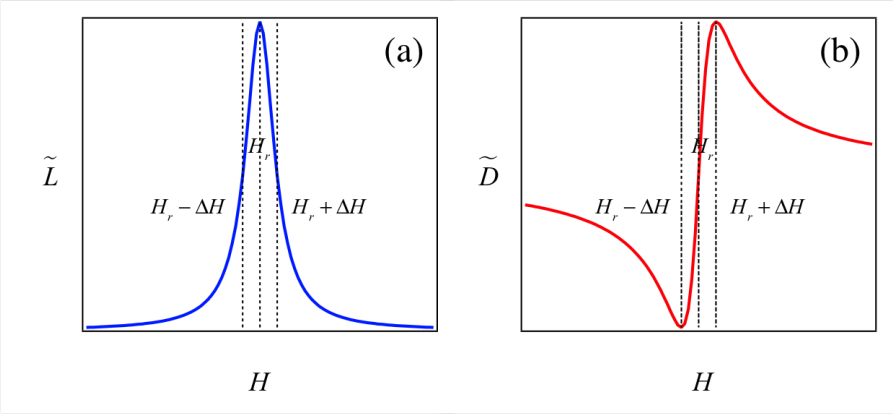

Figure 2.5: The (a) Lorentz and (b) Dispersive line shape. H_r is the resonance field and ΔH is the line width of the spectra.

The coordinate system is shown in Fig. 2.4. Here, m_i (i =x,y,z) are the three dynamic components of **m** in cartesian coordinate system; h_i are the three components of **h**; χ_h is known as the Polder tensor, which describes the dynamic response of magnetization to an alternating magnetic field. The elements of χ_h are represented as

$$(\chi_{xx}, \chi_{xy}, \chi_{yy}) = (\widetilde{D} + i\widetilde{L})(A_{xx}, A_{xy}, A_{yy}). \tag{2.10}$$

Here, $\widetilde{D}$ and $\widetilde{L}$ are defined as

$$\begin{aligned} \widetilde{D} &= \frac{\Delta H(H - H_r)}{(H - H_r)^2 + \Delta H^2}, \\ \widetilde{L} &= \frac{\Delta H^2}{(H - H_r)^2 + \Delta H^2}, \end{aligned} \tag{2.11}$$

which are asymmetric (dispersive) and symmetric (Lorentz) line shapes, respectively, as shown in Fig. 2.5. Here H is the amplitude of the external magnetic field which is applied on z direction; H_r is the resonance magnetic field; and ΔH is the line-width of FMR.

In Eq. 2.10, A_{xx}, A_{xy}, and A_{yy} are the amplitudes of the FMR, which are determined by the parameters of the samples as

$$\begin{aligned} A_{xx} &= \frac{\gamma M_s[N_y M_s + (H - N_z)M_s]}{\alpha\omega[2(H - N_z M_s) + M_s(N_z + N_y)]}, \\ A_{xy} &= -\frac{M_s}{\alpha[2(H - N_z M_s) + M_s(N_z + N_y)]}, \\ A_{yy} &= \frac{\gamma M_s[N_x M_s + (H - N_z)M_s]}{\alpha\omega[2(H - N_z M_s) + M_s(N_z + N_y)]}. \end{aligned} \tag{2.12}$$

Here, N_x, N_y, and N_z are the x, y, and z components of the demagnetization factor.

2.2.2 STT induced spin dynamics in MTJs

As discussed above, to maintain the precession of the magnetization $\hat{\mathbf{m}}$, a continuous driving force is required. In MTJs, this driving force was served by the spin-transfer torque (STT) generated by the microwave current sent into the sample.

STT is an effect on magnetization based on the exchange interaction between the spin-polarized current going through the sample and the localized spins in the magnetic material. STT has two components. One is called the in-plane STT and the other is called the out-of-plane STT. The directions of in-plane and out-of-plane are defined by $\hat{\mathbf{m}} \times (\hat{\mathbf{M}} \times \hat{\mathbf{m}})$ and $\hat{\mathbf{M}} \times \hat{\mathbf{m}}$, respectively, where $\hat{\mathbf{m}}$ and $\hat{\mathbf{M}}$ are the unit vectors of magnetizations in the free and the fixed FM layers, respectively.

The LLG equation for a vector magnetization $\hat{\mathbf{m}}$ with a STT can be expressed as [41, 97]

$$\frac{d\hat{\mathbf{m}}}{dt} = -\gamma\hat{\mathbf{m}} \times \mathbf{H}_{\text{eff}} + \alpha\hat{\mathbf{m}} \times \frac{d\hat{\mathbf{m}}}{dt} - \gamma\frac{\tau_{\parallel}(I,\theta)}{M_s}\hat{\mathbf{y}} - \gamma\frac{\tau_{\perp}(I,\theta)}{M_s}\hat{\mathbf{x}}, \tag{2.13}$$

where $\tau_{\parallel}(I,\theta)$ is the in-plane STT and $\tau_{\perp}(I,\theta)$ is the out-of-plane STT. $\hat{\mathbf{y}}$ and $\hat{\mathbf{x}}$ are unit vectors which are defined as $\hat{\mathbf{y}} = \frac{\hat{\mathbf{m}}\times(\hat{\mathbf{M}}\times\hat{\mathbf{m}})}{|\hat{\mathbf{M}}\times\hat{\mathbf{m}}|}$ and $\hat{\mathbf{x}} = \frac{\hat{\mathbf{M}}\times\hat{\mathbf{m}}}{|\hat{\mathbf{M}}\times\hat{\mathbf{m}}|}$.

By solving Eq. 2.13, we can obtain

$$\begin{pmatrix} m_x \\ m_y \\ m_z \end{pmatrix} = \begin{pmatrix} \chi_{xx} & \chi_{xy} & 0 \\ \chi_{yx} & \chi_{yy} & 0 \\ 0 & 0 & 0 \end{pmatrix} \begin{pmatrix} \frac{d\tau_\perp}{dI} \\ \frac{d\tau_\perp}{dI} \\ 0 \end{pmatrix} = \chi_\tau \begin{pmatrix} \frac{d\tau_\perp}{dI} \\ \frac{d\tau_\perp}{dI} \\ 0 \end{pmatrix}, \tag{2.14}$$

where χ_τ is the magnetic susceptibility tensor due to the STT. The elements of χ_τ are represented as

$$\begin{aligned} \chi_{xx} &= -\frac{I_{RF}}{2M_s\gamma\Delta H}(i\omega - \frac{\gamma}{M_s}\frac{d\tau_\parallel}{d\theta})(\widetilde{D} + i\widetilde{L}), \\ \chi_{xy} &= -\frac{I_{RF}}{2M_s\gamma\Delta H}(\gamma N_y M_s + \gamma H + i\alpha\omega - \frac{\gamma}{M_s}\frac{d\tau_\perp}{d\theta})(\widetilde{D} + i\widetilde{L}), \\ \chi_{yx} &= \frac{I_{RF}}{2M_s\gamma\Delta H}(\gamma N_x M_s + \gamma H + i\alpha\omega)(\widetilde{D} + i\widetilde{L}), \\ \chi_{yy} &= \frac{I_{RF}}{2M_s\gamma\Delta H} i\omega(\widetilde{D} + i\widetilde{L}). \end{aligned} \tag{2.15}$$

The observed FMR spectra are linear combinations of Lorentz and dispersive line shapes which depend on both $d\tau_\perp/dI$ and $d\tau_\parallel/dI$. Theoretical and experimental studies found that $d\tau_\perp/dI$ and $d\tau_\parallel/dI$ have different voltage dependences [41, 98–104].

$$d\tau_\parallel/dI = A_1 V + A_2 V^2, \tag{2.16a}$$

$$d\tau_\perp/dI = B_0 + B_2 V^2. \tag{2.16b}$$

Here, A_1, A_2, B_0 and B_2 are coefficients independent from the bias voltage V. Thus, a bias voltage can adjust the FMR line shape by changing $d\tau_\perp/dI$ and $d\tau_\parallel/dI$ [41, 99–104].

2.2.3 Thermal spin-transfer torque

As shown in Eq. (2.7), a spin current can be driven not only by a gradient of electrochemical potential $\nabla\bar{\mu}_C$ but also a temperature gradient ∇T. The STT driven by $\nabla\bar{\mu}_C$ is called the dc-biased STT, since it is usually achieved by applying a dc bias voltage, and the STT driven by ∇T is called the TSTT.

Hatami et al. derived an expression for the TSTT in spin valves showing that the STT generated by a voltage ΔV and a temperature difference ΔT between the two ends of a spin valve are additive and can be represented as [55]

$$\tau \propto (P_S \Delta V + P'_S S \Delta T). \tag{2.17}$$

Here, S is the Seebeck coefficient of the spin valve. The typical range of spin polarization, P_S, is from 0 to 0.6 in most magnetic materials [105, 106]. In contrast to P_S, $\mid P'_S \mid$ is not bounded, and $P'_S S$ can be very large [55], which means a small ΔT may generate a large torque. Although Hatami's expression comes from a spin accumulation model where only the in-plane torque was considered, the result that STT can be generated by ΔV and ΔT is instructive in an MTJ.

TSTT in MTJs has also been predicted by first principle calculation [61]. It was found that a 6 K temperature difference was required to switch the magnetization configuration from an AP to a P state, but an order of magnitude larger temperature difference was required to switch it back. The large TSTT for the AP state was attributed to the fact that interface states around the Fermi energy on one side of the barrier to allow multiple scattering processes [90]. Pushp et al. observed TSTT assisted magnetization switching in MTJs recently. They found that the TSTT is larger at an AP state than the TSTT at a P state [60]. Arnab et al. observed the

field-like component of TSTT in MTJs by measuring ΔT dependent magnetization switching and also found that the TSTT is larger at an AP state than the TSTT in a P state [107].

The theory of TSTT is still in development. In chapter 6, a detailed discussion about TSTT will be presented both in theory and experimental observation.

2.3 Electrical detection of spin dynamics in MTJs

Three generations of FMR measurement technologies have been developed to date [62, 108, 109]. The first and the second generations of FMR measurement technologies measure the power of the absorbed or transmitted microwave. In the first generation of FMR measurement technology, the sample was put inside a microwave cavity, and the cavity was placed in a magnetic field. By monitoring the signal as a function of the external magnetic field, the spin dynamics properties of the sample were studied. This technology has been commercialized by Bruker and has been widely used for studying the spin dynamics in bulk materials and thin films [108]. However, a limitation of this technology is that it is difficult to study the FMR dispersion as a function of microwave frequency and magnetic field since the frequency range of the cavity is limited.

The second generation of FMR measurement technology combined a coplanar waveguide (CPW) and a vector network analyzer (VNA) [109]. A CPW is fabricated using a printed circuit board with ground-signal-ground lines, where the microwave current can transmit through the signal line. A VNA can be used to precisely measure both the magnitude and the phase of scattering parameters (S-parameters). Since

the energy lost in the transmission line is very sensitive to the ambiance, careful calibration is required before each measurement. This, as well as the high price of a VNA, hampers the possibility of wide use of the second generation of FMR measurement technology.

In the first and second generation of FMR measurement technologies, the signal is proportional to the size of the samples. Thus, it is a challenge to use these techniques to study dynamic properties of single magnet nanostructures such as MTJs.

In this thesis, electrical detection of FMR (EDFMR) is used to study spin dynamic properties in MTJs, which is based on the spin rectification effect. Spin rectification effect was performed for the first time by Juretschke in the early 1960's [110, 111], and was rediscovered four decades later [62, 112]. EDFMR is a sensitive method which can be used to detect FMR on micro/nanometer scale samples [62, 113]. In EDFMR, the sample and CPW are integrated on a chip by micro/nanofabrication technology, and the spin dynamic properties are measured by a dc voltage across the FM samples directly. In principle, this voltage is caused by the coupling of the microwave current and the periodical magnetoresistance change of the sample. Thus, the measurement does not depend on the size of the samples, but the sensitivity is determined by the magnitude of magnetoresistance. In addition, the lock-in technique is used, which enhances the sensitivity of the measurement to 10 nV.

2.3.1 Principle of electrical detection of FMR

In general, rectification is the process by which a dc signal is produced by two coupled alternating signals with the same angular frequency, ω, based on the fact that

$\cos(\omega t)\cos(\omega t+\phi) = \frac{1}{2}\cos\phi + \frac{1}{2}\cos(2\omega t+\phi)$. Here, ϕ is a relative phase between the two signals. A non-zero time-independent term $\frac{1}{2}\cos\phi$ exists when $\phi \neq n\pi/2$ ($n = \pm1, \pm3, \pm5..$).

In the spin rectification effect, the two alternating signals are a microwave current and an oscillating resistance. Specifically, the resistance of an MTJ is determined by the relative angle (θ) between the two magnetizations. When a microwave current is sent into an MTJ, the magnetization of the free layer is oscillating with the same frequency as that of the microwave current. Supposing the microwave current is $I_{RF}\cos\omega t$, where I_{RF} is the amplitude and ω is the angular frequency, angle θ is driven to oscillate with a small correction $\delta\theta(t)$ as $\theta+\delta\theta$. By Taylor expanding Eq. 2.3 to the first order of θ , the oscillating resistance is derived as $R(\theta) = \frac{1}{2}(R_P+R_{AP}) + \frac{1}{2}(R_P - R_{AP})(\cos\theta - \sin\theta\delta\theta)$. By solving the LLG equation, we obtained $\delta\theta \approx -\mathrm{Re}(m_y)$ as shown in Eq. A.5 in appendix A. Thus, the dc rectification voltage, V_r, is derived by calculating the time average of $I_{RF}\cos\omega t \cdot R(\theta)$. Since the microwave current and m_y are in phase in MTJs [63], the rectification voltage V_r is obtained as $\frac{1}{4}I_{RF}(R_P - R_{AP})|m_y|\sin\theta$, from which, one can see that V_r is related to the amplitude of the microwave current, the magnetoresistance, the relative angle of two magnetizations, and the dynamic magnetization at y direction.

2.3.2 Rectification voltage in MTJs

The y component of the dynamic magnetization can be derived from Eq. 2.14 as (see the appendix A for details) [41, 97]

$$m_y = -\frac{I_{RF}}{2M_s}\frac{\sqrt{1+M_0/H_r}}{(H-H_r+i\Delta H)}\left[\sqrt{1+M_0/H_r}\left(\frac{d\tau_\perp}{dI}\right) + i\left(\frac{d\tau_\parallel}{dI}\right)\right], \tag{2.18}$$

where $M_0 \equiv (N_x + N_y)M_s \approx N_x M_s$. Then the rectification voltage V_r is represented as

$$\begin{aligned} V_r &= \frac{I_{RF}^2}{4M_s}(R_P - R_{AP})\sin\theta\sqrt{1+\frac{M_0}{H_r}}\frac{1}{\Delta H}\cdot\left[\widetilde{D}(H)\sqrt{1+\frac{M_0}{H_r}}\left(\frac{d\tau_\perp}{dI}\right)-\widetilde{L}(H)\left(\frac{d\tau_\parallel}{dI}\right)\right] \\ &= D\cdot\widetilde{D}+L\cdot\widetilde{L}. \end{aligned} \tag{2.19}$$

Here, the amplitudes of dispersive and Lorentz components D and L are:

$$D = \frac{I_{RF}^2}{4M_s}(R_P - R_{AP})\sin\theta\left[1+\frac{M_0}{H_r}\right]\frac{1}{\Delta H}\frac{d\tau_\perp}{dI} \tag{2.20}$$

and

$$L = -\frac{I_{RF}^2}{4M_s}(R_P - R_{AP})\sin\theta\sqrt{1+\frac{M_0}{H_r}}\frac{1}{\Delta H}\frac{d\tau_\parallel}{dI}. \tag{2.21}$$

From Eq. 2.19, it can be seen that V_r is a linear combination of Lorentz and dispersive line shapes.

The ratio of the dispersive and Lorentz magnitudes D/L, is calculated as

$$D/L = \sqrt{1+\frac{M_0}{H_r}}\left.\frac{d\tau_\perp/dI}{d\tau_\parallel/dI}\right|_{I_0=V/R}, \tag{2.22}$$

where V is the voltage bias and R is the resistance of the MTJ. The terms $d\tau_\perp/dI$ and $d\tau_\parallel/dI$ in Eq. 2.22 are 'torkances' of out-of-plane and in-plane STTs, respectively. From Eq. 2.22, D/L is proportional to the ratio of the out-plane and in-plane torkances. Since both torkances are proportional to $\sin\theta$ [41], D/L is independent to θ. In chapter 6, it will be shown that D/L at TSTT case is dependent to θ. The different angular dependences of D/L at dc-biased STT and TSTT cases makes it possible to distinguish these two kinds of torques.

Chapter 3

Samples and experimental setup

In this thesis, a measurement system was built in order to study the static and dynamic properties of MTJs. The system has the capabilities to

(1) adjust magnetization configurations in MTJs;

(2) excite ferromagnetic resonance (FMR) in MTJs by microwave currents;

(3) detect FMR spectra electrically;

(4) apply dc voltage biases on MTJs using a voltage source;

(5) establish a temperature gradient across tunnel barriers using a laser beam;

(6) change the global temperature of MTJs using a Peltier device.

In this chapter, the general concept of the entire system is explained first. Then, the different functions of this measurement system are discussed in detail. Also, the composition and structure of the MTJs used in this thesis are provided .

3.1 Composition and structure of magnetic tunnel junctions

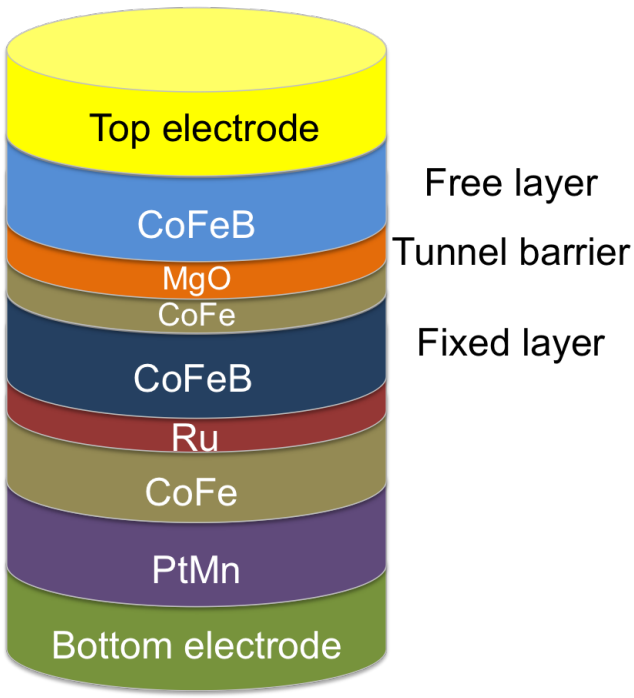

Figure 3.1: A sketch of the MTJ structures used in this thesis fabricated by Everspin.

The MTJs used in this thesis were fabricated on two wafers grown under different conditions in two different groups. One of the wafers is from Everspin which was grown on a Si substrate covered with 200 nm of SiO_2. The MTJ multilayers (Fig. 3.1) contain PtMn(20)/CoFe(2.27)/Ru(0.8)/CoFeB(2.2)/CoFe(0.525)/MgO(1.2)/CoFeB(2.5) from bottom to top (the unit of these thickness values is in nm). The bottom CoFeB layer pinned by the PtMn layer acts as a fixed layer, and the top CoFeB layer acts as a free layer. These MTJ layers have elliptical shapes with various long and short axes. The long axes of the MTJs are parallel to the pinning direction. The long axes

of the different MTJs used vary from 126 to 420 nm, and the short axes vary from 63 to 120 nm. With different combinations of long and short axes, the samples have cross-sectional areas ranging from 7938 to 50400 nm^2, and they are all small enough to ensure the single domain switching as shown in Fig. 2.2.

The other wafer is from INESC [114] and was grown on a Corning glass substrate. The MTJ structures includes PtMn(18)/CoFe(2.2)/Ru(0.9)/CoFeB(3)/MgO(0.7)/CoFeB(3) (the unit of these thickness values is in nm). The MTJ layers have rectangular shapes with areas ranging from 4 to 24 μm^2.

3.2 Experimental system

In this thesis, the static and dynamic current and thermal transport in MTJs were systematically studied . To do this, a comprehensive experimental system was developed. As shown in Fig. 3.2, this experimental system can achieve electrical detection under different situations with various independent variables. These variables include magnetization configurations, which are denoted by the relative angle between the two magnetizations (θ) and controlled by an external magnetic field; ac spin-transfer torque, which is applied by a microwave current; dc spin-transfer torque, which is applied by a dc-bias; thermal spin-transfer torque, which is applied by laser heating; and adjustment of ambient temperature, which is achieved by using a Peltier device.

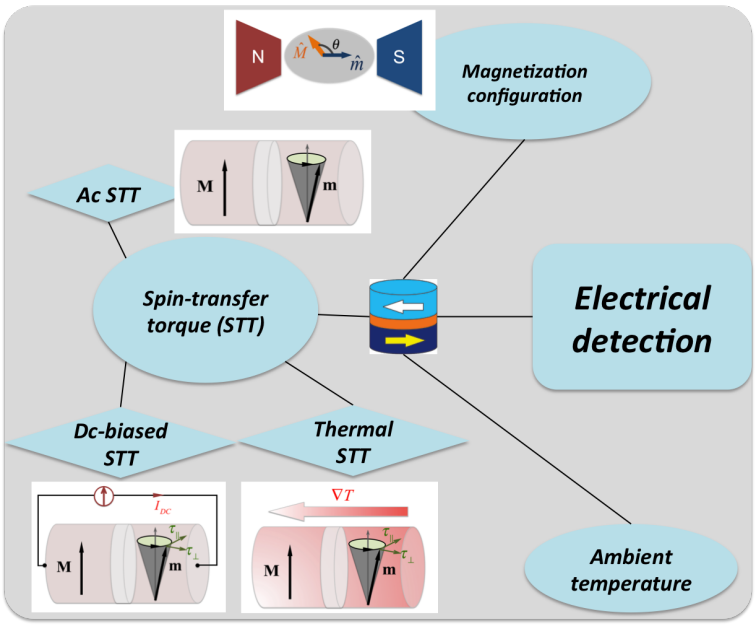

Figure 3.2: The comprehensive experimental system built for this thesis study. This system contains three controlling functions and a measurement part. The first controlling function is the control of magnetization configurations by an external magnetic field. The magnetization of the free layer can be excited by a microwave current to precess along its equilibrium position. When the frequency of the microwave current equals to the resonance frequency, FMR will occur. At the FMR condition, by applying a dc bias or a temperature gradient, a dc-biased STT or a TSTT is applied on the precessing magnetization, which affects the FMR spectra. To exclude the effects caused by the overall temperature increase, the overall temperature of the sample can be adjusted by the external heating devices attached to it. The measurements are mainly measured based on the electrical detection method.

The electrical detection of FMR in this thesis was mainly achieved by using the lock-in technique. A lock-in amplifier is widely used to detect a small ac signal in a noisy environment. Essentially, a lock-in amplifier is 'locked' by a reference signal. This reference signal multiplied with the input signal and integrates to a dc signal over a specified time, which is much longer than the period of the reference signal. The noise signals, at frequencies other the reference frequency, are rejected and do

not affect the measurement.

In this thesis, the comprehensive systems are divided into small parts to perform various functions.

Static transport measurement

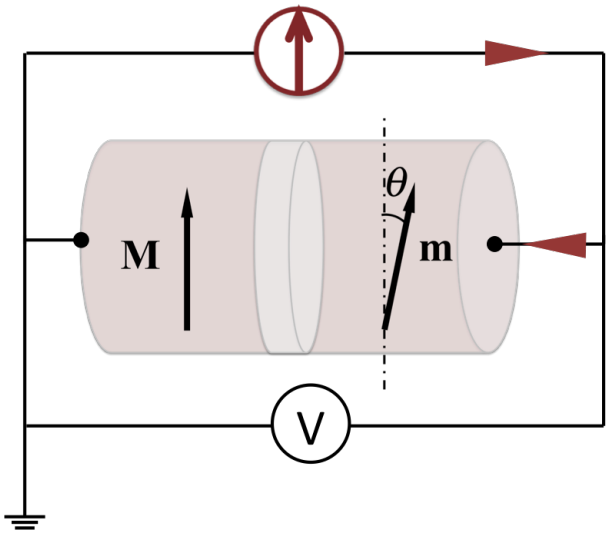

Figure 3.3: Sketch of the circuit used for current dependence measurement. The angle between the two magnetizations (θ) is set by an external magnetic field. A dc current is sent into the sample and the dc voltage across the sample is measured.

Tunneling magnetoresistance (TMR) is a key feature of an MTJ. The resistance of an MTJ is calculated by the measured voltage across the MTJ using a voltmeter with a very small current (1 μA for example) which does not change the resistance of the MTJ. By increasing the dc current, the current dependent magnetoresistance and TMR are obtained. Figure 3.3 shows the circuit of current dependence measurement. Here, a Keithley 2400 source meter was employed to generate a dc current and measure the dc voltage across the MTJs at the same time. The static transport properties of the MTJs are studied in chapter 4.

Electrical detection of spin dynamics in non-resonance regime

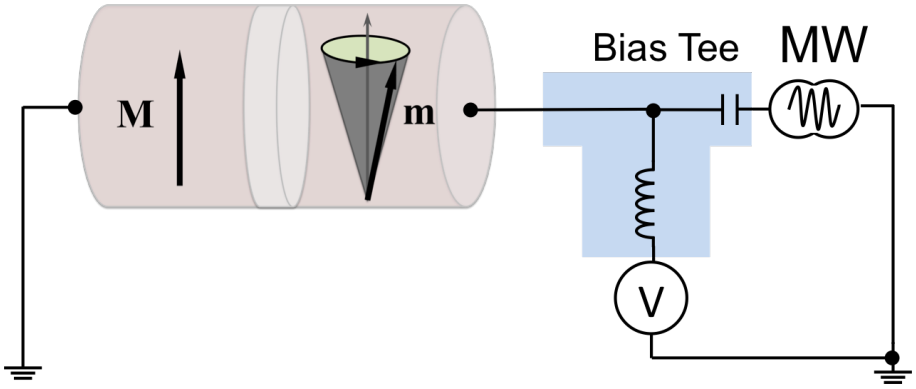

Figure 3.4: Sketch of the circuit for microwave rectification. The magnetization configurations of the MTJs are adjusted by an external magnetic field. A microwave current is sent into the sample by a coaxial cable or a horn antenna. The voltage across the sample generated by the Seebeck rectification is measured. A bias tee is employed to separate the dc and microwave current.

Figure 3.4 shows the circuit for microwave rectification measurement on MTJs. A microwave current is sent into an MTJ and a voltage is detected across the sample. It is shown in chapter 5 that in a non-resonance regime (when the frequency of the microwave is away from the ferromagnetic resonance frequency), the voltage is caused by the Seebeck rectification.

The microwave current is generated by an Agilent E8267D microwave generator, which enables us to generate microwave currents from 100 kHz to 20 GHz. There are two ways to send a microwave into the MTJs. One could either use a coaxial cable connected to one of the electrodes, or could radiate microwaves on the samples using a horn antenna by placing it in front of the sample with a distance of around 5 cm. A bias tee is used to separate the microwave current and the dc signal as shown in Fig. 3.4.

Electrical detection of spin dynamics in resonance regime

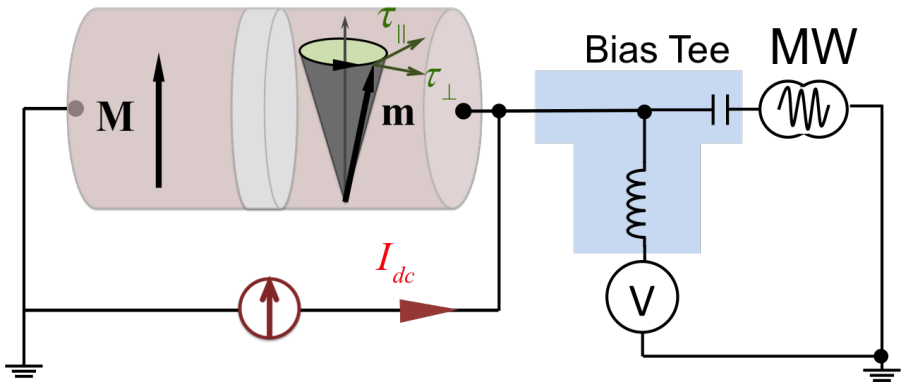

Figure 3.5: Sketch of the circuit used for studying dc-biased STT. A microwave current is sent into the sample by a coaxial cable to excite the FMR. The FMR voltage across the sample is measured by the lock-in technique. A dc bias current is sent into the sample and the FMR spectra for various dc bias currents are measured. A bias tee is employed to separate the dc and microwave current.

By adjusting the microwave around the resonance regime, the FMR of MTJs can be measured. To study the effect of dc-biased STT on MTJs, an extra dc current is sent into the sample to apply a dc STT as shown in Fig. 3.5. The frequency of the microwave current is close to the FMR frequency.

To study the effect of TSTT on MTJs, a laser beam is employed to heat the top side of the MTJs as shown in Fig. 3.6. This laser heating technique can establish a temperature gradient across the MTJ effectively [52]. The wavelength of the solid laser generator used in this thesis was 671 nm. The power of the laser can be tuned from 0 up to 300 mW.

The study of STT generated either by a dc-bias or a temperature difference is performed in chapter 6.

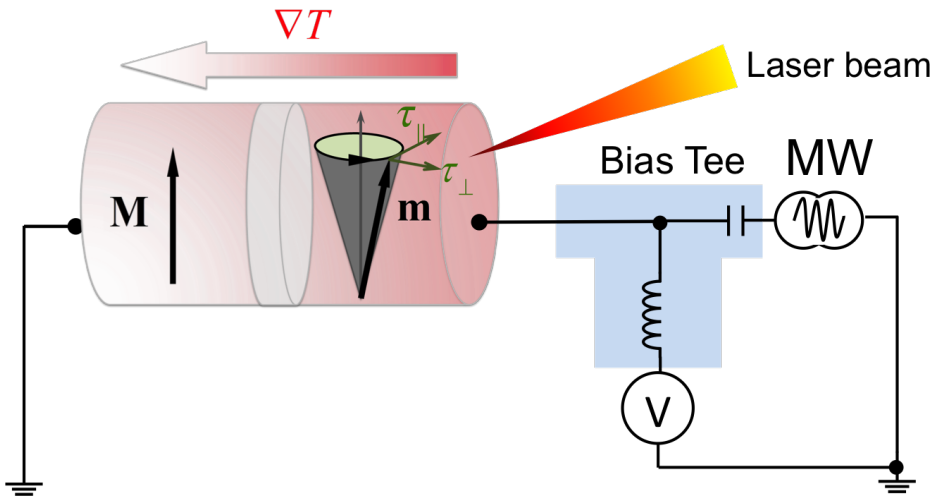

Figure 3.6: Sketch of the circuit used for studying TSTT. A microwave current is sent into the sample by a coaxial cable to excite the FMR. The FMR voltage across the sample is measured by the lock-in technique. A temperature difference is generated by heating one side of the MTJs with a laser beam. FMR spectra for various temperature differences are measured. A bias tee is employed to separate the dc and microwave current.

Global heating by a Peltier device

To heat the MTJ globally, a thermoelectric cooling/heating device is introduced. This thermoelectric cooling/heating device is composed of two ceramic plates connected by two different types of materials. It uses the Peltier effect to transfer heat from one side of the device to the other as a charge current, I, flows through the device. As a consequence, the temperature on one of the plates will increase, while the temperature will decrease on the other plate. The MTJ sample is attached on one of the plates of the thermoelectric cooling/heating device as shown in Fig. 3.7. The other plate of the device is connected to a copper heat-sink whose temperature remains constant while the temperature of the plate attached to an MTJ reaches equilibrium.

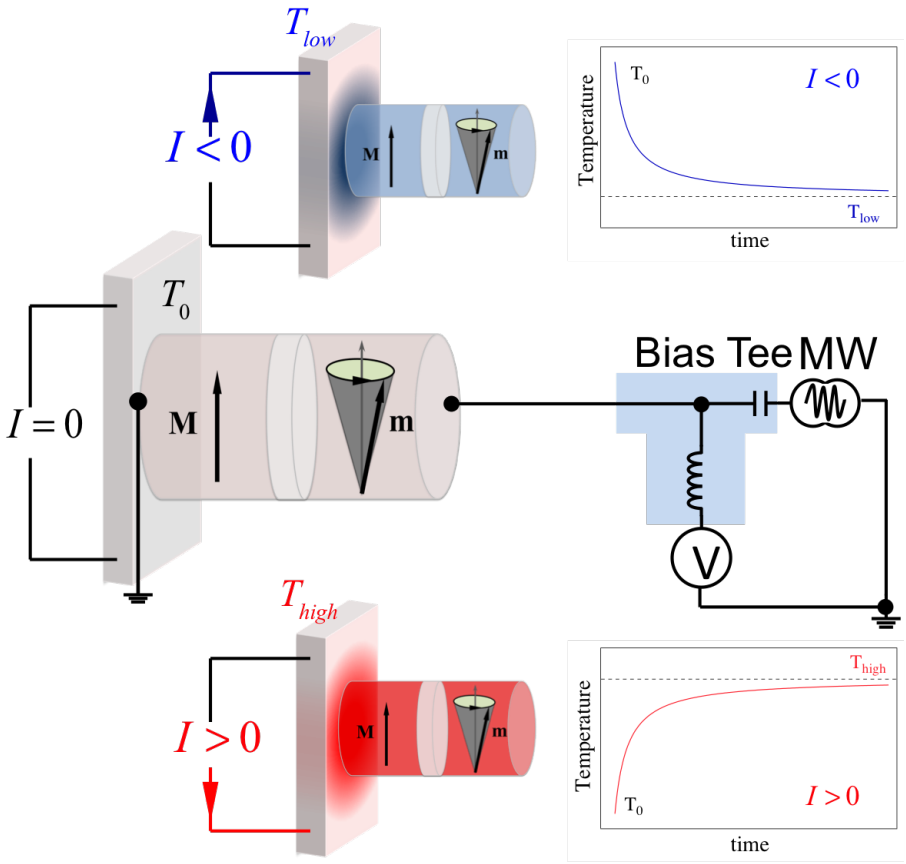

Figure 3.7: Sketch of the circuits used to control the overall temperature by heating the samples with an attached Peltier device. When a current I is sent into the Peltier device, heat will transfer from the surface attached to the sample to the other surface, and the direction of the transfer of heat is determined by the polarity of I. When $I < 0$, the temperature decreases, but when $I > 0$, the temperature increases. The rate of the temperature changes are fast at the beginning, and become slower until reaching thermal equilibrium.

The direction of the transport of heat is determined by the polarity of I. For example, as shown in Fig. 3.7, when $I < 0$, the temperature of the surface attached to the sample decreases, and it reaches an equilibrium temperature of T_{low}. In contrast, when $I > 0$, the temperature of the surface attached to the sample increases, and it reaches an equilibrium temperature of T_{high}. The values of T_{low} and T_{high} are

determined by the amplitude of I. A larger I results in a higher T_{high} and a lower T_{low}. The temperature dependence of spin dynamics in the resonance regime is studied in chapter 6.

Chapter 4

Static transport properties in magnetic tunnel junctions

It was found that the tunneling magnetoresistance (TMR) ratio decreases by increasing an applied current in magnetic tunnel junctions (MTJs), and this decrease is dependent on the polarities of this current [85, 99, 103, 115–118]. This current dependent TMR is asymmetric with respect to the current polarity, and the magnetoresistance decrease in an anti-parallel (AP) state is more significant than in a parallel (P) state. Since the TMR ratio is one of the most basic parameters which reflects static transport properties in MTJs, the study of the current dependent TMR can help us to understand the spin-dependent tunneling in MTJs intensively.

Different mechanisms have been developed to describe the current dependent of TMR in MTJs [33–38, 70, 85, 99, 104, 116, 119]. It has been found that the magnetoresistance is dependent on the height of the tunnel barrier, which is dependent on the biased voltage and the orientation of the tunneling spin [85, 117, 119]. The

decrease in TMR, occurring at bias voltages on the order of hundreds of millivolts, is caused by the collective excitation of local spins by electrons at the interface between the ferromagnetic (FM) layer and the tunnel barrier [70]. It has also been shown that the magnetoresistance is very sensitive to extrinsic conditions, including annealing, dislocations, doping elements to the barrier at interfaces, and sputtering during fabrication [116]. Recently, it has been found that the magnetoresistance can also be decreased by spin-transfer torque (STT), where STT causes a rotation in the magnetization of the FM layer, which lowers the TMR ratio [33–38, 104].

Since current dependent magnetoresistance is complicated and strongly dependent on the properties of the interfaces between the FM layer and the tunnel barrier, this dependence can vary from sample to sample. In this chapter, the results of systematic studied of the current dependent magnetoresistance in the MTJs are presented. The measurements were taken on samples with various cross-sectional areas, at various temperatures, and in different magnetization configurations. This current dependence was attributed to the change of the spin-polarization by a spin-polarized current and a phenomenological model was built. With this model, the current dependent TMR in MTJs is well explained. This model also allows us to evaluate the threshold current for magnetization switching in MTJs, which is another important parameter for applications. The study in this chapter will help us understand thermoelectric transport and thermal spin-transfer torque in the following chapters. This work has been published on *AIP Advances* [65].

4.1 The relationship between tunnel magnetoresistance and spin polarization

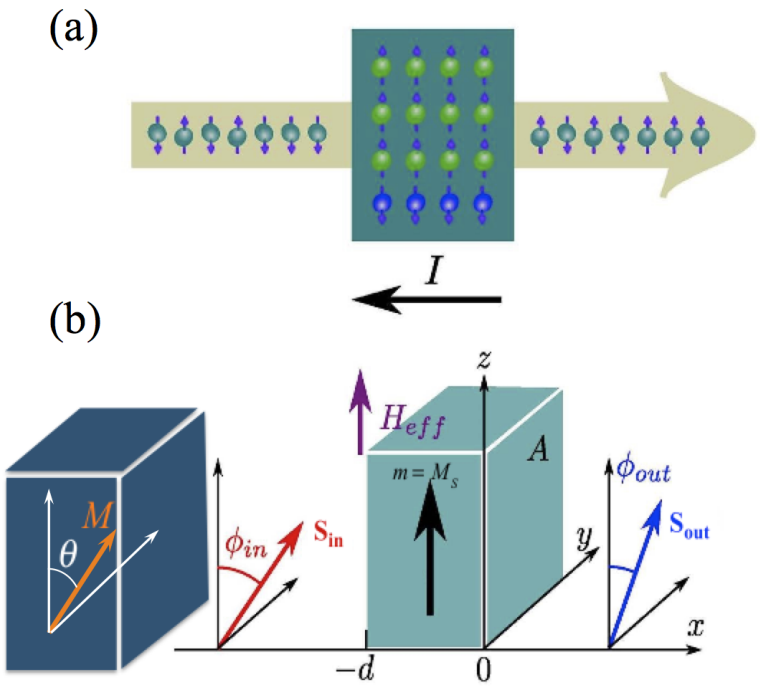

Figure 4.1: (a) A sketch of the spins localized in an FM layer reversed partially by the spins carried by a spin-polarized current flow. (b) Coordinates of the spin-polarized current flowing through an FM layer.

To describe the current dependent TMR, a phenomenological model was built based on the conservation laws of angular momentum and of electrons. In this model, TMR is presented as a function of the current applied to the sample.

As shown in Fig. 4.1(a), when a spin-polarized current passes through an FM layer, an STT will be applied onto the magnetization of the FM layer. This STT is due to the exchange interaction between the spins carried by the current and localized

in the free FM layer. The net number of spins, which is the difference between the majority and minority spins in the FM layer is changed by this spin-polarized current.

The coordinate system is shown in Fig. 4.1(b). The magnitudes of the magnetizations of the free and fixed FM layers are m and M, respectively. The free FM layer has a cross-sectional area of A and a thickness of d, and its magnetization is aligned to the direction of the effective field H_{eff} (z axis) which equals to the saturation magnetization M_s. The number of net spins (N_{free}) in the free layer at a certain temperature is

$$N_{free} = M_s A d/\mu_B, \tag{4.1}$$

where μ_B is the Bohr magneton.

A charge current with an amplitude I is spin-polarized after it has passed through the fixed FM layer and the direction of its polarization is along $\mathbf{s_{in}}$ at an angle ϕ_{in} with respect to the z axis. It is assumed that ϕ_{in} equals to the angle between two magnetizations of the two FM layers (θ). When this spin-polarized current passes the free FM layer, the polarization will be changed to the direction $\mathbf{s_{out}}$ at an angle ϕ_{out} with respect to the z axis. Within the local momentum relation time τ_r, $I\tau_r$ is the electric charge flowing through the free layer. The change of the number of majority spins ΔN_r in the FM layer can be calculated as

$$\Delta N_r(I) = -\frac{I\tau_r}{2e}\left[P_{in}(\cos\phi_{in} - 1) - P_{out}(\cos\phi_{out} - 1)\right]. \tag{4.2}$$

Here, e is the elementary charge, and P_{in} and P_{out} are the polarization of the current before and after going through the FM layer, respectively. Thus, the number of net spins in the free FM layer, N_{free}, is a function of the current I, and can be written

as $N_{free}(I) = N_{free}(0) - N_r(I)$. The spin polarization of the free FM layer, P_{free}, defined as the ratio of the net spin to the number of electrons in the conduction band of the free FM layer, N_{free}^{total}, is a function of the current and can be written as $P_{free}(I) = N_{free}(I)/N_{free}^{total}$.

It is assumed that the electrons flowing out the free layer have the same polarization and spin orientation as those in the free FM layer [120, 121]. Thus, $\phi_{out} = 0$ and $P_{out} = P_{free}(I)$. Then the polarization of the free layer can be written as,

$$P_{free}(I) \;\; = \;\; P_{free}(0)(1 - I/I_c). \tag{4.3}$$

Here, the substitutions $\tau_r = 1/\alpha\gamma H_{eff}$ and $\gamma = 2\mu_B/\hbar$ were used, where α is the dimensionless Gilbert damping coefficient and γ is the absolute gyromagnetic ratio. I_c is the threshold current where $R_{AP} = R_P$, i.e. at I_c, switching has already been happened. It is defined as

$$I_c \equiv \frac{2e}{\hbar}\frac{2}{1-\cos\phi_{in}}\frac{\alpha}{P_{in}}M_s A d H_{eff}, \tag{4.4}$$

by assuming $N_{free}^{total} \gg I\tau_r/e$. Since switching between two magnetization states is one of the fundamental function of MTJs in their application, I_c is a highly interesting quantity.

Equation 4.4 provides a way to estimate I_c quantitatively. From this equation, I_c is proportional to the Gilbert damping coefficient, total spin momentums in the free layer, and the effective field; and inversely proportional to spin-polarization of the current. In addition, I_c strongly depends on the relative angle between the two magnetizations (ϕ_{in}). From Eq. 4.4, it is expected that the threshold current is larger at a P state than at an AP state. Such a threshold current was also derived by Sun

[36] by considering spin-transfer torque. But in their work, I_c is proportional to $\cos^{-1}\phi$ which is different from Eq. 4.4. In section 4.4, It will be shown that Eq. 4.4 can explain the present results well.

Combining Eq. 4.3 and Jullière's two current model, the TMR ratio η and resistance $R(I, \phi_{in})$ can be represented as

$$\eta = \frac{2P_{fix}P_{free}(1 - I/I_c)}{1 - P_{fix}P_{free}(1 - I/I_c)}, \tag{4.5a}$$

$$R(I, \phi_{in}) = R_P \frac{1 + P_{fix}P_{free}(1 - I/I_c)}{1 - P_{fix}P_{free}(1 - I/I_c)}, \tag{4.5b}$$

where P_{fix} is the spin polarization of the fixed FM layer defined as the ratio between the number of net spins and the total number of conduction electrons in the fixed FM layer. In Eqs. (4.5a) and (4.5b), the spin polarization of both FM layers P_{fix} and P_{free} refers to the original spin polarizations with no applied current and are determined by the intrinsic properties of the material. In this case, both FM layers are CoFeB with the same thickness, and thus it is assumed that $P_{fix} = P_{free}$. Equation (4.5a) shows the relation between TMR and I, which can be used empirically to describe the behavior of current dependence of TMR.

4.2 Current dependence of TMR at room temperature

To study the current dependent TMR, the resistance of an MTJ was measured in the AP state and P state, by sending a current through the MTJ up to 100 μA and measuring the voltage on it. The AP and P states were set by an external magnetic field and the MTJ had a cross-sectional area of 0.04 μm^2.

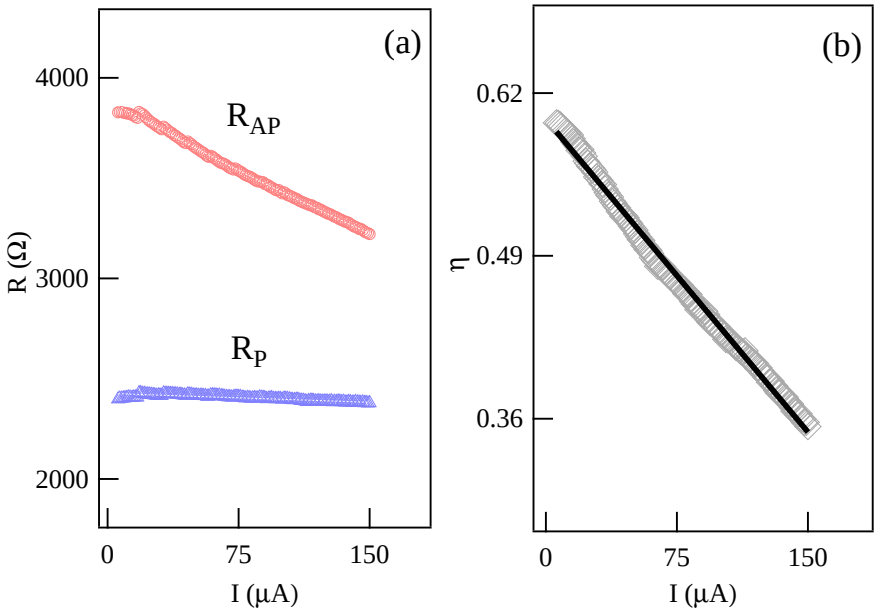

Figure 4.2: (a) The resistances of the AP and P states in an MTJ decrease as a function of the current. (b) The TMR ratio η decreases as a function of the current. The solid line is fit curve using Eq. (4.5a), where $P_{fix} = P_{free} = 0.48$.

The resistances of both the AP and P states as a function of the dc current are shown in Fig. 4.2(a). It can be seen that the resistance of the AP states drops rapidly while the resistance of the P state only decreases slightly by increasing the current amplitude. The TMR ratio, η, was evaluated as a function of the current as shown in Fig. 4.2(b). It is clear that η decreases from 0.6 to 0.36 by increasing the current, which was well fitted by using Eq. (4.5a). In this fit, the spin-polarization of both layers were $P_{fix} = P_{free} = 0.482$, which is consistent with the reported spin polarization of CoFeB [122]. In addition, the threshold current $I_c = 423$ μA agrees well with the typical threshold current measured in MgO-based MTJs [43, 44].

4.3 Tunnel magnetoresistance current dependence under various cross sectional areas

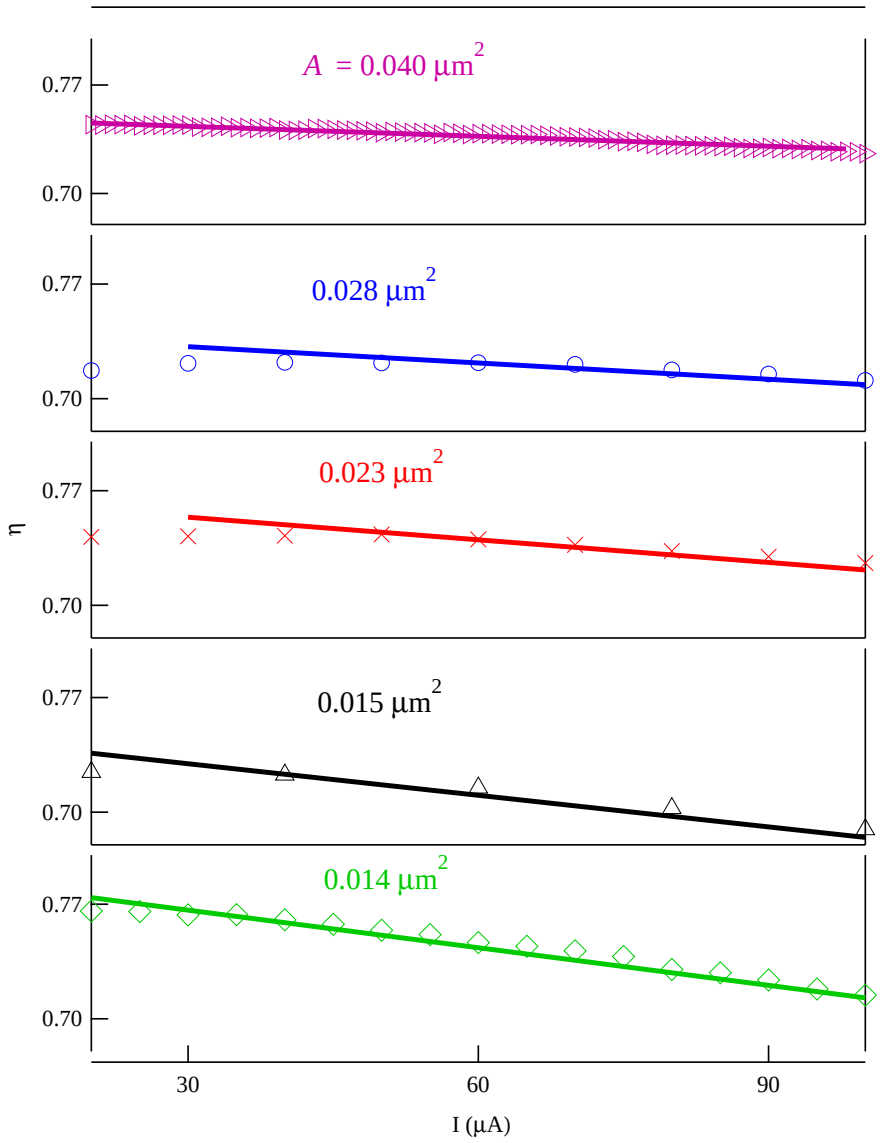

Figure 4.3: For different junction areas A, all TMR ratios decrease as current I increases, which were well fitted using Eq.(4.5a), where $P_{fix} = P_{free} = 0.48$ and I_c varies for different A. I_c as a function of A is plotted in Fig. 4.4.

As indicated by Eq. 4.4, the threshold current, I_c, is proportional to the barrier

cross-sectional area. To confirm this, the current dependent TMR was studied on MTJs with various cross-sectional areas, and the threshold current was evaluated. Here, measurements were taken on MTJs with different cross sectional areas, A, as 0.040, 0.028, 0.023, 0.015 and 0.014 μm^2.

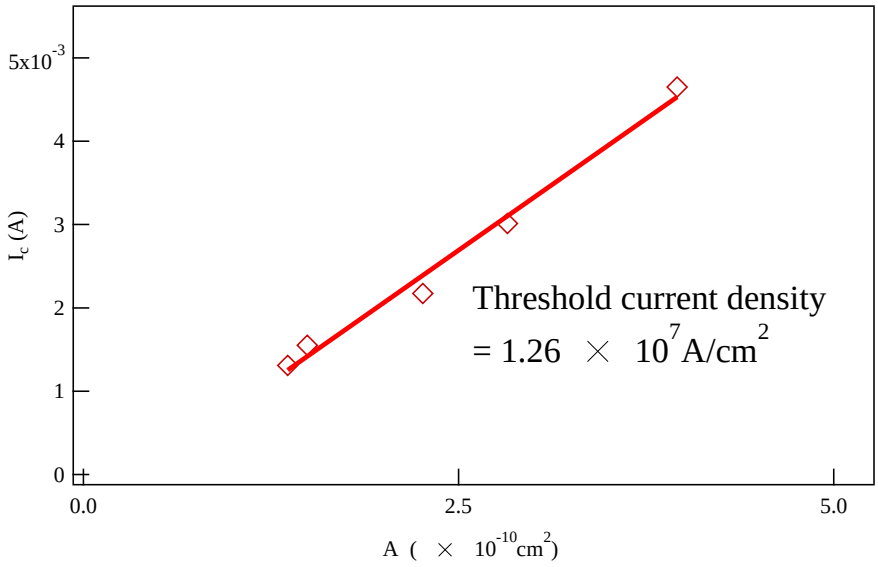

Figure 4.4: The threshold current I_c is proportional to A as shown by the solid line. The slope of this line indicates the threshold current density of 1.26×10^7A/cm^2 for switching.

As shown in Fig. 4.3, the measured TMR ratio η as a function of the current for different A were plotted and fitted by using Eq. (4.5a). In these fits, the spin polarization for all samples is 0.48. The threshold currents for different MTJs are shown in Fig. 4.4. The linear dependence of I_c on A is as expected from Eq. 4.4, indicating that the threshold current density, calculated as I_c/A, is constant. In this case, it is 1.26×10^7A/cm^2, which is on the same order for the magnetization switching in most MTJs [43, 44].

4.4 Resistance current dependence under various magnetization configurations

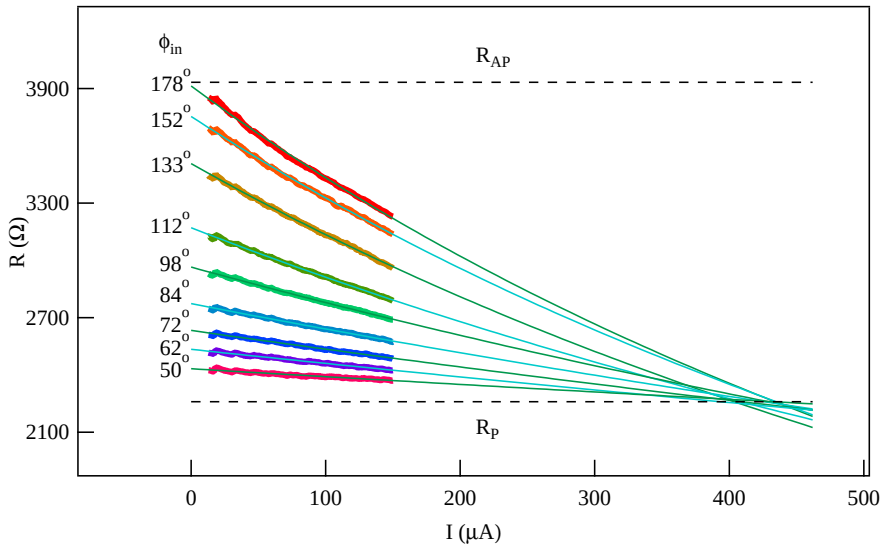

Figure 4.5: For different ϕ_{in}, the resistance decreases as a function of current, and is well fitted by using Eq. (4.5b). All lines intersect around 2217 Ω at the current of $430 \pm 20\ \mu A$.

The threshold current also depends on the relative angle ϕ_{in} between the magnetizations of the two FM layers. In preparation for the study of the angular dependence of spin-transfer torque in chapter 6, the dc transport property, i.e. the current dependence of resistance at various values of ϕ_{in} was studied. In the measurements, ϕ_{in} was set by adjusting the external magnetic field. The values of ϕ_{in} were estimated via Eq. 2.3 by measuring the resistance of MTJs with a current of 0.1 μA, which is much smaller than I_c.

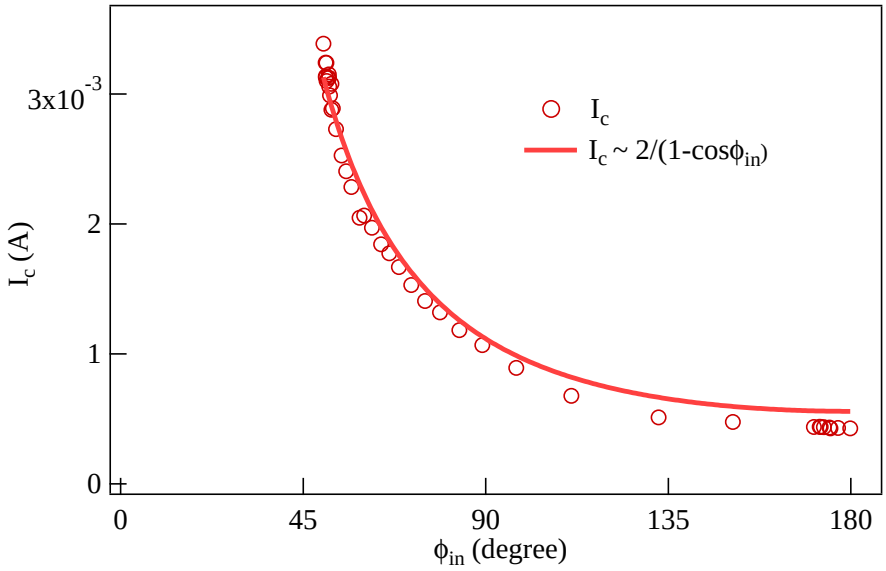

Figure 4.6: Angle ϕ_{in} dependence of I_c, which agrees well with Eq. (4.4) shown in the solid line.

As shown in Fig. 4.5, all the resistances at various angle ϕ_{in} decreases by increasing the current and they were fitted by using by using Eq. (4.5b). At a larger ϕ_{in}, the rate of decrease is larger than at a smaller ϕ_{in}, because the current induces more net spin changes in the free layer for a larger ϕ_{in} than for a smaller ϕ_{in}. The evaluated threshold current for each angle ϕ_{in} were plotted in Fig. 4.6. The calculated ϕ_{in}-dependent threshold current used Eq. 4.4 were plotted as the solid curves in Fig. 4.6 for comparison. In the calculation, Gilbert damping coefficient $\alpha = 0.01$ [41] and spin polarization $P_{in} = 0.48$ [122] were used. The current model works well here and indicates that the lowest threshold current occurs when the spin-polarization of the spin current is opposite to the magnetization of the FM layer.

4.5 Tunnel magnetoresistance current dependence under various temperatures

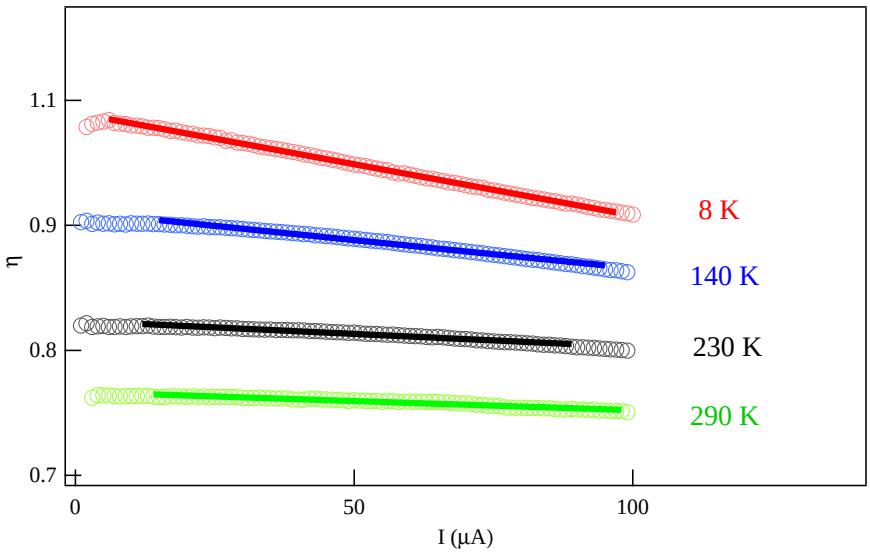

Figure 4.7: η as a function of I at 8, 140, 230 and 290 K.

As a preparation for the studies of thermal related effects, such as the Seebeck effect in chapter 5, and the thermal spin-transfer torque in chapter 6, the current dependence measurements of TMR were performed at various temperatures. The sample was put into a non-magnetic cavity and cooled down to 8 K using a helium compressor unit. Figure 4.7 shows η as a function of I at 8, 140, 230 and 290 K. Decreases of TMR ratios with increasing current was observed at various temperatures. The solid lines are fits using Eq. (4.5a), where $P_{fix} = P_{free} = 0.48$ [122].

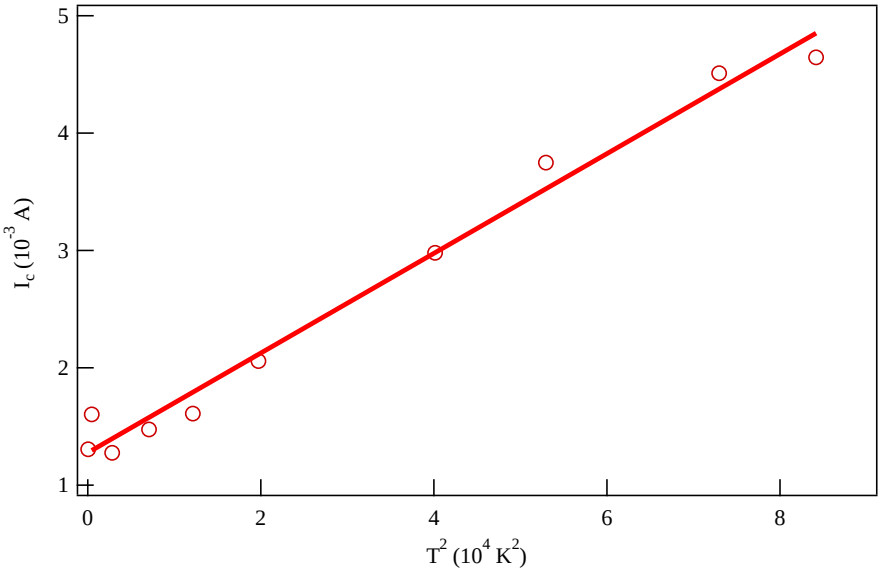

Figure 4.8: I_c as a function of T^2.

The threshold current I_c can be expressed by the relation $I_c(T) = I_c(0)(1 + CT^2)$ [123], where $I_c(0)$ is the threshold current at 0 K and C is a constant determined by the barrier height and thickness. To confirm this relationship in the tunneling junction used in this thesis, I_c was plotted as a function of T^2 as shown in Fig. 4.8. It is seen that I_c is proportional to T^2, which is evidence of the tunneling phenomenon in the MTJs [123].

Essentially, the T^2 response is a natural result of a tunneling barrier starting from Landauer's approach, where the two ferromagnetic layers are treated as two terminals connecting with a channel. The current transport from one terminal to the other is determined by the voltage and temperature differences applied to the two terminals. The expansion of this current represented to temperature will give out a zero, second and even higher orders to temperature. However, the zero and second orders are

dominant terms, which results in a T^2 dependence [124].

4.6 Summary

In this chapter, the behavior of the current dependent TMR in MTJs was studied. Experimentally, a decrease of the TMR ratio while increasing the applied current was observed on samples with various cross-sectional areas at various temperatures. The reason for this decrease is due to the change of spin polarization in the FM layer of MTJs, which is based on the exchange interaction between the spin current and spins localized in the free FM layer. A phenomenological model was provided to describe the decreases of magnetoresistance and TMR ratio. The experimental observation of the resistance change due to an applied current is well explained, and the value of the threshold current for magnetization switching in MTJs is also estimated at different magnetization configurations as well as at different temperatures ranging from 8 to 300 K. This study of the static transport in MTJs will help in understanding and studying the dynamic transport in the following chapters.

Chapter 5

Seebeck Rectification in magnetic tunnel junctions

Recently, the new discipline of spin *caloritronics* [45] has received much attention, since it introduced *spin* as another degree of freedom into traditional thermoelectricity, and started a renaissance of thermoelectricity in spintronic devices and magnetic structures [52, 54, 125–127]. Among various thin films and nanostructures, in which spin caloritronics has been experimentally investigated, magnetic tunnel junctions (MTJs) were one of the most attractive systems with important discoveries such as the spin-dependent Seebeck effect [46–52] and thermal spin-transfer torque [60, 74, 107]. Recently, a number of experiments have found that in MTJs, the magnitude of the Seebeck coefficient (S) can be as high as 1000 μV/K [50, 52], 3-orders of magnitude larger than in normal metallic materials. Furthermore, similar to the resistance, S of an MTJ at a parallel (S_P) and an antiparallel (S_{AP}) configurations has different values [50, 52, 128]. For this reason, it is an analogue to tunnel magnetoresistance

(TMR) effect, and is named the magneto-Seebeck effect. The magneto-Seebeck ratio, S_{MS}, defined as $S_{MS} = \frac{S_P - S_{AP}}{min(S_P, S_{AP})}$, is as high as 100 % in MTJs [52], which makes this effect a highly attractive candidate for spin caloritronic application.

In previous studies of the spin-dependent Seebeck effect in MTJs, the measurements were performed under static conditions [50, 52, 128]. The MTJs were heated externally by using a laser beam [50, 52] or by using an attached electric heater line [128], Specifically, a voltage was generated by a temperature difference at either an anti-parallel (AP) or a parallel (P) configurations. Here, the magnetization configurations were set by an external magnetic field, and at each measurement, the magnetization of the free layer was at its equilibrium position.

By contrast, the work in this chapter was based on an intrinsic Joule heating and was performed in a dynamic condition under microwave radiation. This intrinsic heating is: when a microwave current is sent into an MTJ, each layer of the MTJ is heated by this current; because of the larger electrical resistance and smaller thermal conductance of the MgO barrier compared to the other metal layers, as well as the asymmetrical in geometry in an MTJ, an effective temperature difference across the barrier can be established, resulting in a dc voltage across the MTJ.

This work not only motivates the theoretical investigation of thermal spin and thermoelectric properties of MTJs driven by microwave fields [129], but also paves the way for utilizing spin caloritronics in microwave imaging [75] and energy harvesting [76]. This work has been published in *Physical Review Letters* [73].

5.1 The coupling of charge and heat current in MTJs

To study the behavior of thermoelectricity in an MTJ, a Thomson Thermoelectric Conductor (TTC) is introduced to build a model of spin-dependent electric and thermal transport in it. TTC is a conductor where a voltage and a temperature gradient exist at the same time. Consider a TTC with both particle ($\mathbf{J}$) and heat ($\mathbf{J}_Q$) flux densities as shown in Fig. 5.1, where $\mathbf{J}$ and $\mathbf{J}_Q$ satisfy the Onsager reciprocal relations and can be obtained from the 3×3 matrix (Eq. 2.7)

$$\begin{aligned} \mathbf{J} &= -(\sigma/e^2)\nabla\bar{\mu} + (S\sigma/|e|)\nabla T, \\ \mathbf{J}_Q &= (TS\sigma/|e|)\nabla\bar{\mu} - (\kappa + TS^2\sigma)\nabla T. \end{aligned} \tag{5.1}$$

Here, σ and κ are the electric and thermal conductivity, respectively; and $\bar{\mu} = \mu - |e|V$ is the electrochemical potential, where μ is the chemical potential and e is the elementary charge.

The total energy flux density in the TTC is $\mathbf{J}_W = \mathbf{J}_Q + \bar{\mu}\mathbf{J}$ and satisfies the energy conservation principle [88]

$$C_v \partial T/\partial t + \nabla \cdot \mathbf{J}_W = 0, \tag{5.2}$$

where C_v is the specific heat per unit volume.

Because the lateral dimension (about 100 to 1000 nm) is much larger than the dimension of along the direction of current flow (on the order of tens of nm) in the MTJ stacks (x direction in the case here), a one-dimensional TTC with a length d was used to simplify the actual three-dimensional problem, so that Eq. 5.2 reduces

to

$$C_v \frac{\partial T}{\partial t} + \frac{\partial J_{Wx}}{\partial x} = 0, \tag{5.3}$$

where J_{Wx} is the total energy flux density in the direction of current flow (x direction).

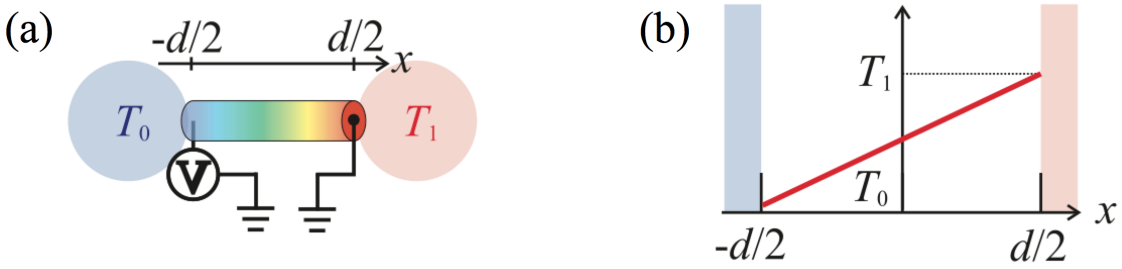

Figure 5.1: (a) The Thomson thermoelectric conductor (TTC) connected in an open circuit. (b) The corresponding temperature profiles of the TTC in (a).

Figure 5.1(a) shows the case in an open electric circuit by connecting the TTC to two thermal reservoirs with different temperatures T_0 and T_1, the steady state solution (where $\frac{\partial T}{\partial t} = 0$) of Eq. 5.3 gives $V = S(T_1 - T_0)$ and $T(x) = (T_0 + T_1)/2 + (T_1 - T_0)x/d$, as shown by the plot in Fig. 5.1(b). This is the well-known Seebeck effect.

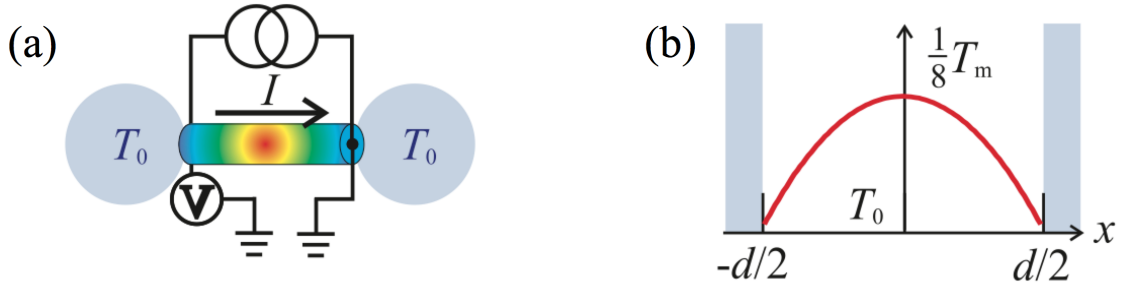

Figure 5.2: (a) The Thomson thermoelectric conductor (TTC) connected in a closed circuit. (b) The corresponding temperature profiles of the TTC in (a).

However, in a closed circuit carrying a continuous electric current with the current density $J_C = -|e|J$, if the TTC is set in a symmetrical thermal environment as shown

in Fig. 5.2(a), then the steady state solution depends on the boundary conditions at the contacts. In the case where the thermoelectric heating/cooling dominates over both Joule and conductive heating at the contacts, the result is the well-known Peltier effect. On the other hand if the thermoelectric effect is weak, the solution leads to $T(x) = T_0 - [(x/d)^2 - 1/4]T_m/2$, with $T_m \equiv (J_C^2 d^2)/(\kappa\sigma)$. The maximum temperature is located at the center of the TTC, as shown in Fig. 5.2(b).

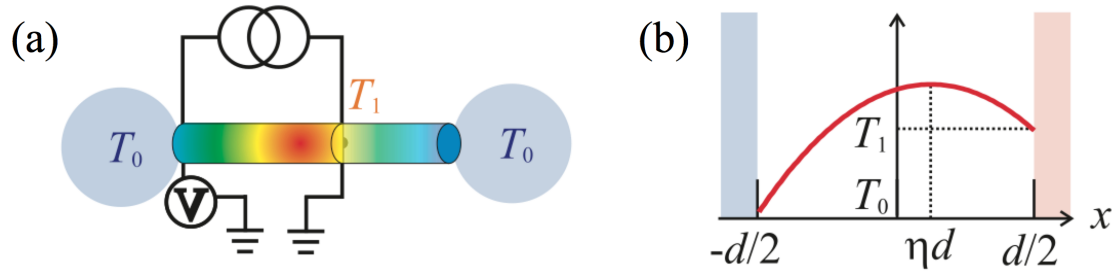

Figure 5.3: (a) The Thomson thermoelectric conductor (TTC) connected in a closed circuit with a supporting material such as Si. (b) The corresponding temperature profiles of the TTC in (a).

The position of the maximum temperature shifts by an amount of ηd if the TTC is set in an asymmetric thermal environment. For example, by connecting the TTC to the thermal reservoir at one side via a supporting material such as Si as shown in Fig. 5.3(a). The thermal asymmetric parameter η can be calculated by solving Eq. 5.3 to determine the temperature distribution $T(x)$. In the case shown in Fig. 5.3, it is easy to show that $\eta = (T_1 - T_0)/T_m$.

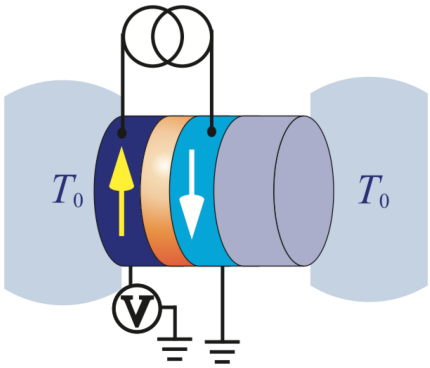

Figure 5.4: Schematic MTJ circuit used in the thesis. A microwave current is sent into an MTJ and the dc voltage across the two ends of the MTJ. The temperature of the two terminals of the MTJ is T_0.

Such a TTC is the building block of the model constructed for highlighting the intrinsic thermoelectric transport in an MTJ. As shown in Fig. 5.4, the multilayered MTJ was modeled as a series of TTCs with a cross-sectional area A. It carries the tunneling current $I = J_C A$, and is connected to the thermal reservoir directly on one side but via an insulating substrate on the other side. The MgO tunnel layer was treated as a conductor with a non-zero conductivity for calculating the Joule heating. The heat in an MTJ is generated by a current I, and eventually results in a temperature increase ΔT. The temperature distribution $T(x)$ inside the multi-layer stack can be simplified from Eq. 5.2 into a one-dimensional thermal equation given by

$$C_v \frac{\partial T}{\partial t} = \kappa \frac{\partial^2 T}{\partial x^2} + J_C^2/\sigma. \tag{5.4}$$

By solving Eq. 5.4 at the steady state condition $\partial T/\partial t$=0, it can be found that

$$V(I) = R \cdot I + S \cdot \Sigma(\eta_j R_{\kappa j} R_j) \cdot I^2, \tag{5.5}$$

where $R \equiv \sum R_j$ is the resistance of the junction; and $S \equiv \Sigma(\eta_j R_{\kappa j} R_j S_j)/\Sigma(\eta_j R_{\kappa j} R_j)$

is the Seebeck coefficient of the MTJ based on the TTC model, which is related to the resistance $R_j = d_j/(\sigma_j A)$, the heat resistance $R_{\kappa j} = d_j/(\kappa_j A)$, the thermal asymmetric parameter η_j, and the absolute thermal power S_j of the j-th layer that carries the tunneling current I.

Equation 5.5 shows that the tunneling current I in an MTJ makes not only the well-known 1st order contribution to the voltage V via Ohm's law, but also induces a 2nd order contribution. Such an $I-V$ non-linearity is intrinsically induced by the heat dissipation caused by the tunneling current, which modifies the voltage profile of the MTJ via the thermoelectric coupling. In the context of linear response, the induced nonlinear term in the $I-V$ relation is similar to the textbook example of the correction to Ohm's law via the anisotropic magnetoresistance (AMR) of magnetic materials [130], since both are determined by the coupled effect of a pair of forces which drive the linear response via the Onsager reciprocal relation. Hence, such an intrinsic coupling effect should not be ignored even in the linear transport regime.

5.2 Seebeck rectification generated by microwave heating

When there is a microwave current $I(t) = I_{RF}\cos(\omega t)$ sent into the MTJ, where I_{RF} is the amplitude and ω is the angular frequency of this current, the total voltage from Eq. 5.5 can be deduced as

$$V(t) = V_r + V_\omega \cos(\omega t) + V_{2\omega}\cos(2\omega t). \tag{5.6}$$

Here, the first term $V_r = S \cdot \Sigma(\eta_j R_{\kappa j} R_j) \cdot I^2$ is a dc voltage and is proportional to the Seebeck coefficient (η_j may be frequency dependent).

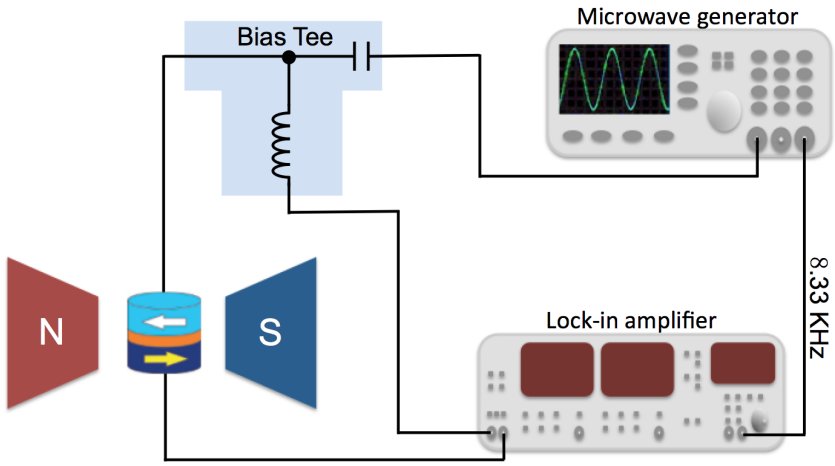

Figure 5.5: A sketch of the circuit for measurement of the Seebeck rectification. A microwave is sent into an MTJ with a coaxial cable, and the rectification voltage V_r can be detected by a lock-in amplifier with a modulation frequency of 8.33 kHz. The magnetization configuration of the MTJ is set to the P or the AP states. A bias tee is used to separate dc and ac signals.

Experimentally, as shown in Fig. 5.5, a microwave generator was used to directly send this microwave current $I(t) = I_{RF}\cos(\omega t)$ into the MTJ via a coaxial cable, and V_r was measured by using a lock-in amplifier with modulating the microwave power at 8.33 kHz with a square wave. V_r was measured in an accurate way at both the P and AP alignments of the sample as shown in Fig. 5.6(a) at $\omega/2\pi = 9.0$ GHz. Here, I_{RF} is estimated from the incident average microwave power P_{avg} via the relation $P_{avg} = (R + Z_0)^2 I_{RF}^2 / 16 Z_0$ [131], which takes into account the impedance mismatch of the MTJ with the coaxial cable ($Z_0 = 50\ \Omega$).

The data shown in this chapter were measured on two samples which were fab-

ricated on two wafers grown under different conditions in two different groups as discussed in chapter 3.1. Sample A (No. R07C6) from INESC has the dimension of 2 μm $\times$ 4 μm. Sample B (No. 652-14) from Everspin has an elliptical shape with the long and short axis of 204 and 85 nm, respectively. The long axes of sample A (B) are perpendicular (parallel) to the pinning direction.

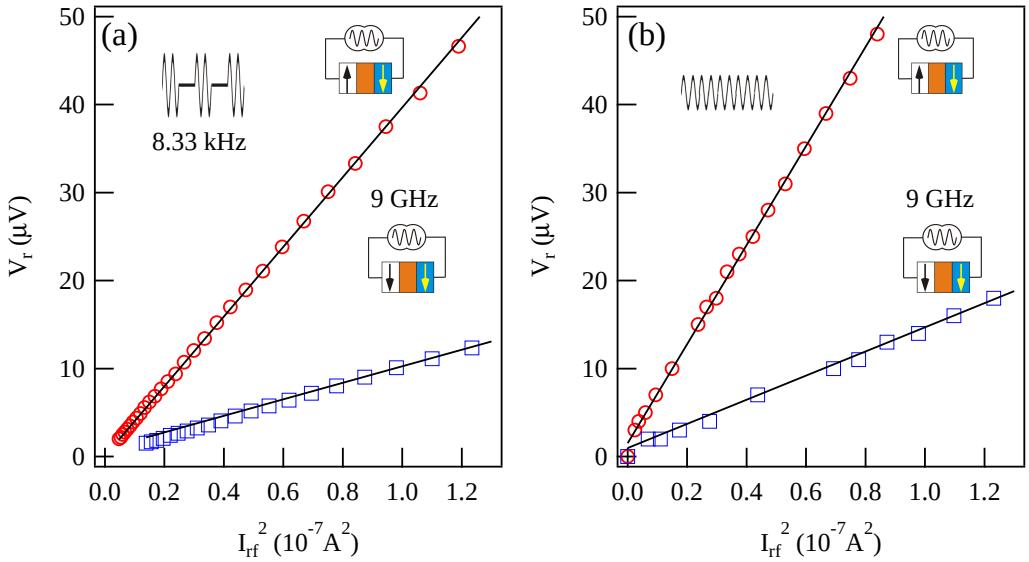

Figure 5.6: The rectification voltage V_r plotted against to the square of microwave current I_{RF}^2 on sample B at a (a) microwave current modified with 8.33 kHz or (b) continuous microwave current. Circles and squares are measured at the AP and P alignments of the MTJ, respectively. Lines are fits from the Eq. 5.6.

Figure 5.6(a) shows V_r as a function of I_{RF}^2. The measurement was taken on sample B. The red circles and blue rectangles are experimental results for AP and P states, respectively, and the black lines are linear fits. From Fig. 5.6(a), it is seen that V_r is proportional to I_{RF}^2 for both P and AP alignments as expected. The slopes of the curves in Fig. 5.6(a) denote the Seebeck coefficient at both P (S_P) and AP (S_{AP}) alignments, and S_{AP} is larger as S_P. The effect that the value of S_{AP} is larger

than S_P is also observed in static measurements where the samples were heated by a laser beam [50, 52].

To ensure that the modulation of the microwave power at 8.33 kHz would not induce any spurious effects in measuring the Seebeck rectification, measurements using continuous wave (CW) microwave were performed. Here, V_r is directly measured by using a dc voltage meter, at a constant incident microwave power P_{MW}. By noticing that without modulation the current I_{RF} is determined by $P_{MW} = (R + Z_0)^2 I_{RF}^2/8Z_0$, V_r was measured as shown in Fig. 5.6(b). The red circles and blue rectangles are experimental results for the AP and P states, respectively, and the black lines are linear fits. It is found that the results in Fig. 5.6(b) are in fairly good agreement with that of Fig. 5.6(a).

The theoretical values of the Seebeck coefficients of MTJs vary from 55 [132] to 150 μV/K [133] due to the fact that they are calculated by different theoretical approaches. Also, the experimental reported Seebeck coefficients vary with different samples. It was found that in an MTJ with a Al_2O_3 barrier, the Seebeck coefficient was on the order of 1000 μV/K [50] and in an MTJ with a MgO barrier, the value varies from 50 to 1300 μV/K [50, 52]. The Seebeck coefficient was estimated as 50 μV/K through dc transport experiments in the MTJs at the AP state [73]. This resulted in an estimated temperature difference of 1 K which corresponds to a 50 μV rectification voltage from Fig. 5.6(a). Since MTJs may have larger Seebeck coefficients, the temperature differences might be overestimated.

5.3 Magnetic control of rectification

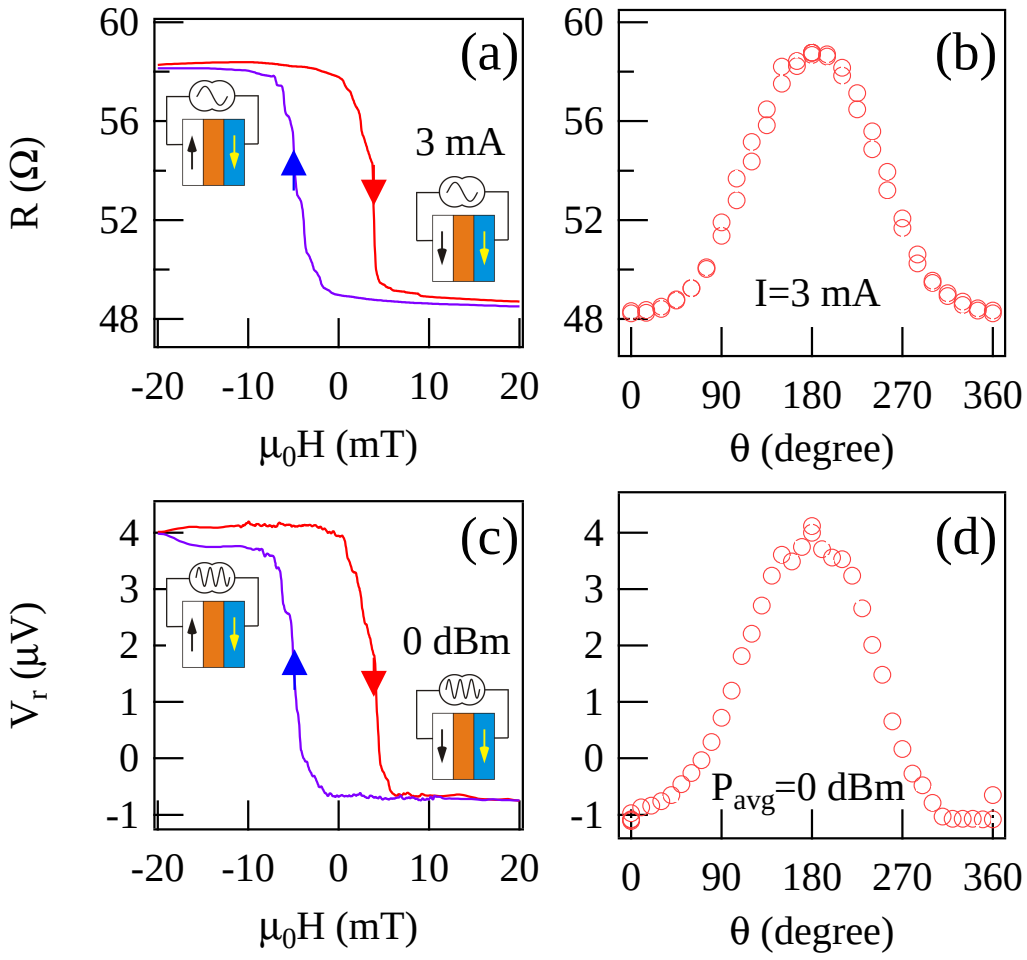

Figure 5.7: The TMR of sample A measured as a function of (a) the external magnetic field strength and (b) the field direction. The Seebeck rectification voltage measured at $\omega/2\pi = 10$ GHz as a function of (c) the external magnetic field strength and (d) the field direction.

As the observations in the previous sub-section, the Seebeck coefficient is related to the magnetization configurations, where S_{AP} is larger than S_P. This effect is similar to the magneto-resistance (R) of an MTJ, which has so far been the foundation of the applications of MTJs. It is worth noting that both of them originate from the density

of state of electrons which strongly depends on the magnetization configurations in an MTJ [77]. In the following experiments, it will be demonstrated more clearly that the Seebeck rectification of MTJs can be magnetically controlled.

Figures. 5.7(a) and (b) show the TMR of sample A measured at 384 Hz as a function of the field strength (H) and angle between two magnetizations of the two FM layers (θ), respectively. $R(H)$ in Fig. 5.7(a) is taken at $\theta = 0°$, while $R(\theta)$ in Fig. 5.7(b) is measured at $H = 10$ mT. The results are characteristics for MTJs showing that the TMR is determined by the relative direction of the magnetizations of the pinned and free layers [134]. In Figs. 5.7(c) and (d), the H and θ dependence of the Seebeck rectification V_r measured at $\omega/2\pi = 10.0$ GHz were plotted. Clearly, V_r can be also magnetically controlled.

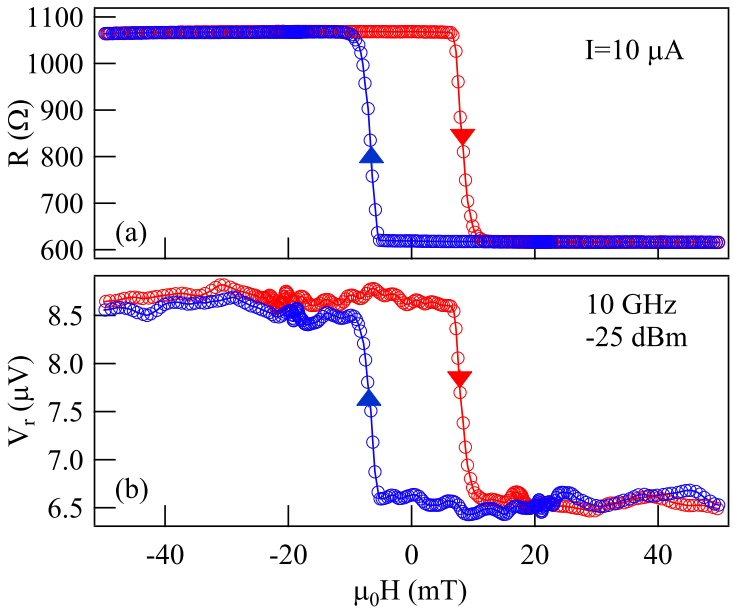

Figure 5.8: (a) The TMR of sample B measured as a function of the external magnetic field with a small current ($I = 10$ μA). (b) The Seebeck rectification voltage V_r measured at $\omega/2\pi = 10.0$ GHz as a function of (c) the external magnetic field strength and (d) the field direction.

Similar to MTJs from wafer A, the Seebeck effect in MTJs from wafer B can be controlled magnetically as well. The easy axis TMR loop of Sample B is shown in Fig. 5.8(a). The MTJs show single domain magnetization reversal. For comparison, the Seebeck rectification voltage V_r is plotted in Fig. 5.8(b). Here two sharp jumps in V_r appear at fields identical to where R jumps in the TMR loop. This magnetically controllable Seebeck rectification effect may open new ways for the application of MTJs in magnetically controllable thermal sensors.

5.4 Adjustment of Seebeck rectification via external heating methods

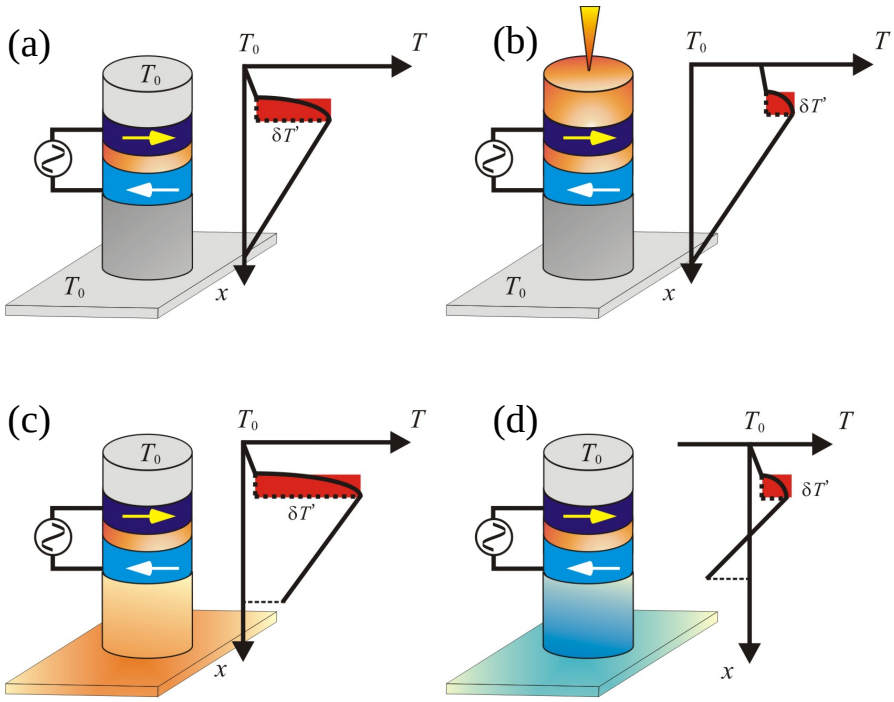

Figure 5.9: Sketches of the adjustment of temperature gradient established via microwave heating by adjusting the thermal boundary conditions using external heating methods. (a) A temperature gradient $\delta T'$ across the MgO layer of the MTJ is established by microwave heating. (b) The top electrode of the MTJ was heated by a laser beam. The temperature of the top surface is raised resulting in a decrease of $\delta T'$. (c) The bottom electrode of the MTJ is heated by a Peltier device attached to the bottom electrode. The temperature of the bottom electrode is thus raised, resulting in an increase of $\delta T'$. (d) The bottom electrode of the MTJ is cooled down by a Peltier device attached to the bottom electrode. The temperature of the bottom electrode is thus decreased, resulting in a decrease of $\delta T'$.

Equation 5.5 is the foundation of Seebeck rectification, but it is worth noting that other effects [119, 135] besides Seebeck rectification effect may contribute to the nonlinear I^2 term in Eq. 5.5. For example, an asymmetric of Fermi energies for two

FM layers will introduce an asymmetry of conductance as a function of an applied current, resulting in a rectified dc voltage when an ac current is applied [119]. Another example is the 'spin-diode' effect, where a dc voltage is rectified by the microwave current through the sample and the alternating resistance caused by this microwave current [135]. In this section, it will demonstrate that in the microwave regime, the nonlinear correction to Ohm's law is dominated by the Seebeck effect generated by an intrinsic heating. This was achieved by adjusting the Seebeck effect by using external heating methods.

Based on the TTC model, boundary conditions play an important role in the temperature profile, and thus in the Seebeck rectification effect as well. To verify the origin of microwave rectification in an MTJ under a microwave, The thermal boundary conditions were adjusted by introducing external temperature control techniques, which include a laser heating technique [52] and an external heating technique using a Peltier device.

As shown in Fig. 5.9(a), a temperature gradient $\delta T'$ is established by sending a microwave current into an MTJ. This $\delta T'$ decreases when the top surface of the MTJ is heated by a laser beam, as illustrated in Fig. 5.9(b). In contrast, this $\delta T'$ increases when the bottom surface of the MTJ is heated using a Peltier device attached as shown in Fig. 5.9(c). Similarly, this $\delta T'$ decreases when the bottom surface of the MTJ is cooled by a Peltier device attached as shown in Fig. 5.9(d). Since the Seebeck voltage is proportional to the temperature difference across the MTJ, an increase or decrease in $\delta T'$ corresponds to the enhancement or suppression of the Seebeck voltage.

Figure 5.10(a) shows the adjustment of the Seebeck rectification voltage using laser

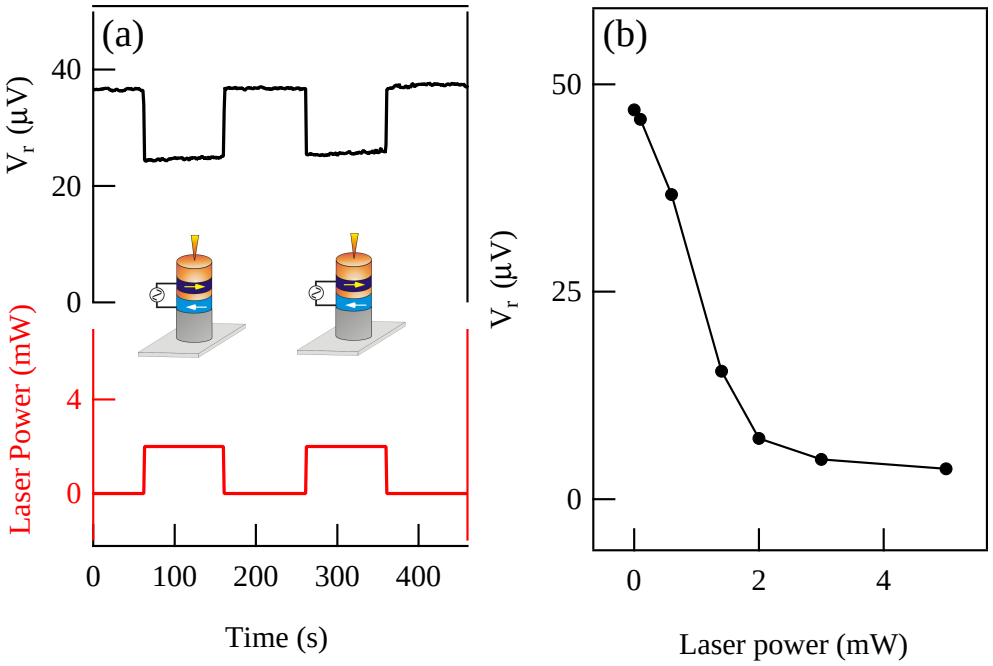

Figure 5.10: (a) The rectification voltage V_r can be adjusted by heating the top electrode of the MTJs with a laser beam. V_r is 38 and 22 μV when the laser is OFF (0 mW) and ON (2 mW), respectively. (b) V_r is suppressed by increasing the laser power. The total suppression of V_r indicates that the principle origin of V_r is the Seebeck effect.

heating, plotted as a function of time. The black curve on the top of Fig. 5.10(a) is the measured Seebeck voltage and the red curve on the bottom of Fig. 5.10(a) is the laser power applied to the sample. A microwave current at a frequency of 3.8 GHz with an incident power of 1 μW was sent into the MTJ through a coaxial cable at all times. A laser beam was focused on the top electrode of the MTJ sample with a diameter of less than 100 μm. The laser was turned, with a power of 2 mW, on for the periods from 50 to 150 s and 250 to 350 s, and turned off at other time intervals. The voltage V_r was suppressed when the laser was on and restored when the laser was off. The suppression of V_r, as expected, is the result of the decrease in the temperature

difference across the MTJ caused by laser heating.

Figure 5.10(b) shows the Seebeck rectification voltage as a function of laser power.The black line is a guide to the eye. By increasing the laser power, V_r is suppressed significantly. Most strikingly, the rectification voltage is almost completely suppressed when the laser power is larger than 3 mW, which indicates that V_r is dominated by the Seebeck effect, rather than other non-thermal [119, 135] mechanisms.

To control the temperature on the bottom side of the MgO barrier, the MTJ was attached to a Peltier-heating device using a thermally conductive adhesive. The temperature at the surface of Peltier-heating device was the same as the temperature on the bottom side of MTJ due to good thermal conductivity between the heating device and the MTJ. The temperature of the bottom surface could be controlled by adjusting the polarity and magnitude of the dc current sent into the Peltier device and was measured by a thermal sensor attached to it. When the bottom side of the sample was heated, the temperature gradient across the MgO barrier was enhanced as shown in Fig. 5.9(c). By contrast, when the bottom side of the sample was cooled, the temperature gradient across the MgO barrier was suppressed as shown in Fig. 5.9(d).

As expected, the enhancement or suppression of the Seebeck rectification voltage V_r by heating or cooling the bottom side of the MTJ was observed, as shown in Fig. 5.11. The experiment was done over a 500-second time interval, during which a microwave current at 5.8 GHz with an incident power of 200 μW was sent into the sample. Simultaneously, the bottom side of the MTJ was heated or cooled periodically. At the 60th second, the temperature of the bottom side of the sample was raised and, the temperature gradient across the MgO tunneling barrier was increased,

resulting in the enhancement of the rectification voltage. At 160s, the bottom side of the MTJ was cooled, resulting in a decrease of the temperature difference across the MTJ, and the suppression of V_r as shown in Fig. 5.11.

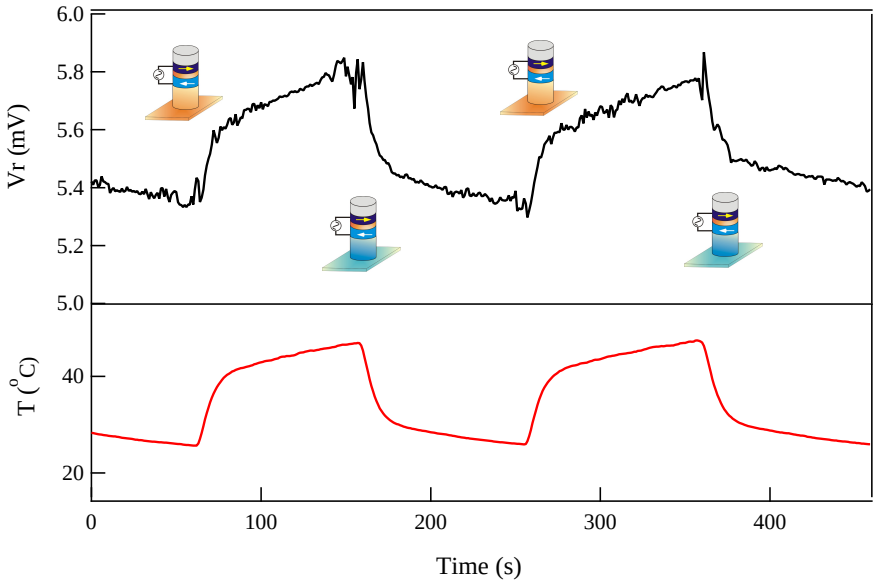

Figure 5.11: The rectification voltage V_r adjusted by external heating or cooling by a Peltier device attached to the bottom electrode of the MTJ. The temperature T was measured using a thermal couple attached to the bottom electrode of the MTJ. Both V_r and T were monitored and plotted as functions of time. V_r increased or decreased in response to the heating or cooling of the bottom electrode.

Figure 5.12 shows the change in voltage, ΔV_r, as a function of the temperature difference between the bottom and the top side. During the first 10 seconds of heating or cooling, it is assumed that the temperature of the bottom side, T_{bottom}, has changed, while the temperature of the top side, T_{top}, remains the same as the ambient temperature. The temperature difference between the bottom and the top side caused by external heating, $T_{bottom} - T_{top}$, resulted in a change in voltage ΔV_r, defined as $\Delta V_r = V_r(T_{bottom} - T_{top}) - V_r(0)$, where $V_r(0)$ is the voltage with no external heating or

cooling and $V_r(T_{bottom} - T_{top})$ is the voltage after heating or cooling. As what discussed above, an increase or decrease in the temperature difference across the MTJ results in the enhancement or suppression of V_r. As shown in Fig. 5.12, by increasing the temperature difference across the MTJ, the voltage V_r was increased (ΔV is positive) and vice versa. ΔV also depends on the magnetization configurations. In the AP configuration, the slope is larger compared to the slope in the P configuration, which corresponds to the different Seebeck coefficients for different configurations, and is consistent with previous results.

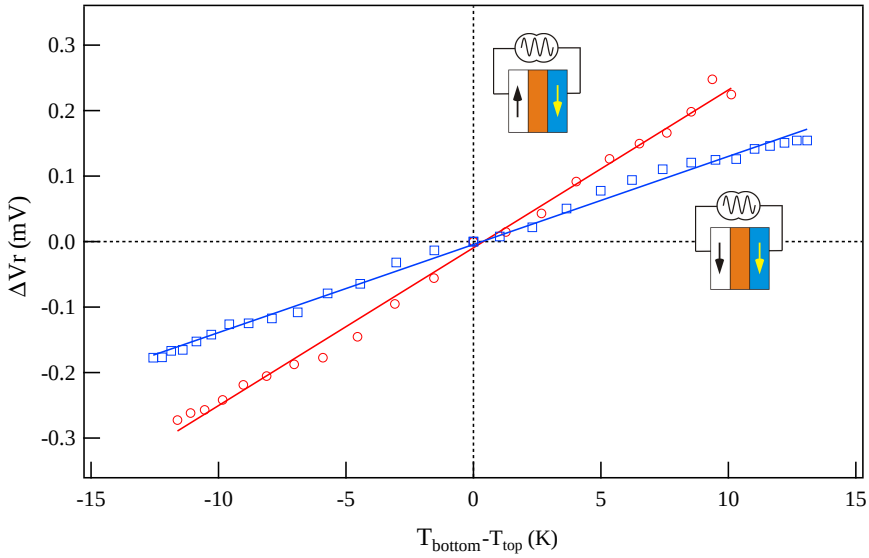

Figure 5.12: The change of rectification voltage ΔV_r as a function of the temperature difference of the bottom and top electrodes $T_{bottom} - T_{top}$. The red circle and blue rectangles denote the AP and P states, respectively.

5.5 Summary

In this chapter, an intrinsic thermoelectric coupling effect was found and this coupling contributes to a higher order term in the nonlinear correction to Ohm's

law in MTJs. This intrinsic thermoelectric coupling even exists in linear response regime, where only the first order driving forces (an electrochemical potential gradient and a temperature gradient) are involved. This nonlinear correction enables a novel Seebeck rectification effect which can be magnetically controlled. By varying the temperature gradient using an external thermal source, the thermal origin of the observed microwave rectification in MTJs is confirmed. This work refines the previous understanding of magneto-transport and microwave rectification in MTJs and forms a new foundation for utilizing spin caloritronics in high-frequency applications. Furthermore, the existence of thermal gradients encourages the exploration the thermal spin-transfer torque in MTJs, as will be demonstrated in the next chapter.

Chapter 6

Thermal spin-transfer torque in magnetic tunnel junctions

Traditionally, spin-transfer torque (STT) was generated by a spin-polarized current driven by a dc-bias voltage [33, 34]. The study of this dc-biased STT has demonstrated the capability to induce magnetization switching in MTJs [37, 38] . Pioneering work in the area of spin caloritronics found that a spin current can be driven by a temperature gradient [5]. Taking advantage of the development of spin caloritronics [45], a temperature gradient has been used to create spin currents, and their associated TSTT has been proposed for magnetization switching in magnetic materials [56] and in MTJs [61] theoretically. Although TSTT has not been experimentally demonstrated as capable of switching the magnetization in MTJs, the reduction of magnetization switching field under a TSTT has been observed at low temperatures recently [60]. The field-like TSTT was also observed by carefully analyzing the switching field in 2016 [107].

In this chapter, the impact of TSTT on the dynamic response occurring at ferromagnetic resonance (FMR) was studied at room temperature. The FMR spectra were measured electrically. The line shapes of FMR spectra were analyzed by varying the temperature difference across the MgO barrier. This temperature different was controlled by changing the power of a laser beam focused on one of the electrodes of MTJs. Evidence for the existence of TSTT in MTJs has been observed. It is found that the sum of the temperature differential of the in-plane and the out-of-plane TSTT is proportional to the temperature difference across the tunnel barrier. It is also found that the temperature differential of the in-plane and the out-of-plane TSTT is related to the relative angle of the magnetizations in the two FM layers. In addition, the magnetization orientation dependence of TSTT was measured and analyzed, which showed that this dependence differs from the magnetization orientation dependence of spin-transfer torque driven by a dc-bias. The work in this chapter has been published in *Physical Review B* [74].

6.1 Formalism of electrical detection of FMR with TSTT

Figure 6.1 shows a sketch of TSTT in an MTJ. The film is located in the $y-z$ plane and its easy axis is along the z direction. The positive x axis is from the fixed FM layer to the free FM layer. The magnetization of the free FM layer, $\mathbf{m}$, is excited by a microwave current to precess along its equilibrium position (z axis). This precession is governed by the Landau $-$ Lifshitz $-$ Gilbert (LLG) equation (Eq. 2.13). In the

coordinate system here, $\mathbf{m}$ is precessing along the z-axis with a cone angle $\delta\theta$; $\mathbf{M}$ is in the $y-z$ plane and has an angle of θ with the positive z axis. Thus, the angle between $\mathbf{m}$ and $\mathbf{M}$ is $\theta+\delta\theta$. However, since $\delta\theta$ is generally much smaller than θ, thus the angle between $\mathbf{m}$ and $\mathbf{M}$ is θ, approximately. The two components of spin-transfer torque (STT) in MTJs are named the in-plane and the out-of-plane STT, respectively. The in-plane torque, $\tau_{\parallel}$, is along the direction of $\hat{\mathbf{m}}\times(\hat{\mathbf{M}}\times\hat{\mathbf{m}})$, and the out-of plane torque, $\tau_{\perp}$, is along the direction of $\hat{\mathbf{M}}\times\hat{\mathbf{m}}$ [41]. Here $\hat{\mathbf{m}}$ and $\hat{\mathbf{M}}$ are the unit vectors of $\mathbf{m}$ and $\mathbf{M}$, respectively. From the definition of the direction of $\tau_{\parallel}$ and $\tau_{\perp}$, the relative angle between $\hat{\mathbf{m}}$ and $\hat{\mathbf{M}}$ influences the direction of the torques. Since both $\hat{\mathbf{M}}$ and $\hat{\mathbf{m}}$ are in the $y-z$ plane, the cross product $\hat{\mathbf{M}}\times\hat{\mathbf{m}}$ is along the x axis. The polarities of θ are defined to be the same as the polarities of $\hat{\mathbf{M}}\times\hat{\mathbf{m}}$, i.e., $\pi>\theta>0$ when $\hat{\mathbf{M}}\times\hat{\mathbf{m}}$ is along the positive x axis and $-\pi<\theta<0$ when $\hat{\mathbf{M}}\times\hat{\mathbf{m}}$ is along the negative x axis.

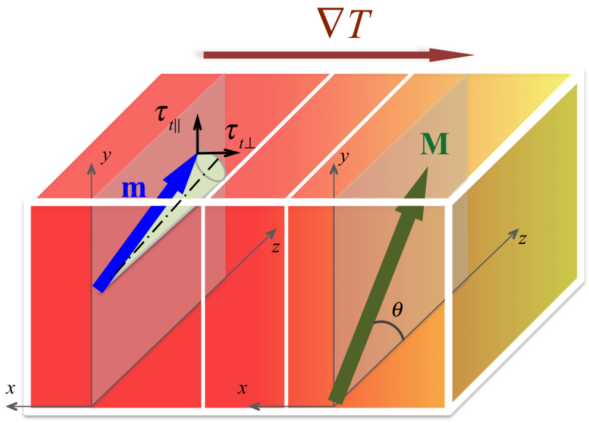

Figure 6.1: Sketch of the thermal spin-transfer torque in an MTJ. $\mathbf{M}$ and $\mathbf{m}$ are the magnetizations of the fixed and free layer respectively. $\tau_{t\parallel}$ and $\tau_{t\perp}$ are the in-plane and out-of-plane torques generated by the temperature gradient ∇T.

When a temperature difference is applied across the sample, TSTT makes a dis-

turbance, $\boldsymbol{\delta m}$, on $\hat{\mathbf{m}}$ as $\hat{\mathbf{m}} \approx (m_x e^{i\omega t} + \delta m_x)\hat{\mathbf{x}} + (m_y e^{i\omega t} + \delta m_y)\hat{\mathbf{y}} + (1 + \delta m_z)\hat{\mathbf{z}}$, where δm_x, δm_y, and δm_z are the three components of $\boldsymbol{\delta m}$ along the x, y, and z directions [59]. Thus, the cross product relating to the in-plane and out-of-plane torque turns out to be

$$\hat{\mathbf{M}} \times \hat{\mathbf{m}} = \sin\theta\hat{\mathbf{x}} + \delta m_x \cos\theta\hat{\mathbf{y}} - \delta m_x \sin\theta\hat{\mathbf{z}} + O(e^{i\omega t}), \tag{6.1}$$

and

$$\hat{\mathbf{m}} \times (\hat{\mathbf{M}} \times \hat{\mathbf{m}}) = \sin\theta\hat{\mathbf{y}} - \delta m_x \cos\theta\hat{\mathbf{x}} + \delta m_x \sin\theta\hat{\mathbf{z}} + O(e^{i\omega t}). \tag{6.2}$$

Since $\tau_\perp$ is dominant along x direction and $\delta m_i \ll m_i$ ($i = x, y$ or z), to a good approximation, we have

$$\boldsymbol{\tau}_\perp \approx \tau_\perp\hat{\mathbf{x}} + \tau_\perp \cdot \cot\theta \cdot \delta m_x \cdot \hat{\mathbf{y}}, \tag{6.3}$$

and

$$\boldsymbol{\tau}_\parallel \approx \tau_\parallel\hat{\mathbf{y}} - \tau_\parallel \cdot \cot\theta \cdot \delta m_x \cdot \hat{\mathbf{x}}. \tag{6.4}$$

Here, δm_x can be expressed as [59]

$$\delta m_x = \frac{1}{M_s} \sum_{\beta=\perp,\parallel} \chi_{x\beta} \frac{\partial \tau_{t,\beta}}{\partial T} \Delta T, \tag{6.5}$$

where $\tau_{t,\beta}$ is the in-plane ($\beta = \parallel$) and the out-of-plane ($\beta = \perp$) TSTT, and $\chi_{x\beta} = \frac{dm_x}{d\tau_{t,\beta}}$ is the magnetic susceptibility tensor of the free layer.

In the case with both dc-biased STT and TSTT, Eq. 2.13 turns out to be

$$\frac{d\hat{\mathbf{m}}}{dt} = -\gamma\hat{\mathbf{m}} \times \mathbf{H}_{\text{eff}} + \alpha\hat{\mathbf{m}} \times \frac{d\hat{\mathbf{m}}}{dt} - \frac{\gamma}{M_s}\widetilde{\tau}_y\hat{\mathbf{y}} - \frac{\gamma}{M_s}\widetilde{\tau}_x\hat{\mathbf{x}}, \tag{6.6}$$

where

$$\widetilde{\tau}_y = \tau_\parallel(I,\theta) - \tau_\perp(I,\theta)\cot\theta\left(\frac{1}{M_s}\sum_{\beta=\perp,\parallel} \chi_{x\beta}\frac{\partial \tau_{t,\beta}}{\partial T}\Delta T\right)$$

and

$$\widetilde{\tau_x} = \tau_\perp(I,\theta) + \tau_\parallel(I,\theta)\cot\theta(\frac{1}{M_s}\sum_{\beta=\perp,||}\chi_{x\beta}\frac{\partial\tau_{t,\beta}}{\partial T}\Delta T)$$

are STT at two directions.

Similarly as the deduction of rectification voltage V_r in the case with only a dc-biased STT as shown in Appendix A, V_r in the case with only TSTT is deduced as

$$\begin{aligned} V_r &= D\cdot\widetilde{D}(H) + L\cdot\widetilde{L}(H) \\ &= \frac{I_{RF}^2}{4M_s}(R_P - R_{AP})\sin\theta\sqrt{1+\frac{M_0}{H_r}}\frac{1}{\Delta H} \\ &\cdot\left[\widetilde{D}(H)\sqrt{1+\frac{M_0}{H_r}}\left(\left.\frac{d\tau_\perp}{dI}\right|_{I=0} - \left.\frac{d\tau_\parallel}{dI}\right|_{I=0}\cot\theta\cdot(\frac{1}{M_s}\sum_{\beta=\perp,||}\chi_{x\beta}\frac{\partial\tau_{t,\beta}}{\partial T}\Delta T)\right)\right. \\ &\left. - \widetilde{L}(H)\left(\left.\frac{d\tau_\parallel}{dI}\right|_{I=0} - \left.\frac{d\tau_\perp}{dI}\right|_{I=0}\cot\theta\cdot(\frac{1}{M_s}\sum_{\beta=\perp,||}\chi_{x\beta}\frac{\partial\tau_{t,\beta}}{\partial T}\Delta T)\right)\right]. \end{aligned} \tag{6.7}$$

Here $I = 0$ indicates there is no dc charge current, (i.e. no dc-biased STT), and D and L are the amplitudes of dispersive and Lorentz line shape, respectively. From Eq. 6.7, an FMR line shape is a combination of D and L, where D and L are

$$D = \frac{I_{RF}^2}{4M_s}(R_P - R_{AP})\sin\theta\left(1+\frac{M_0}{H_r}\right)\frac{1}{\Delta H}\left(\left.\frac{d\tau_\perp}{dI}\right|_{I=0} - \left.\frac{d\tau_\parallel}{dI}\right|_{I=0}\cot\theta\cdot(\frac{1}{M_s}\sum_{\beta=\perp,||}\chi_{x\beta}\frac{\partial\tau_{t,\beta}}{\partial T}\Delta T)\right)$$

and

$$L = \frac{I_{RF}^2}{4M_s}(R_P - R_{AP})\sin\theta\sqrt{1+\frac{M_0}{H_r}}\frac{1}{\Delta H}\left(\left.\frac{d\tau_\parallel}{dI}\right|_{I=0} - \left.\frac{d\tau_\perp}{dI}\right|_{I=0}\cot\theta\cdot(\frac{1}{M_s}\sum_{\beta=\perp,||}\chi_{x\beta}\frac{\partial\tau_{t,\beta}}{\partial T}\Delta T)\right),$$

respectively.

At zero dc bias, $\frac{d\tau_\perp}{dI}$ was observed near zero [41], thus the ratio between the dispersive and Lorentz line shape, D/L, due to TSTT has a form as

$$D/L = \frac{1}{M_s}\sqrt{1+\frac{M_0}{H_r}}\cdot\cot\theta\cdot\sum_{\beta=\perp,||}\chi_{x\beta}\frac{\partial\tau_{t,\beta}}{\partial T}\Delta T. \tag{6.8}$$

D/L reflects the relation between FMR line shape and TSTT and is a key feature which will be studied systematically. By comparing the resonance spectra under only a dc bias ($I \neq 0$) to the spectra with neither a dc bias nor a temperature difference ($I = 0$ and $\Delta T = 0$), the properties of dc-biased STT can be revealed. Similarly, by comparing the resonance spectra under only a temperature difference ($\Delta T \neq 0$) to the spectra with neither a dc bias nor a temperature difference is present ($I = 0$ and $\Delta T = 0$), the properties of TSTT can be revealed. In a TSTT case, at a certain θ, D/L is expected to be proportional to ΔT as indicated by Eq. 6.8. By contrast, in a dc-biased STT case, from Eq. 2.22, D/L is proportional to the ratio of the perpendicular and parallel 'torkances' ($d\tau_{\parallel}/dI$ and $d\tau_{\perp}/dI$). Since both the in-plane and the out-of-plane torkances are proportional to $\sin\theta$ [41], D/L is independent to θ .

6.2 Experimental methods

The sketch of the circuit for electrically detecting FMR in MTJs is shown in Fig. 3.5. A microwave current was sent into the MTJ through a coaxial cable, and a magnetic field was applied in the plane of the MTJ films to set the angle between two magnetizations in the FM layers. The resonance field is determined by the frequency of the microwave. By sweeping the magnetic field through the resonance position, a resonance signal will be observed. Here the positive voltage is defined from the free layer to the fixed layer and the fixed layer is connected to ground. To study dc-biased STT, a dc bias was applied across the barrier of an MTJ to drive a dc-biased STT, as shown in Fig. 3.5. By measuring the FMR with a dc bias, the effect of a dc-biased

STT on the FMR can be observed.

By contrast, to study the TSTT, a temperature difference was applied across the MTJ by heating the electrode near the free layer by using a laser beam, as shown in Fig. 3.6. The positive temperature gradient was defined as the temperature decreases from the free layer to the fixed layer.

The temperature difference, ΔT, established by laser heating was estimated by measuring the Seebeck voltage, V_S. A laser beam was focused on the electrode of the MTJ and the current across the sample was measured by the lock-in technique. The left axis in Fig. 6.2 shows the measured current, I_{Laser}, when increasing the laser power, P_L, focused on the MTJ. The corresponding voltage, V_S, was calculated and plotted in Fig. 6.2 as well (right axis). Then ΔT was estimated as $\Delta T = V_S/S$, where the Seebeck coefficient S was evaluated as 50 μV/K based on the previous work [73].

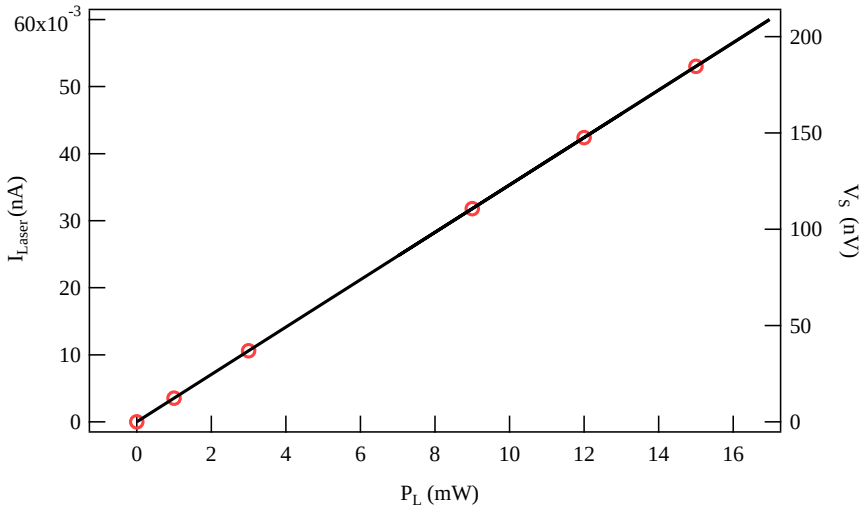

Figure 6.2: Estimation of the temperature difference across an MTJ by laser heating. The red hollow circles are measurement data and the black line is a linear fit.

In this chapter, to detect TSTT, a microwave current was required to generate

FMR. This microwave current, as was discussed in chapter 5, also introduced a temperature difference across the tunnel junction. However, to reduce the complexity, the magnitude of the microwave current was fixed but the temperature difference across the MgO barrier was adjusted by changing the power of the laser. Furthermore, the magnitude of the microwave current was on the order of 10 μA, which induced a temperature difference of 0.01 mK. In comparison, the temperature difference caused by the laser heating was much larger, which was on the order of several mK. Thus, only the temperature difference caused by the laser heating is considered in this chapter.

As discussed in chapter 6.1, there are two components of STT, related to the cross product $\mathbf{m} \times (\mathbf{M} \times \mathbf{m})$ and $\mathbf{M} \times \mathbf{m}$. Thus the relative angle between $\mathbf{M}$ and $\mathbf{m}$, θ, will affect the STT. θ is set by adjusting the angle (φ) between the external magnetic field (H) and the easy axis of the MTJ, and by adjusting the amplitude of H. Figure 6.3(a) shows the resistance loop of the MTJ (Sample 663-2 with a 126×63 nm^2 elliptic shape) measured by sweeping the magnetic field at $\varphi = 0^\circ$ (gray) and $\varphi = 60^\circ$ (red), respectively.

At large positive H, the angle θ is near 0° and the resistance R is at the minimum value of 5136 Ω, point A in Fig. 6.3(a) for example. When sweeping H from positive to negative, a switching is observed at $H = -10.6$ mT where the magnetization in free FM layer, $\mathbf{m}$, switches to the opposite direction and θ is near 180°, thus the resistance at that time is at the maximum value of 7792 Ω, for example, at point B in Fig. 6.3(a). As H increases negatively, the magnetization in the fixed layer, $\mathbf{M}$, will rotate towards H and then θ will decrease from $\theta = 180^\circ$ resulting in a decrease of resistance . θ at a certain H can be calculated according to Eq. 2.3. For example,

the resistance at point C is 7494 Ω, thus θ at point C is 140.8° with $R_P = 5136$ Ω and $R_{AP} = 7792$ Ω.

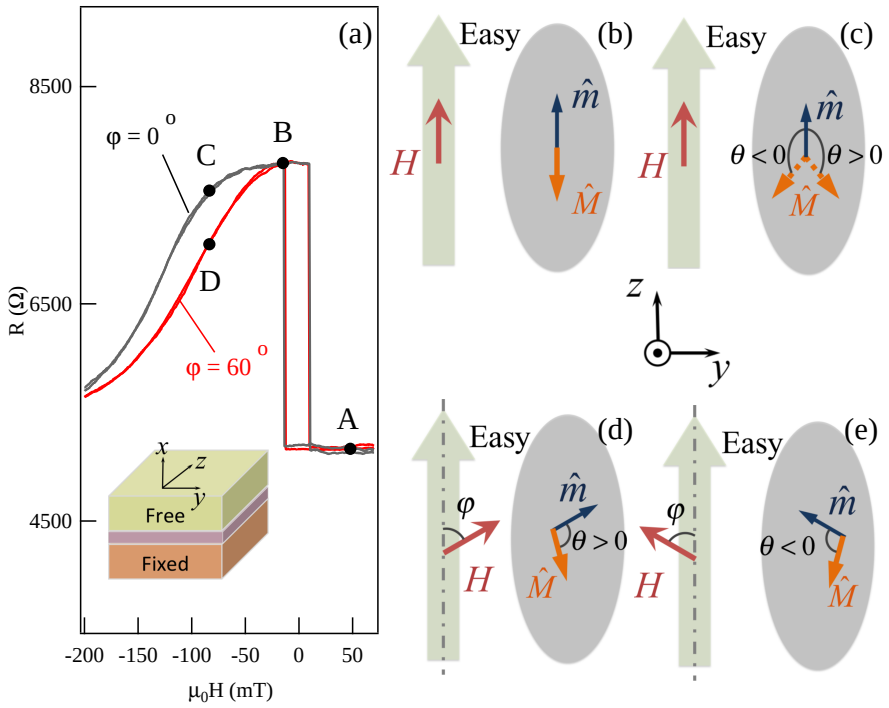

Figure 6.3: (a) The resistance loops as a function of H of the MTJ at $\varphi = 0°$ (gray) and $\varphi = 60°$ (red). There are four points marked as A,B, C and D. (b) and (c) are the sketches of the configuration of **m** and **M** corresponding to point B and C respectively. (d) and (e) are the sketches of the configuration of **m** and **M** corresponding to point D when $\theta > 0$ and $\theta < 0$, respectively.

Figure 6.3(b) shows the anti-parallel configuration corresponding to point B in Fig. 6.3(a), where the external magnetic field H is along the direction of the easy axis. By increasing H, **M** will start rotating to the direction of H in y-z plane. An anti-clockwise rotation will result in a positive θ, and a clockwise rotation will result in a negative θ as shown in Fig. 6.3(c). To set θ with determined polarity, the relative position of **M** and **m** are controlled by setting H in different directions relative to

the easy axis. As shown in Fig. 6.3(d), when the projection of H on the y-axis is positive, **M** will prefer to rotate anti-clockwise, thus θ is positive as H is increased. By contrast, as shown in Fig. 6.3(e), when the projection of H on the y-axis is negative, **M** will prefer to rotate clockwise, thus θ is negative as H is increased.

6.3 Thermal spin-transfer torque in MTJs

In this section, TSTT is observed through FMR line shape changes. The MTJ measured has an elliptical cross section with a dimension of 126×63 nm^2. The frequency of the microwave current sent into the MTJ was 6.91 GHz, with an amplitude of $I_{RF} = 12.6$ μA. FMR was detected electrically when sweeping the magnetic field H. A laser beam was focused on the surface of the MTJ to generate a temperature difference ΔT up to 3 mK. θ was set to positive (91°) and negative ($-101°$) angles to study the angular dependence of the FMR signal.

θ was set to 91° first. Figure 6.4(a) shows the rectification voltage V_r as a function of the magnetic field near the resonance field H_r. The gray dots are the raw FMR spectra, and the black lines are fit curves using Eq. 6.7. When $\Delta T = 0$ mK, the FMR curve was Lorentz dominant, with $D = 138.5$ μV and $L = -671.8$ μV thus $D/L = -0.21$. The small dispersive component is attributed to the interlayer exchange coupling between the two FM layers [85, 136]. When $\Delta T = 3$ mK, the dispersive component increased relative to the Lorentz component, with $D = 30.2$ μV and $L = -44.9$ μV, thus $D/L = -0.67$. To clearly show the two line shape components, D and L were normalized by the maximum of L. The normalized dispersive and Lorentz components D_{Norm} and L_{Norm} were plotted against $H - H_r$ in

Fig. 6.4(b). Figure 6.4(b) shows that the Lorentz components were always negative. When $\Delta T = 0$ mK, the dispersive component was positive. When $\Delta T = 3$ mK, the negative amplitude of the dispersive component increased by three times compared to the case when $\Delta T = 0$ mK.

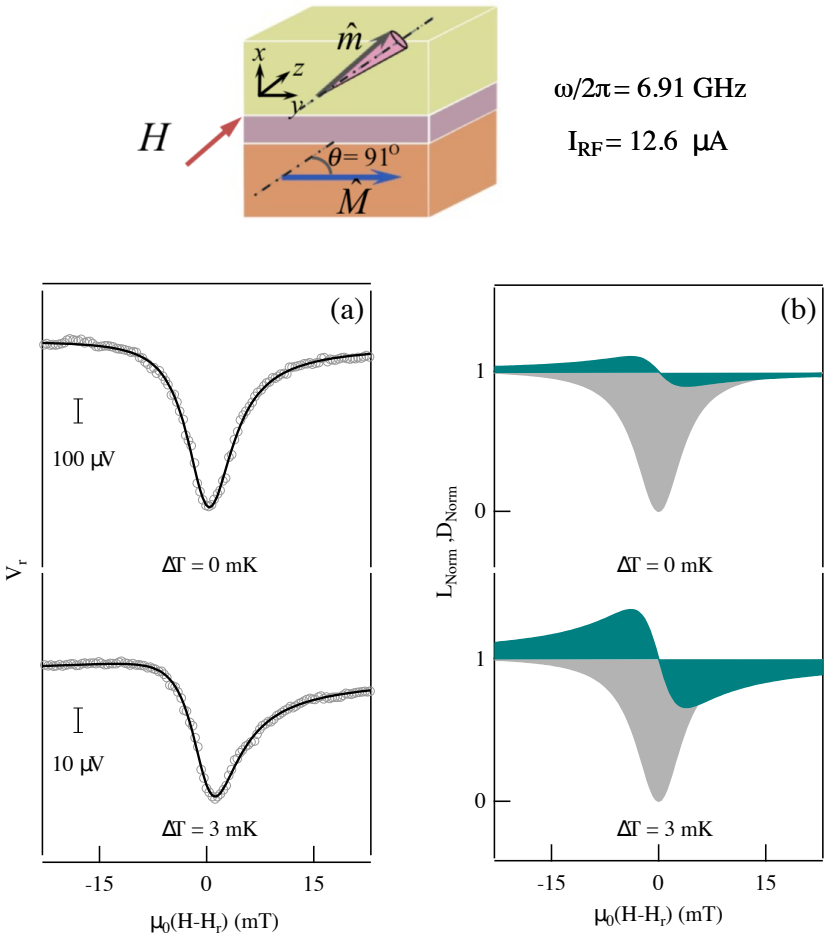

Figure 6.4: The top sketch depicts the coordinates and magnetization configuration at $\theta = 91°$ (a) The FMR line shape at $\Delta T = 0$ and $\Delta T = 3$ mK. The gray dots are the measurement results and the black lines are fits with a sum of dispersive and Lorentz components. (b) The Lorentz (gray) and dispersive (dark cyan) components normalized by the amplitude of L at $\Delta T = 0$ and $\Delta T = 3$ mK, respectively.

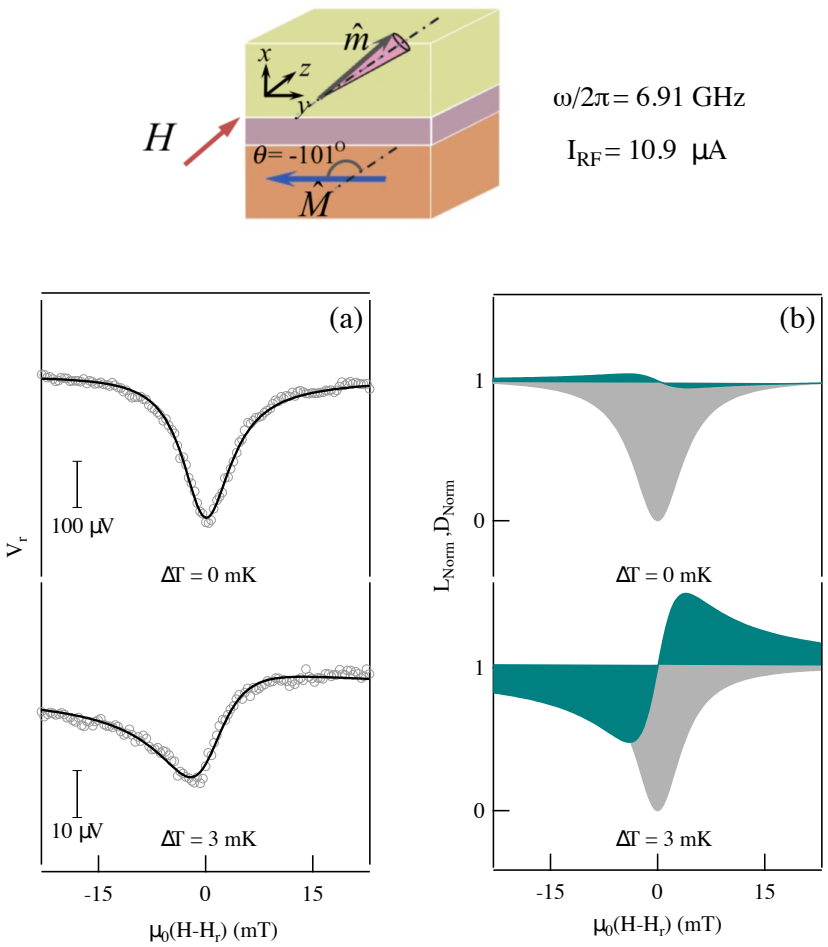

Figure 6.5: The top sketch depicts the coordinates and the magnetization configuration at $\theta = -101°$ (a) The FMR line shape at $\Delta T = 0$ and $\Delta T = 3$ mK. The gray dots are the measurement results and the black lines are the fits using Eq. 6.7. (b) The Lorentz (gray) and dispersive (dark cyan) components normalized by the amplitude of L at $\Delta T = 0$ and $\Delta T = 3$ mK, respectively.

θ was then set to $-101°$. The frequency of the microwave current sent into the MTJ remained 6.91 GHz, with an amplitude of 10.9 μA. Figure 6.5(a) shows the rectification voltage V_r as a the function of magnetic field near the resonance field H_r at $\theta = -101°$. The gray dots in Fig. 6.5(a) are the raw FMR spectra, and the black curves are fit curves using Eq. 6.7. The normalized dispersive and Lorentz

component D_{Norm} and L_{Norm} were plotted against $H - H_r$ in Fig. 6.5(b), indicating that the Lorentz components are always negative. When $\Delta T = 0$ mK, the line shape is Lorentz dominant with a negative dispersive component, and when $\Delta T = 3$ mK, the dispersive component becomes positive. When $\Delta T = 0$ mK, $D = 29.1$ μV and $L = -306.7$ μV thus $D/L = -0.09$, and when $\Delta T = 3$ mK, $D = -13.9$ μV and $L = -13.6$ μV, thus $D/L = 1.0$.

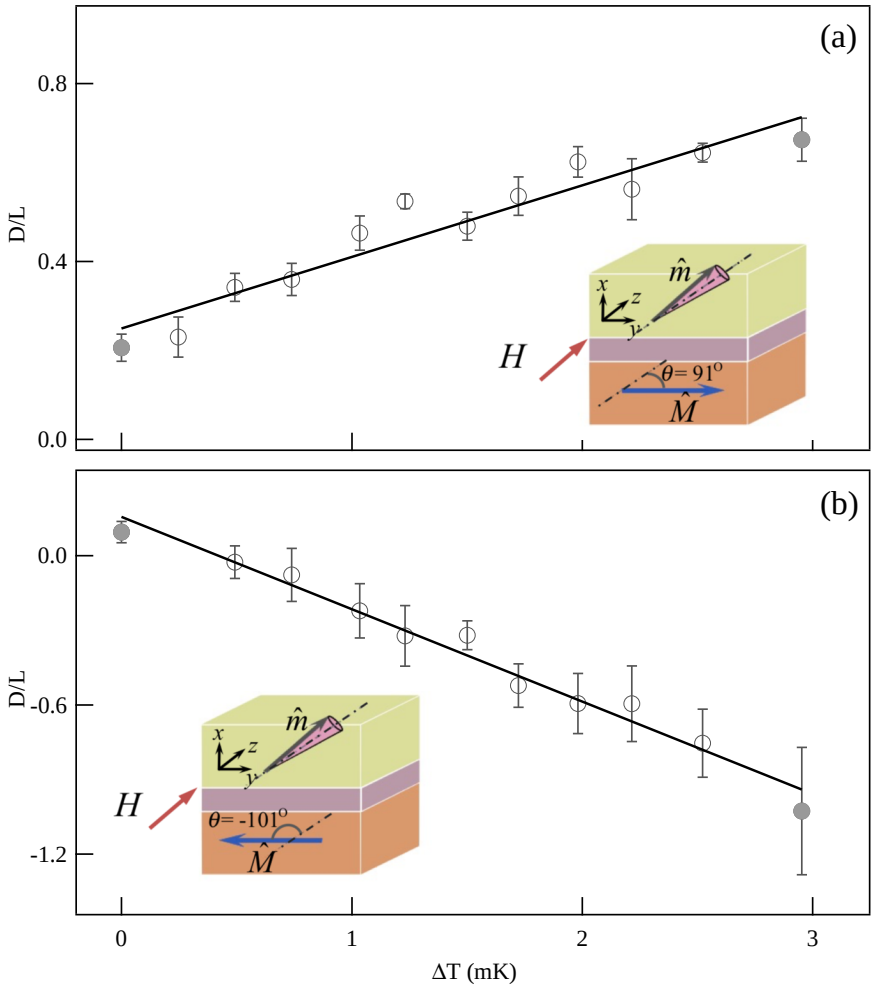

Figure 6.6: D/L at various ΔT at (a) $\theta = 91°$ and (b) $\theta = -101°$. The solid gray dots are the values corresponding to $\Delta T = 0$ and 3 mK.

Figures 6.6(a) and (b) show D/L at various ΔT values from 0 to 3 mK at $\theta = 91°$ and $\theta = -101°$, respectively. D/L is linear dependent to ΔT. This linear dependence of D/L on ΔT is consistent with the expectation as shown in Eq. 6.8. In addition, D/L increases at $\theta = 91°$ but decreases at $\theta = -101°$ with an increasing ΔT. In the next section, it will be shown that the trend of the D/L change produced by a dc-biased STT is different from the change produced by TSTT.

6.4 Dc-biased spin-transfer torque in MTJs

In this section, dc-biased STT was observed by analyzing the FMR line shape changes. First, θ was set to 91°, and the magnitude of the microwave current, I_{RF}, was set at 12.6 μA. Figure 6.7(a) shows V_r as a function of magnetic field near the resonance field H_r. The gray dots are the raw FMR spectra, and the black lines are fit curves using Eq. 6.7. The normalized magnitudes of the dispersive and Lorentz line shape components D_{norm} and L_{norm} were plotted in Fig. 6.7(b), from which it can be seen that the FMR line shape was adjusted by the dc-biased STT for both positive and negative dc currents. In all three cases, there were dominant negative Lorentz components while the sign of the dispersive component was determined by the polarity of the dc voltage bias V_{dc}. At $V_{dc} = 248$ mV, the dispersive component was positive, and at $V_{dc} = -248$ mV, the dispersive component was negative.

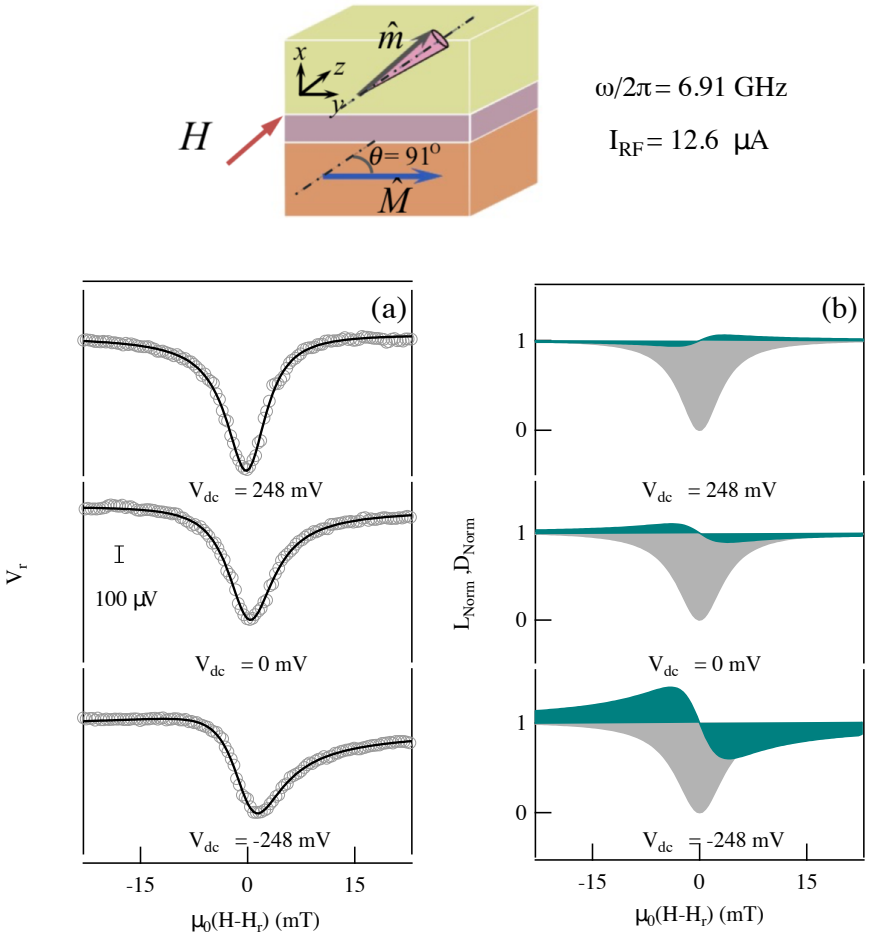

Figure 6.7: The top sketch depicts the coordinates and the magnetization configuration at θ =91° (a) The FMR line shape evolution with the dc bias V_{dc} at different polarities. The FMR spectrum with no dc bias is in the middle while the FMR spectra for positive and negative dc biases are on the top and bottom, respectively. The gray dots are the measurement results, and the black lines are fits of the data by Eq. 6.7. (b) The Lorentz (gray) and dispersive (dark cyan) components of the FMR spectra normalized by L.

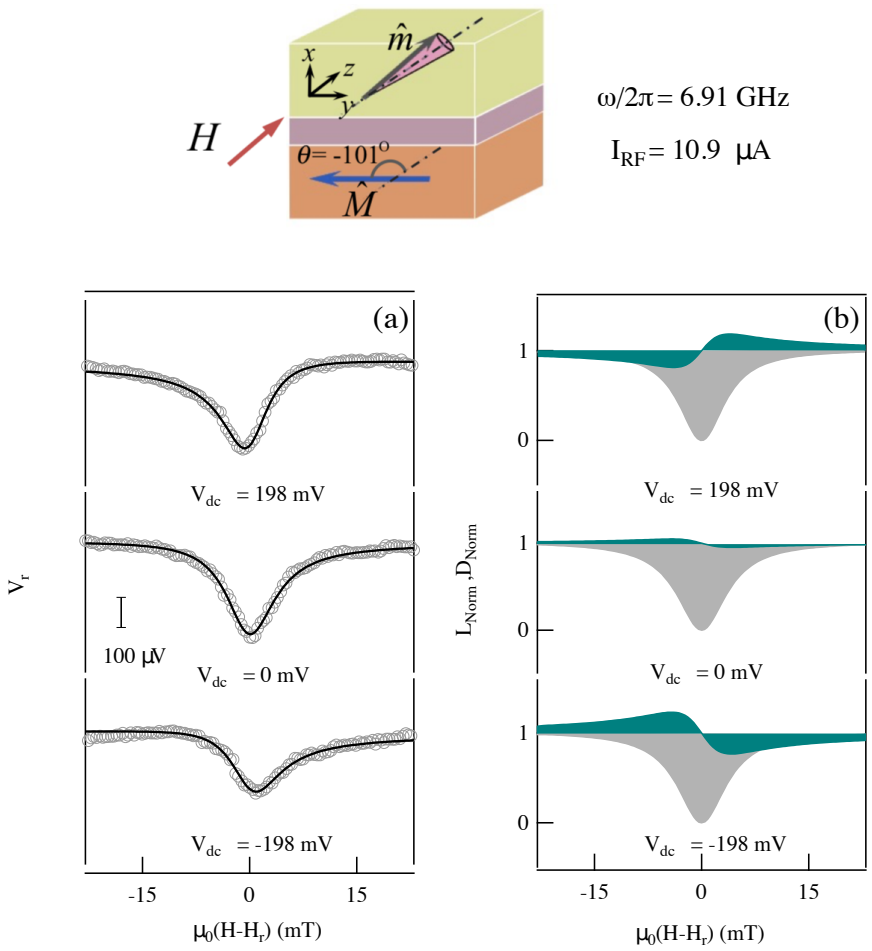

Figure 6.8: The top sketch depicts the coordinates and the magnetization configuration at $\theta = -101°$ (a) The FMR line shape evolution with the dc bias V_{dc} at different polarities. The FMR spectrum with no dc bias is in the middle while the FMR spectra for positive and negative dc biases are on the top and bottom, respectively. The gray dots are the measurement results, and the black lines are fits of the data by Eq. 6.7. (b) The Lorentz (gray) and dispersive (dark cyan) components of the FMR spectra normalized by L.

Setting θ to $-101°$, and $I_{\rm RF}$ to 10.9 μA, Figure 6.8(a) shows V_r as a function of magnetic field near the resonance field H_r. The gray dots in Fig. 6.5(a) are the raw FMR spectra and the black curves are fits using Eq. 6.7. The normalized D and L were plotted in Fig. 6.8(b), from which one can see that the FMR line shape

was affected by dc-biased STT at both positive and negative polarities. At all three dc biases, there was a dominant negative Lorentz component, and the sign of the dispersive component was determined by the polarity of the dc voltage bias V_{dc}. At $V_{dc} = 198$ mV, the dispersive component was positive, and at $V_{dc} = -198$ mV the dispersive component was negative.

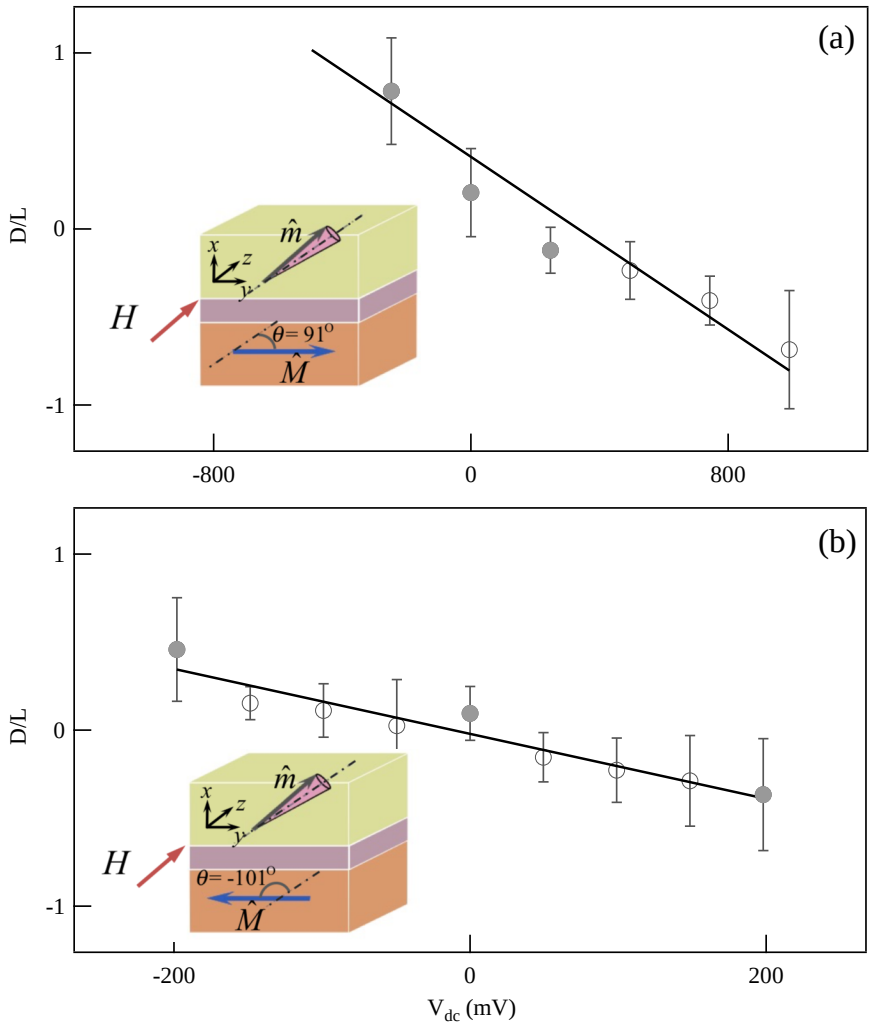

Figure 6.9: D/L at various V_{dc} for (a) $\theta = 91°$ and (b) $\theta = -101°$. The solid gray dots are the values corresponding to V_{dc} plotted in Figs. 6.7 and 6.8. The black line is a linear fit.

Figure 6.9(a) shows D/L as a function of V_{dc} from which it can be seen that D/L increases negatively at positive bias and positively at negative bias at $\theta = 91°$. Figure 6.9(b) shows the same trend of D/L as a function of V_{dc} at $\theta = -101°$. In the dc-biased STT case, the trend of D/L by increasing current is not dependent to θ, which is what expect to be seen from Eq. 2.22. By contrast, the trend of D/L by increasing temperature difference is dependent to θ. The different trend of D/L in dc-biased and thermal STT gives a way to distinguish these two kinds of torques. The angular dependence of D/L will be discussed in more details in the next section.

6.5 Angular dependence under dc-biased STT and thermal STT

In previous sections, the different trends of D/L were observed at various temperature differences and dc-biases. These measurements were taken at both positive and negative θ values, which already showed that D/L under TSTT was related to the polarity of θ, while D/L under dc-biased STT was not.

In this section, the trends of D/L under dc-biased and thermal STT were systematically studied for values of θ ranging from -180 to $180°$. In total, ten sets of measurements were done at five positive angles and five negative angles. All the FMR spectra for both the TSTT and dc-biased STT case were fit using Eq. 6.7.

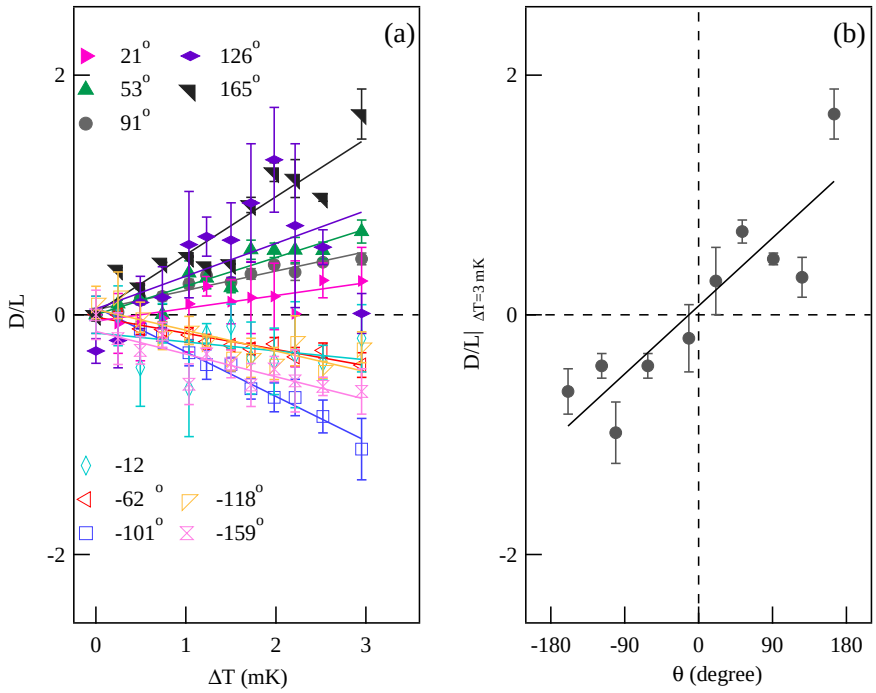

Figure 6.10: (a) D/L as a function of ΔT at various θ angles. The solid dots correspond to positive θ and the hollow dots correspond to negative θ. The lines represent linear fits for each θ angle. (b) D/L as a function of θ at $\Delta T = 3$ mK. The black line is a guide to the eye.

Figure 6.10(a) shows D/L as a function of ΔT at various θ angles. The lines are linear fits since Eq. 6.8 indicates that D/L has a linear dependence on ΔT. From the fits, one can see that the slope of D/L as ΔT increases is positive for $0° < \theta < 180°$, but negative for $-180° < \theta < 0°$.

Figure 6.10(b) shows the angular dependence of D/L at $\Delta T = 3$ mK. The solid line in this figure is a guide to the eye to show the general trend. D/L has a negative value when $-180° < \theta < 0°$, and a positive value when $0° < \theta < 180°$. D/L is larger at 180° than at 0°. It was shown that TSTT is larger in the AP state than in the P state by observing the reduction of switching field due to TSTT at low temperatures [60],

indicating that TSTT is larger at $\theta = 180°$ than at $\theta = 0°$. Essentially, from Eq. 6.8, the angular dependence of D/L indicated that the in-plane and out-of-plane thermal torkances, $d\tau_{t||}/dT$ and $d\tau_{t\perp}/dT$, are related to θ, although how these torkances link to θ is still unclear.

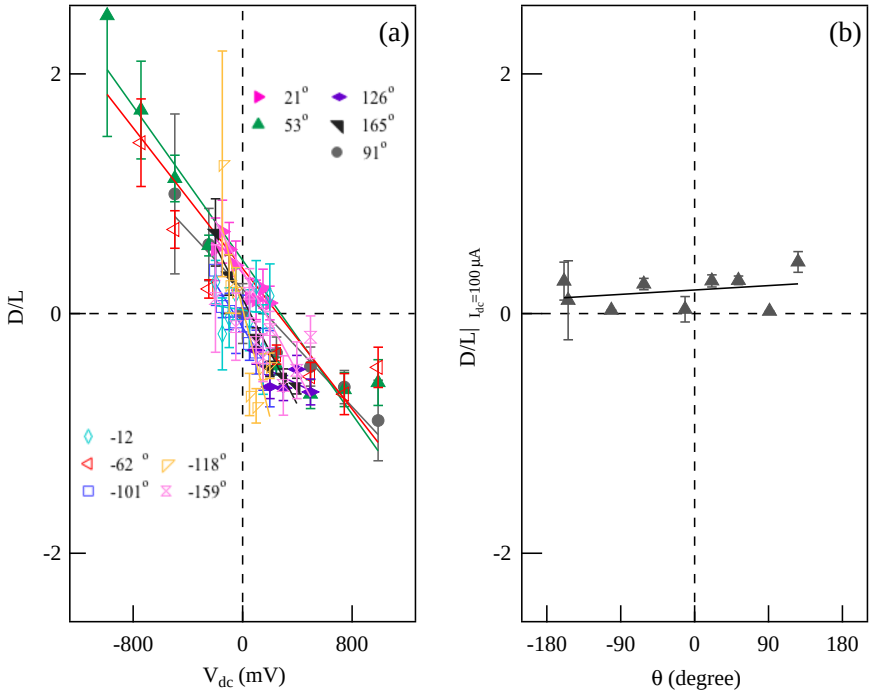

Figure 6.11: (a) D/L as a function of V_{dc} at various θ angles. The solid dots correspond to positive θ and the hollow dots correspond to negative θ. The lines represent the linear fits for each θ angle. (b) D/L as a function of θ at $I_{dc} = 100$ μA. The black line is a guide to the eye.

Similarly, dc-biased STT induced FMR line shape changes were summarized in Fig. 6.11(a). Figure 6.11(a) shows D/L as a function of V_{dc} at the same θ as in Fig. 6.10(a). The solid lines are linear fits. At both positive and negative θ angles, the slopes of D/L as V_{dc} increases are always negative.

Figure 6.11(b) shows the angular dependence of D/L at a constant dc current at

I_{dc} =100 μA. The solid line in this figure is a guide to the eye to show the general trend. For all angles, D/L is always positive and has a nearly constant value compared to the strong θ dependence of D/L induced by TSTT (Fig. 6.10(b)).

The angular dependence of D/L in dc-biased STT case was consistent with Ref. [41]. They performed measurements at angles between 45 to 90° and found that the ratio between the in-plane and the out-of-plane torkance was nearly constant between these angles. As shown in Eq. 2.22, D/L is proportional to $\frac{d\tau_\perp/dI}{d\tau_\parallel/dI}$. It was shown that both torkances are $\sin\theta$ dependent [41], thus the ratio between them is θ independent, resulting in an angular independence of D/L in the dc-biased STT case.

In summary, both TSTT and dc-biased STT increase by increasing the temperature difference ΔT and the dc voltage ΔV, respectively. The sum of the temperature differential of the in-plane and the out-of-plane TSTT is linearly dependent to ΔT; by contrast, both the in-plane and the out-of-plane dc-biased STT are proportional to $\sin\theta$. In consequence, TSTT is dependent on the relative angles of the magnetizations in two FM layers and these dependencies are different from the angular dependence in dc-biased STT.

6.6 Comparison of temperature and temperature difference effects

In this section, the temperature dependence of electrically detected FMR through global external heating was studied and it concluded that the thermal effect observed above by FMR line shape changes is not caused by absolute temperature rises.

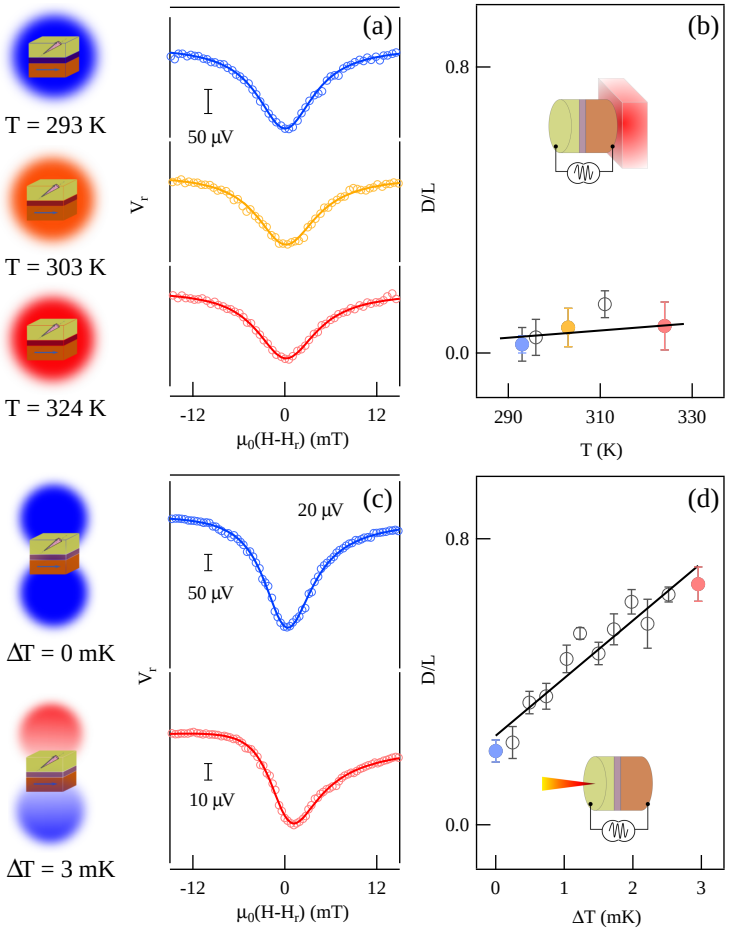

Figure 6.12: In the left column, the sketches show that the samples were set at various temperatures or have a temperature difference between the top and the bottom side. (a) The FMR spectra for three different temperatures. (b) D/L of the FMR spectra at various temperatures. The black line is a guide to the eye, and the blue, yellow, and red solid dots are D/L at the three temperatures shown in (a). (c) The FMR spectra at different temperature differences ΔT. (d) D/L at various ΔT. The black line is a guide to the eye and the blue and solid red dots are D/L for ΔT values of 0 and 3 mK corresponding to the cases in (c).

In the measurements, the MTJ was heated by an external heating device attached to the electrode near the fixed layer, and at each temperature, the sample was heated to equilibrium by waiting for 20 minutes. The temperature of the sample was detected using a thermocouple attached near the surface of the electrodes.

Figure 6.12(a) shows V_r as a function of the magnetic field near FMR resonance, H_r, at three different temperatures. θ was set to 52° and the I_{RF} was 86 μA. The line shape change was indicated by D/L and plotted in Fig. 6.12(b), from which it can be seen that the line shape does not change significantly with increasing temperature.

For comparison, the laser heating spectra performed at $\theta = 91°$ discussed in chapter 6.3 was replotted in Fig. 6.12(c), and D/L as a function of ΔT was plotted in Fig. 6.12(d). By comparing Figs. 6.12(b) and (d), one can see that D/L is very sensitive to ΔT but not to T. A ΔT as small as 3 mK makes a significant change in D/L while a temperature increase of up to 30 K has only minimal impact on D/L.

Joule heating induced by the microwave current in the MTJs was also excluded. In the laser heating case, the FMR line shapes before and after laser heating were compared, and the effects of Joule heating in these two cases are the same because the magnitude of the microwave current was fixed. Thus, Joule heating is not involved in the line shape change in the study where the difference in FMR line shape before and after laser heating.

After considering the effects of temperature dependence and Joule heating on the FMR line shape, it can conclude that the FMR line shape changes observed during laser heating are mainly caused by TSTT generated by a temperature difference, but not absolute temperature.

6.7 Summary

In this chapter, a system was built to generate a temperature difference across an MTJ by laser heating, and a TSTT was generated by this temperature difference.

The TSTT was observed by detecting the FMR electrically, and analyzing the FMR line shape change. It is found that the sum of the temperature differential of the in-plane and the out-of-plane TSTT is proportional to the temperature difference across the tunnel barrier, and both components are related to the relative angle of the magnetizations in the two FM layers. In addition, the angular dependence of TSTT was found to be different from the dc-biased STT. This difference provides a way to distinguish TSTT and dc-biased STT. All these features above are supported by the calculation derived from the LLG equation, by including STT and TSTT. This work has a general interest to the spintronics community since it demonstrates that electrically detected FMR can be used as a sensitive tool for the measurement of TSTT in MTJs and since it provides an experimental support for the study of the mechanisms and for the potential applications of TSTT.

Chapter 7

Conclusion and future work

In this thesis, the coupling of charge, spin, and heat flows in electron transport in MTJs was studied. Firstly, in chapter 4, the current dependent magnetoresistance was studied. It was observed that the TMR ratio decreased as an increasing current was applied to the MTJs. This decrease was attributed to a reduction of spin polarization in the free FM layer, caused by exchange interactions between the spin current and the localized magnetic momentum in the FM layer. Based on this hypothesis, a formula was deduced to describe the decrease of TMR ratio. This formula links the magnetoresistance and TMR ratio to two key parameters in MTJs, which are the spin-polarization in the FM layer and the threshold current (I_c) for magnetization switching, without considering the complicated details in the interfaces of the tunnel barrier and FM layers. Using these formulas, experimental observations of the resistance change due to an applied current were well explained and the value of I_c could be determined at different magnetization configurations, as well as at temperatures ranging from 8 to 300 K.

In addition to the study of static transport properties, dynamic transport properties were investigated in MTJs by studying intrinsic thermoelectric coupling. In chapter 5, it was found that an intrinsic thermoelectric coupling effect contributes to a nonlinear correction to Ohm's law in MTJs. This intrinsic thermoelectric coupling exists even in the linear response regime, where the charge and heat currents are driven by first order driving forces, i.e. electrochemical potential and temperature gradients. This nonlinear correction enables a novel Seebeck rectification effect, which can be controlled magnetically. This work refines the previous understanding of magneto-transport and microwave rectification in MTJs and presents a method for utilizing spin caloritronics in high-frequency applications.

Encouraged by the study of the thermoelectric coupling effect, in chapter 6, it was focused on the study of thermal spin-transfer torque (TSTT) in MTJs. A temperature difference across the tunnel barrier was generated successfully by heating an MTJ with a focused laser beam. This temperature difference drives a spin current to apply TSTT on the magnetization in the free FM layer. To observe this TSTT, electrical detection of ferromagnetic resonance (FMR) was employed, and FMR spectra were detected as a dc voltage signal. By analyzing the FMR line shape, the existence of TSTT in MTJs was observed. It was found that the sum of the temperature differential of the in-plane and the out-of-plane TSTTs are proportional to the temperature difference across the tunnel barrier. In addition, the temperature differential of the in-plane and the out-of-plane TSTTs are related to the relative angle between the magnetizations of the two FM layers. This angular dependence is not found in dc-biased STT, which provides a way to distinguish TSTT and dc-biased STT. Starting

from the Landau-Lifshitz-Gilbert equation, by considering STT, formulas predicting the dc voltage of electrical detected FMR were derived. These formulas explain most of the experimental results very well. This work provides experimental support for the study of the mechanisms of TSTT and demonstrates that electrical detection of FMR is a sensitive tool for the measurement of TSTT in MTJs. Thus, this work has a general interest to the spintronics community.

Based on the work in this thesis, many topics still remain to be studied in the future. Some of these are as follows:

The application of Seebeck rectification as a microwave sensor

The work on the Seebeck rectification effect provides possibilities in applications, such as non-destructive detection and microwave imaging [75]. Compared with the spin diode effect in MTJs, Seebeck rectification is effective in a broadband frequency range (preliminary results showed a range up to 40 GHz) without any external magnetic field, which would greatly reduce the hardware requirement of imaging systems.

At present, a single MTJ device attached to a mechanical stage is employed in each imaging system [75]. The data acquisition time is limited by the speed of the mechanical scan, which may be improved in future studies. The nano-scale size of MTJ devices promises the possibility to fabricate MTJ arrays, which are already used in magnetoresistive random-access memories (MRAMs). Redesigned MTJ arrays thus could be used in microwave imaging systems. These sensor arrays could work as electro-optical devices, which could greatly reduce data acquisition time. In addition, such a system would be more robust since no mechanical motion is required.

Frequency dependence of the magnetoresistance/capacitance effect and

Seebeck rectification

The discoveries of the spin diode and Seebeck rectification effects in MTJs under microwave radiation enables MTJs to be applied in microwave detectors and even in radio frequency power harvesting circuits. Yet difficulties in making qualitative measurements of the frequency dependent magnetotransport in MTJs has hampered understanding and hence limited the use of these techniques. Impedance spectroscopy may be a straightforward way to investigate the frequency dependent magnetotransport properties. However, this research is not easy, especially for measurements performed at the GHz range in nanostructured MTJ devices, because an on-chip coplanar waveguide and a highly precise microprobe are required to deliver microwave current into the device.

The dynamic spintronic group at the UofM has an advanced probe station system with a superconducting magnet (up to 1 Tesla) which is able to produce temperatures from 4.2 to 400 K. By combining this probe station system with the electrical detection technique used in this thesis, one would be able to precisely characterize the impedance as functions of frequency, magnetic field, and temperature. Such measurements would allow us to model the high-frequency response of MTJs by taking into account the screening effect caused by the accumulation of charge at the MTJ interfaces. This knowledge would help to optimize the broadband microwave detector based on the Seebeck rectification effect in MTJs.

Quantify TSTT vectors in MTJs

In order to use TSTT to reorient the magnetization in MTJs, a quantitative measurement of both the magnitude and direction of TSTT in MTJs is required.

In this thesis, It has been demonstrated an effective method to observe TSTT by analyzing the FMR line shapes measured by the electrical detection technique. It was also showed that controllable temperature differences across the tunnel barrier can be achieved using an adjustable laser heating technique. Based on the high sensitivity of this approach in studying TSTT, in the future, one can systematically measure both the magnitude and direction of TSTT in MTJs, and hence deduce the TSTT vectors, which is of fundamental interest for data storage.

Manipulating the magnetization switching fields in MTJs by TSTT

As the existence of TSTT has been clearly observed in this thesis, the manipulation of the magnetization switching field in MTJs is now possible to be studied. At present, directly switching the magnetizations using TSTT is difficult since the temperature gradient across the MTJs is on the order of several mK/nm, which is much smaller than the predicted gradient necessary (0.2 K/nm [56]). Based on this work, one can systematically measure the reduction of the magnetization switching field by introducing TSTT. This study would provide a better understanding of TSTT and push forward the application of TSTT in MTJ-based MRAMs. Optimized techniques for generating temperature differences across the tunnel barriers in MTJs would assist this study. For example, in this thesis, measurements were taken at static temperature differences in equilibrium, and in the future, a pulse laser beam may produce larger temperature differences [52, 137], and thus generate larger TSTT.

Appendix A

Derivative of the rectification voltage V_r with STT

In chapter 2.3.1, the rectification voltage V_r was deduced as the form of $V_r = \frac{1}{4} I_{RF}(R_P - R_{AP}) \sin\theta |m_y|$. To get the value of V_r, m_y is required to be calculated.

The magnetization of the free layer $\mathbf{m}$ is precessing around the $\hat{z}$ direction, thus by ignoring the slight change in the z component, $\mathbf{m}$ can be written as

$$\mathbf{m} = \left(m_x e^{i\omega t}, m_y e^{i\omega t}, m_z\right), \tag{A.1}$$

where m_x, m_y, and m_z are the three components of magnetization in the orthogonal coordinate as shown in Fig. 6.1. Normalizing the three components of $\mathbf{m}$ by dividing by m_z taking $m_z \simeq M_s$, where M_s is the saturated magnetization of the free layer, the unit vector of $\mathbf{m}$ can be represented as:

$$\hat{\mathbf{m}} = \left(m_x e^{i\omega t}, m_y e^{i\omega t}, 1\right), \tag{A.2}$$

where $m_x = m_x/M_s$ and where $m_y = m_y/M_s$. Similarly, since the magnetization of

the fixed layer is in the $y-z$ plane, the unit vector of the fixed layer's magnetization $\hat{\mathbf{M}}$ can be represented as:

$$\hat{\mathbf{M}} = (0, \sin\theta, \cos\theta)\,, \tag{A.3}$$

where θ is the angle made by $\hat{\mathbf{m}}$ and $\hat{\mathbf{M}}$. Precession of $\hat{\mathbf{m}}$ changes θ,whose direction cosine can be written as:

$$\begin{aligned}\cos\theta(t) = \hat{\mathbf{m}}\cdot\hat{\mathbf{M}} &= \mathrm{Re}(m_x e^{i\omega t}, m_y e^{i\omega t}, 1)\cdot(0, \sin\theta, \cos\theta)\\ &= \cos\theta + \sin\theta \mathrm{Re}(m_y e^{i\omega t}).\end{aligned} \tag{A.4}$$

By comparing with a Taylor expansion of $\cos\theta(t)$ at θ,

$$\cos\theta(t) = \cos\theta - \sin\theta\delta\theta,$$

we have

$$\delta\theta = -\mathrm{Re}(m_y e^{i\omega t}). \tag{A.5}$$

The LLG equation (Eq. 2.8) for a vector magnetization $\hat{\mathbf{m}}$ with STT is [41, 97]

$$\frac{d\hat{\mathbf{m}}}{dt} = -\gamma\hat{\mathbf{m}}\times\mathbf{H}_{\text{eff}} + \alpha\hat{\mathbf{m}}\times\frac{d\hat{\mathbf{m}}}{dt} - \gamma\frac{\tau_{\parallel}(I,\theta)}{M_s}\frac{\hat{\mathbf{m}}\times(\hat{\mathbf{M}}\times\hat{\mathbf{m}})}{|\hat{\mathbf{M}}\times\hat{\mathbf{m}}|} - \gamma\frac{\tau_{\perp}(I,\theta)}{M_s}\frac{\hat{\mathbf{M}}\times\hat{\mathbf{m}}}{|\hat{\mathbf{M}}\times\hat{\mathbf{m}}|}, \tag{A.6}$$

where $\tau_{\parallel}(I,\theta)$ and $\tau_{\perp}(I,\theta)$ is the in-plane and the out-of-plane STT, respectively.

Then, each term in Eq. 6.6 can be written separately as,

$$\begin{aligned}-\gamma\hat{\mathbf{m}}\times\mathbf{H}_{\text{eff}} &\approx \gamma\left[(N_x M_s + H)m_x\hat{\mathbf{y}} - (N_y M_s + H)m_y\hat{\mathbf{x}}\right]e^{i\omega t},\\ \alpha\hat{\mathbf{m}}\times\frac{d\hat{\mathbf{m}}}{dt} &\approx i\alpha\omega(m_x\hat{\mathbf{y}} - m_y\hat{\mathbf{x}})e^{i\omega t},\\ \tau(I,\theta) &= \tau^0 + \frac{d\tau}{dI}I_{RF}e^{i\omega t} - \frac{d\tau}{d\theta}m_y e^{i\omega t},\end{aligned}$$

where N_x,N_y are the demagnetization factor on x and y direction, respectively. Combining individual terms and ignoring constant terms gives us:

$$i\omega m_x = -m_y\gamma(N_yM_s + H) - im_y\alpha\omega - \frac{\gamma}{M_s}(\frac{d\tau_\perp}{dI}I_{RF} - \frac{d\tau_b}{d\theta}m_y), \tag{A.7}$$

$$i\omega m_y = m_x\gamma(N_xM_s + H) - im_x\alpha\omega - \frac{\gamma}{M_s}(\frac{d\tau_\parallel}{dI}I_{RF} - \frac{d\tau_b}{d\theta}m_y), \tag{A.8}$$

which leads to

$$\begin{aligned}&\begin{pmatrix} i\omega & (\gamma N_yM_s + \gamma H + i\alpha\omega) - \frac{\gamma}{M_s}\frac{d\tau_\perp}{d\theta} \\ -(\gamma N_xM_s + \gamma H + i\alpha\omega) & i\omega - \frac{\gamma}{M_s}\frac{d\tau_\parallel}{d\theta} \end{pmatrix}\begin{pmatrix} m_x \\ m_y \end{pmatrix} \\ &= -\frac{\gamma}{M_s}I_{RF}\begin{pmatrix} \frac{d\tau_\perp}{dI} \\ \frac{d\tau_\parallel}{dI} \end{pmatrix}.\end{aligned} \tag{A.9}$$

Let $A = -(\gamma N_xM_s + \gamma H + i\alpha\omega)$, $B = (\gamma N_yM_s + \gamma H + i\alpha\omega) - \frac{\gamma}{M_s}\frac{d\tau_\perp}{d\theta}$, and $C = i\omega - \frac{\gamma}{M_s}\frac{d\tau_\parallel}{d\theta}$, then we have

$$\begin{pmatrix} m_x \\ m_y \end{pmatrix} = -\frac{\gamma I_{RF}}{M_s}\frac{1}{i\omega C - AB}\begin{pmatrix} C & -B \\ -A & i\omega \end{pmatrix}\begin{pmatrix} -\frac{d\tau_\perp}{dI} \\ \frac{d\tau_\parallel}{dI} \end{pmatrix}. \tag{A.10}$$

1) When there is no STT and no damping, we have

$$\begin{pmatrix} i\omega & (\gamma N_yM_s + \gamma H) \\ -(\gamma N_xM_s + \gamma H) & i\omega \end{pmatrix}\begin{pmatrix} m_x \\ m_y \end{pmatrix} = \begin{pmatrix} 0 \\ 0 \end{pmatrix}. \tag{A.11}$$

In order to have non-zero solution of m_x and m_y, the determinant of the equation coefficient matrix should be zero:

$$\begin{vmatrix} i\omega & (\gamma N_yM_s + \gamma H) \\ -(\gamma N_xM_s + \gamma H) & i\omega \end{vmatrix} = 0. \tag{A.12}$$

It gives us the relation between resonant frequency ω and resonant field H for FMR in this situation:

$$\omega^2 = (\gamma N_x M_s + \gamma H_r)(\gamma N_y M_s + \gamma H_r qasx) \approx \gamma^2 H_r(H_r + M_0), \tag{A.13}$$

with $M_0 \equiv (N_x + N_y)M_s \approx N_x M_s$ and $H_r = \frac{1}{2}(-M_0 + \sqrt{M_0^2 + 4\omega^2/\gamma^2})$ the resonant position of applied magnetic field when there is no STT and no damping [138].

2) In the free layer of the MTJs, the demagnetization along x-axis is dominated, i.e. $N_y \ll N_x \sim 1$, and $\alpha \ll 1$, the denominator in Eq. A.10, $i\omega C - AB$, can be written as:

$$i\omega C - AB = 2\gamma^2 H_r(H - H_r + i\Delta H), \tag{A.14}$$

where

$$\Delta H = \alpha\sqrt{\frac{1 + M_0}{H_r}}(H_r + M_0/2). \tag{A.15}$$

Then, from Eq. A.10, it can be obtained that

$$m_y = -\frac{I_{RF}}{2M_s}\frac{\sqrt{1 + M_0/H_r}}{(H - H_r + i\Delta H)} \cdot \left[\sqrt{1 + M_0/H_r}\left(\frac{d\tau_\perp}{dI}\right) + i\left(\frac{d\tau_\parallel}{dI}\right)\right], \tag{A.16}$$

Therefore, the voltage V_r can be expressed as:

$$V_r = \frac{I_{RF}^2}{4M_s}(R_P - R_{AP})\sin\theta\sqrt{1 + \frac{M_0}{H_r}}\frac{1}{\Delta H} \cdot \left[\widetilde{D}(H)\sqrt{1+\frac{M_0}{H_r}}\left(\frac{d\tau_\perp}{dI}\right) - \widetilde{L}(H)\left(\frac{d\tau_\parallel}{dI}\right)\right]. \tag{A.17}$$

The amplitudes of dispersive and Lorentz components D and L are:

$$D = \frac{I_{RF}^2}{4M_s}(R_P - R_{AP})\sin\theta\left[1 + \frac{M_0}{H_r}\right]\frac{1}{\Delta H}\left(\frac{d\tau_\perp}{dI}\right) \tag{A.18}$$

and

$$L = -\frac{I_{RF}^2}{4M_s}(R_P - R_{AP})\sin\theta\sqrt{1 + \frac{M_0}{H_r}}\frac{1}{\Delta H}\frac{d\tau_\parallel}{dI}. \tag{A.19}$$

Thus, the ratio of dispersive and Lorentz amplitudes, D/L, is

$$D/L = \sqrt{1 + \frac{M_0}{H_r} \left. \frac{d\tau_\perp/dI}{d\tau_\parallel/dI} \right|_{I_0=V/R}}, \tag{A.20}$$

where V is the voltage bias and R is the resistance of an MTJ.

Appendix B

Publication List

B.1 U.S. Patent Application

Can-Ming Hu, Yongsheng Gui, **Zhaohui Zhang**, Hong Guo. Seebeck rectification enabled by intrinsic thermoelectric coupling in magnetic tunneling junctions. *United States Patent Pending*, No.: US 20150221847 A1, Aug. 6, 2015.

B.2 Papers

Z.H. Zhang, Y. S. Gui, L. Fu, X. L. Fan, J. W. Cao, D. S. Xue, P. P. Freitas, D. Houssameddine, S. Hemour, K. Wu, and C.-M. Hu, Seebeck Rectification Enabled by Intrinsic Thermoelectrical Coupling in Magnetic Tunneling Junctions, Phys. Rev. Lett. **109**, 037206 (2012).

Z.H. Zhang, L. H. Bai, C.-M. Hu, S. Hemour, K. Wu, X. L. Fan, D. S. Xue, and D. Houssameddine, The tunneling magnetoresistance current dependence on cross

sectional area, angle and temperature, AIP Adv. **5**, 037134 (2015).

Z.H. Zhang, L. H. Bai, X. B. Chen, H. Guo, X. L. Fan, D. S. Xue, D. Houssameddine, and C.-M. Hu, Observation of thermal spin-transfer torque via ferromagnetic resonance in magnetic tunnel junctions, Phys. Rev. B, **94**, 064414 (2016).

Bibliography

[1] J. M. D. Coey. *Magnetism and Magnetic Materials*. (Cambridge University Press, 2010).

[2] A. H. Morrish. *The Physical Principles of Magnetism*. (Wiley, 2001).

[3] *IBM 350 disk storage unit*. `http://www-03.ibm.com/ibm/history/exhibits/storage/storage_350.html`.

[4] L. Mearian. *WD ships world's first 10TB helium-filled hard drive*. `http://www.computerworld.com/article/3011142/data-storage/wd-ships-worlds-first-10tb-helium-filled-hard-drive.html`.

[5] M. Johnson and R. H. Silsbee. Thermodynamic analysis of interfacial transport and of the thermomagnetoelectric system. *Physical Review B*, 35:4959, 1987.

[6] N. F. Mott. The resistance and thermoelectric properties of the transition metals. *Proceedings of the Royal Society of London. Series A, Mathematical and Physical Sciences*, 156:368, 1936.

[7] A. Fert and I. A. Campbell. Two-current conduction in nickel. *Physical Review Letters*, 21:1190, 1968.

[8] M. N. Baibich, J. M. Broto, A. Fert, F. Nguyen Van Dau, F. Petroff, P. Etienne, G. Creuzet, A. Friederich, and J. Chazelas. Giant magnetoresistance of (001) Fe/(001) Cr magnetic superlattices. *Physical Review Letters*, 61:2472, 1988.

[9] G. Binasch, P. Grünberg, F. Saurenbach, and W. Zinn. Enhanced magnetoresistance in layered magnetic structures with antiferromagnetic interlayer exchange. *Physical Review B*, 39:4828, 1989.

[10] S. A. Wolf, D. D. Awschalom, R. A. Buhrman, J. M. Daughton, S. von Molnár, M. L. Roukes, A. Y. Chtchelkanova, and D. M. Treger. Spintronics: a spin-based electronics vision for the future. *Science*, 294:1488, 2001.

[11] J. M. Daughton. Magnetic tunneling applied to memory (invited). *Journal of Applied Physics*, 81:3758, 1997.

[12] J. Åkerman. Toward a Universal Memory. *Science*, 308:508, 2005.

[13] W. Thomson. On the electro-dynamic qualities of metals:–effects of magnetization on the electric conductivity of nickel and of iron. *Proceedings of the Royal Society of London*, 8:546, 1856.

[14] A. Moser, K. Takano, D. T. Margulies, M. Albrecht, Y. Sonobe, Y. Ikeda, S. Sun, and E. E. Fullerton. Magnetic recording: advancing into the future. *Journal of Physics D: Applied Physics*, 35:R157, 2002.

[15] S. Maekawa and T. Shinjo. *Spin dependent transport in magnetic nanostructures*. (CRC Press, 2002).

[16] D. L. L. Mills and J. A. C. Bland. *Nanomagnetism: ultrathin films, multilayers and nanostructures*, volume 1. (Elsevier, 2006).

[17] C. Chappert, A. Fert, and F. Nguyen Van Dau. The emergence of spin electronics in data storage. *Nature Materials*, 6:813, 2007.

[18] M. Julliere. Tunneling between ferromagnetic films. *Physics Letters A*, 54:225, 1975.

[19] H. Kubota, A. Fukushima, Y. Ootani, S. Yuasa, K. Ando, H. Maehara, K. Tsunekawa, D. D. Djayaprawira, N. Watanabe, and Y. Suzuki. Evaluation of spin-transfer switching in CoFeB/MgO/CoFeB magnetic tunnel junctions. *Japanese Journal of Applied Physics, Part 2: Letters*, 44, 2005.

[20] Z. T. Diao, D. Apalkov, M. Pakala, Y. Ding, A. Panchula, and Y. M. Huai. Spin transfer switching and spin polarization in magnetic tunnel junctions with MgO and AlO x barriers. *Applied Physics Letters*, 87(23):1, 2005.

[21] S. Ikeda, J. Hayakawa, Y. Ashizawa, Y. M. Lee, K. Miura, H. Hasegawa, M. Tsunoda, F. Matsukura, and H. Ohno. Tunnel magnetoresistance of 604% at 300 K by suppression of Ta diffusion in CoFeB/MgO/CoFeB pseudo-spin-valves annealed at high temperature. *Applied Physics Letters*, 93:2508, 2008.

[22] P. Bose, P. Zahn, J. Henk, and I. Mertig. Tailoring TMR ratios by ultrathin magnetic interlayers: A first-principles investigation of Fe/MgO/Fe. *MRS Proceedings*, 1183:77, 2009.

[23] J. Åkerman. *Handbook of Spin Transport and Magnetism.* (CRC Press, 2011).

[24] B. Hughes. Magnetoresistive random access memory (MRAM) and reliability. *IEEE International Integrated Reliability Workshop Final Report*, 2003:169, 2003.

[25] I. L. Prejbeanu, W. Kula, K. Ounadjela, R. C. Sousa, O. Redon, B. Dieny, and J. P. Nozieres. Thermally assisted switching in exchange-biased storage layer magnetic tunnel junctions. *IEEE Transactions on Magnetics*, 40:2625, 2004.

[26] J. M. Daughton and A. V. Pohm. Design of Curie point written magnetoresistance random access memory cells. *Journal of Applied Physics*, 93:7304, 2003.

[27] C. Thirion, W. Wernsdorfer, and D. Mailly. Switching of magnetization by nonlinear resonance studied in single nanoparticles. *Nature Materials*, 2:524, 2003.

[28] H. T. Nembach, P. M. Pimentel, S. J. Hermsdoerfer, B. Leven, B. Hillebrands, and S. O. Demokritov. Microwave assisted switching in a Ni81Fe19 ellipsoid. *Applied Physics Letters*, 90:62503, 2007.

[29] L. Berger. Low-field magnetoresistance and domain drag in ferromagnets. *Journal of Applied Physics*, 49:2156, 1978.

[30] L. Berger. Domain drag effect in the presence of variable magnetic field or variable transport current. *Journal of Applied Physics*, 50:2137, 1979.

[31] P. P. Freitas and L. Berger. Observation of s-d exchange force between domain walls and electric current in very thin Permalloy films. *Journal of Applied Physics*, 57:1266, 1985.

[32] C.-Y. Hung and L. Berger. Exchange forces between domain wall and electric current in permalloy films of variable thickness. *Journal of Applied Physics*, 63:4276, 1988.

[33] J. C. Slonczewski. Current-driven excitation of magnetic multilayers. *Journal of Magnetism and Magnetic Materials*, 159:L1, 1996.

[34] L. Berger. Emission of spin waves by a magnetic multilayer traversed by a current. *Physical Review B*, 54:9353, 1996.

[35] M. Tsoi, A. G. M. Jansen, J. Bass, W.-C. Chiang, M. Seck, V. Tsoi, and P. Wyder. Excitation of a magnetic multilayer by an electric current. *Physical Review Letters*, 80:4281, 1998.

[36] J. Z. Sun. Current-driven magnetic switching in manganite trilayer junctions. *Journal of Magnetism and Magnetic Materials*, 202:157, 1999.

[37] J. A. Katine, F. J. Albert, R. A. Buhrman, E. B. Myers, and D. C. Ralph. Current-driven magnetization reversal and spin-wave excitations in Co/Cu/Co pillars. *Physical Review Letters*, 84:3149, 2000.

[38] E. B. Myers, D. C. Ralph, J. A. Katine, R. N. Louie, and R. A. Buhrman. Current-induced switching of domains in magnetic multilayer devices. *Science*, 285:867, 1999.

[39] D. Edwards, F. Federici, J. Mathon, and A. Umerski. Self-consistent theory of current-induced switching of magnetization. *Physical Review B*, 71:054407, 2005.

[40] S. Zhang, P. M. Levy, and A. Fert. Mechanisms of Spin-Polarized Current-Driven Magnetization Switching. *Physical Review Letters*, 88:236601, 2002.

[41] J. C. Sankey, Y.-T. Cui, J. Z. Sun, J. C. Slonczewski, R. A. Buhrman, and D. C. Ralph. Measurement of the spin-transfer-torque vector in magnetic tunnel junctions. *Nature Physics*, 4:67, 2008.

[42] H. Kubota, A. Fukushima, K. Yakushiji, T. Nagahama, S. Yuasa, K. Ando, H. Maehara, Y. Nagamine, K. Tsunekawa, D. D. Djayaprawira, N. Watanabe, and Y. Suzuki. Quantitative measurement of voltage dependence of spin-transfer torque in MgO-based magnetic tunnel junctions. *Nature Physics*, 4:37, 2008.

[43] H. Meng and J.-P. Wang. Composite free layer for high density magnetic random access memory with lower spin transfer current. *Applied Physics Letters*, 89:152509, 2006.

[44] T. Kishi, H. Yoda, T. Kai, T. Nagase, E. Kitagawa, M. Yoshikawa, K. Nishiyama, T. Daibou, M. Nagamine, M. Amano, S. Takahashi, M. Nakayama, N. Shimomura, H. Aikawa, S. Ikegawa, S. Yuasa, K. Yakushiji, H. Kubota, A. Fukushima, M. Oogane, T. Miyazaki, and K. Ando. Lower-current and fast switching of a perpendicular TMR for high speed and high density spin-transfer-torque MRAM. *IEEE International Electron Devices Meeting*, 9:6, 2008.

[45] G. E. W. Bauer, A. H. MacDonald, and S. Maekawa. Spin Caloritronics. *Solid State Communications*, 150:459, 2010.

[46] S. Serrano-Guisan, G. Di Domenicantonio, M. D. Abid, J.-P. Abid, M. Hillenkamp, L. Gravier, J.-P. Ansermet, and C. Félix. Enhanced magnetic field sensitivity of spin-dependent transport in cluster-assembled metallic nanostructures. *Nature Materials*, 5:730, 2006.

[47] O. Tsyplyatyev, O. Kashuba, and V. I. Fal'ko. Giant magnetothermopower and magnetoresistance in metals with embedded ferromagnetic nanoclusters. *Journal of Applied Physics*, 101:132403, 2007.

[48] Y. Takezoe, K. Hosono, A. Takeuchi, and G. Tatara. Theory of spin transport induced by a temperature gradient. *Physical Review B*, 82:094451, 2010.

[49] L. Gravier, S. Serrano-Guisan, F. Reuse, and J.-P. P. Ansermet. Spin-dependent Peltier effect of perpendicular currents in multilayered nanowires. *Physical Review B*, 73:052410, 2006.

[50] W. Lin, M. Hehn, L. Chaput, B. Negulescu, S. Andrieu, F. Montaigne, and S. Mangin. Giant spin-dependent thermoelectric effect in magnetic tunnel junctions. *Nature Communications*, 3:744, 2012.

[51] F. K. Dejene, J. Flipse, and B. J. Van Wees. Spin-dependent Seebeck coefficients of Ni 80Fe 20 and Co in nanopillar spin valves. *Physical Review B*, 86:024436, 2012.

[52] M. Walter, J. Walowski, V. Zbarsky, M. Münzenberg, M. Schäfers, D. Ebke, G. Reiss, A. Thomas, P. Peretzki, M. Seibt, J. S. Moodera, M. Czerner,

M. Bachmann, and C. Heiliger. Seebeck effect in magnetic tunnel junctions. *Nature Materials*, 10:742, 2011.

[53] J. Flipse, F. L. Bakker, A. Slachter, F. K. Dejene, and B. J. Van Wees. Direct observation of the spin-dependent Peltier effect. *Nature Nanotechnology*, 7:166, 2012.

[54] F. L. Bakker, A. Slachter, J.-P. Adam, and B. J. van Wees. Interplay of Peltier and Seebeck Effects in Nanoscale Nonlocal Spin Valves. *Physical Review Letters*, 105:136601, 2010.

[55] M. Hatami, G. E. W. Bauer, Q. Zhang, and P. Kelly. Thermal Spin-Transfer Torque in Magnetoelectronic Devices. *Physical Review Letters*, 99:066603, 2007.

[56] G. E. W. Bauer, S. Bretzel, A. Brataas, and Y. Tserkovnyak. Nanoscale magnetic heat pumps and engines. *Physical Review B*, 81:024427, 2010.

[57] X.-T. Jia and K. Xia. Electric and thermo spin transfer torques in Fe/Vacuum/Fe tunnel junction. *Frontiers of Physics*, 9:768, 2014.

[58] H. Yu, S. Granville, D. P. Yu, and J.-Ph. Ansermet. Evidence for Thermal Spin-Transfer Torque. *Physical Review Letters*, 104:146601, 2010.

[59] L. Fitoussi, F. A. Vetro, C. Caspers, L. Gravier, H. Yu, and J.-P. Ansermet. Linear response to a heat-driven spin torque. *Applied Physics Letters*, 106:162401, 2015.

[60] A. Pushp, T. Phung, C. Rettner, B. P. Hughes, S.-H. Yang, and S. S. P. Parkin.

Giant thermal spin-torqueassisted magnetic tunnel junction switching. *Proceedings of the National Academy of Sciences*, 112:6585, 2015.

[61] X.-T. Jia, K. Xia, and G. E. W. Bauer. Thermal Spin Transfer in Fe-MgO-Fe Tunnel Junctions. *Physical Review Letters*, 107:176603, 2011.

[62] Y. S Gui, N. Mecking, X. Zhou, G. Williams, and C.-M. Hu. Realization of a Room-Temperature Spin Dynamo: The Spin Rectification Effect. *Physical Review Letters*, 98:107602, 2007.

[63] M. Harder, Z. X. Cao, Y. S. Gui, X. L. Fan, and C.-M. Hu. Analysis of the line shape of electrically detected ferromagnetic resonance. *Physical Review B*, 84:054423, 2011.

[64] Y. S. Gui, L. H. Bai, and C.-M. Hu. The physics of spin rectification and its application. *Science China: Physics, Mechanics and Astronomy*, 56:124, 2013.

[65] Z. H. Zhang, L. H. Bai, C.-M. Hu, S. Hemour, K. Wu, X. L. Fan, D. S. Xue, and D. Houssameddine. The tunneling magnetoresistance current dependence on cross sectional area, angle and temperature. *AIP Advances*, 5:037134, 2015.

[66] G. Fuchs, J. Katine, S. Kiselev, D. Mauri, K. Wooley, D. Ralph, and R. Buhrman. Spin Torque, Tunnel-Current Spin Polarization, and Magnetoresistance in MgO Magnetic Tunnel Junctions. *Physical Review Letters*, 96:186603, 2006.

[67] S.-C. Oh, S.-Y. Park, A. Manchon, M. Chshiev, J.-H. Han, H.-W. Lee, J.-E. Lee, K.-T. Nam, Y. Jo, Y.-C. Kong, B. Dieny, and K.-J. Lee. Bias-voltage

dependence of perpendicular spin-transfer torque in asymmetric MgO-based magnetic tunnel junctions. *Nature Physics*, 5:898–902, 2009.

[68] V. S. Pribiag, I. N. Krivorotov, G. D. Fuchs, P. M. Braganca, O. Ozatay, J. C. Sankey, D. C. Ralph, and R. a. Buhrman. Magnetic vortex oscillator driven by d.c. spin-polarized current. *Nature Physics*, 3:498, 2007.

[69] A. Brataas, A. D. Kent, and H. Ohno. Current-induced torques in magnetic materials. *Nature Materials*, 11:372, 2012.

[70] S. Zhang, P. Levy, A. Marley, and S. Parkin. Quenching of Magnetoresistance by Hot Electrons in Magnetic Tunnel Junctions. *Physical Review Letters*, 79:3744, 1997.

[71] S. O. Valenzuela, D. J. Monsma, C. M. Marcus, V. Narayanamurti, and M. Tinkham. Spin polarized tunneling at finite bias. *Physical Review Letters*, 94:196601, 2005.

[72] J. Zhang and R. M. White. Voltage dependence of magnetoresistance in spin dependent tunneling junctions. *Journal of Applied Physics*, 83:6512, 1998.

[73] Z. H. Zhang, Y. S. Gui, L. Fu, X. L. Fan, J. W. Cao, D. S. Xue, P. P. Freitas, D. Houssameddine, S. Hemour, K. Wu, and C.-M. Hu. Seebeck Rectification Enabled by Intrinsic Thermoelectrical Coupling in Magnetic Tunneling Junctions. *Physical Review Letters*, 109:037206, 2012.

[74] Z. H. Zhang, L. H. Bai, X. B. Chen, H. Guo, X. L. Fan, D. S. Xue, D. Houssameddine, and C.-M. Hu. Observation of thermal spin-transfer torque via ferro-

magnetic resonance in magnetic tunnel junctions. *Physical Review B*, 94:064414, 2016.

[75] L. Fu, Z. X. Cao, S. Hemour, K. Wu, D. Houssameddine, W. Lu, S. Pistorius, Y. S. Gui, and C.-M. Hu. Microwave reflection imaging using a magnetic tunnel junction based spintronic microwave sensor. *Applied Physics Letters*, 101:232406, 2012.

[76] S. Hemour, Y. P. Zhao, C. H. P. Lorenz, D. Houssameddine, Y. S. Gui, C.-M. Hu, and K. Wu. Towards low-power high-efficiency RF and microwave energy harvesting. *IEEE Transactions on Microwave Theory and Techniques*, 62:965, 2014.

[77] N. F. Mott and E. A. Davis. *Electronic processes in non-crystalline materials*. (Clarendon Press, 1971).

[78] S. Yuasa, A. Fukushima, T. Nagahama, K. Ando, and Y. Suzuki. High Tunnel Magnetoresistance at Room Temperature in Fully Epitaxial Fe/MgO/Fe Tunnel Junctions due to Coherent Spin-Polarized Tunneling. *Japanese Journal of Applied Physics*, 43:L588, 2004.

[79] S. Yuasa, T. Nagahama, A. Fukushima, Y. Suzuki, and K. Ando. Giant room-temperature magnetoresistance in single-crystal Fe/MgO/Fe magnetic tunnel junctions. *Nature Materials*, 3:868, 2004.

[80] S. S. P. Parkin, C. Kaiser, A. Panchula, P. M. Rice, B. Hughes, M. Samant,

and S.-H. Yang. Giant tunnelling magnetoresistance at room temperature with MgO (100) tunnel barriers. *Nature Materials*, 3:862, 2004.

[81] D. D. Djayaprawira, K. Tsunekawa, M. Nagai, H. Maehara, S. Yamagata, N. Watanabe, S. Yuasa, Y. Suzuki, and K. Ando. 230% room-temperature magnetoresistance in CoFeB/MgO/CoFeB magnetic tunnel junctions. *Applied Physics Letters*, 86:092502, 2005.

[82] S. Yuasa and D. D. Djayaprawira. Giant tunnel magnetoresistance in magnetic tunnel junctions with a crystalline MgO(001) barrier. *Journal of Physics D: Applied Physics*, 40:R337, 2007.

[83] M. Hosomi, H. Yamagishi, T. Yamamoto, K. Bessho, Y. Higo, K. Yamane, H. Yamada, M. Shoji, H. Hachino, C. Fukumoto, H. Nagao, and H. Kano. A novel nonvolatile memory with spin torque transfer magnetization switching: spin-ram. *IEEE International Electron Devices Meeting*, 00:459, 2005.

[84] S. Ikeda, J. Hayakawa, Young M. Lee, F. Matsukura, Y. Ohno, T. Hanyu, and H. Ohno. Magnetic Tunnel Junctions for Spintronic Memories and Beyond. *IEEE Transactions on Electron Devices*, 54:991, 2007.

[85] J. C. Slonczewski. Conductance and exchange coupling of two ferromagnets separated by a tunneling barrier. *Physical Review B*, 39:6995, 1989.

[86] Y. Suzuki and H. Kubota. Spin-torque diode effect and its application. *Journal of the Physical Society of Japan*, 77:31002, 2008.

[87] J. Nogués and I. K. Schuller. Exchange bias. *Journal of Magnetism and Magnetic Materials*, 192:203, 1999.

[88] R. D. Barnard. *Thermoelectricity in metals and alloys.* (Taylor & Francis, 1972).

[89] N. W. Ashcroft and N. D. Mermin. *Solid state physics.* (Saunders College, 1976).

[90] G. E. W. Bauer, E. Saitoh, and B. J. van Wees. Spin caloritronics. *Nature Materials*, 11:391, 2012.

[91] N. Liebing, S. Serrano-Guisan, K. Rott, G. Reiss, J. Langer, B. Ocker, and H. W. Schumacher. Determination of spin-dependent Seebeck coefficients of CoFeB/MgO/CoFeB magnetic tunnel junction nanopillars. *Journal of Applied Physics*, 111:07C520, 2012.

[92] L. Onsager. Reciprocal relations in irreversible processes. I. *Physical Review*, 37:405, 1931.

[93] V. K. Arkad'yev. Absorption of electric waves in parallel wires. *Russian Journal of Physical Chemistry*, 44:165, 1912.

[94] C. Kittel. Interpretation of anomalous larmor frequencies in ferromagnetic resonance experiment. *Physical Review*, 71:270, 1947.

[95] C. Kittel. On the theory of ferromagnetic resonance absorption. *Physical Review*, 73:155, 1948.

[96] J. Xiao, A. Zangwill, and M. D. Stiles. Macrospin models of spin transfer dynamics. *Physical Review B*, 72:014446, 2005.

[97] A. A. Kovalev, G. E. W. Bauer, and A. Brataas. Current-driven ferromagnetic resonance, mechanical torques, and rotary motion in magnetic nanostructures. *Physical Review B*, 75:014430, 2007.

[98] I. Theodonis, N. Kioussis, A. Kalitsov, M. Chshiev, and W. H. Butler. Anomalous bias dependence of spin torque in magnetic tunnel junctions. *Physical Review Letters*, 97:237205, 2006.

[99] C. Heiliger and M. D. Stiles. Ab initio studies of the spin-transfer torque in magnetic tunnel junctions. *Physical Review Letters*, 100:186805, 2008.

[100] A. Manchon, N. Ryzhanova, A. Vedyayev, M. Chschiev, and B. Dieny. Description of current-driven torques in magnetic tunnel junctions. *Journal of Physics: Condensed Matter*, 20:145208, 2008.

[101] M. Wilczyński, J. Barnaś, and R. Świrkowicz. Free-electron model of current-induced spin-transfer torque in magnetic tunnel junctions. *Physical Review B*, 77:054434, 2008.

[102] J. Xiao, G. E. W. Bauer, and A. Brataas. Spin-transfer torque in magnetic tunnel junctions: Scattering theory. *Physical Review B*, 77:224419, 2008.

[103] J. Z. Sun and D. C. Ralph. Magnetoresistance and spin-transfer torque in magnetic tunnel junctions. *Journal of Magnetism and Magnetic Materials*, 320:1227, 2008.

[104] D. C. Ralph and M. D. Stiles. Spin transfer torques. *Journal of Magnetism and Magnetic Materials*, 320:1190, 2008.

[105] S. Parkin, X. Jiang, C. Kaiser, A. Panchula, K. Roche, and M. Samant. Magnetically engineered spintronic sensors and memory. *Proceedings of the IEEE*, 91:661, 2003.

[106] R. Meservey and P. M. Tedrow. Spin-polarized electron tunneling. *Physics Reports*, 238:173, 1994.

[107] A. Bose, A. K. Shukla, K. Konishi, S. Jain, N. Asam, S. Bhuktare, H. Singh, D. D. Lam, Y. Fujii, S. Miwa, Y. Suzuki, and A. A. Tulapurkar. Observation of thermally driven field-like spin torque in magnetic tunnel junctions. *Applied Physics Letters*, 109:032406, 2016.

[108] B. Heinrich, Y. Tserkovnyak, G. Woltersdorf, A. Brataas, R. Urban, and G. E. W. Bauer. Dynamic exchange coupling in magnetic bilayers. *Physical Review Letters*, 90:187601, 2003.

[109] N. H. G. Grenda, P. Hyde, Y. S. Gui, M. P. Wismayer, J. D. a Jung, C.-M. Hu, B. W. Southern, and K.-W. Lin. Angular dependence of ferromagnetic resonance measurements in exchange coupled Ni80Fe20/NiO bilayers. *Journal of Physics D: Applied Physics*, 46:205002, 2013.

[110] H. J. Juretschke. Dc detection of spin resonance in thin metallic films. *Journal of Applied Physics*, 34:1223, 1963.

[111] W. G. Egan and H. J. Juretschke. DC Detection of Ferromagnetic Resonance in Thin Nickel Films. *Journal of Applied Physics*, 34:1477, 1963.

[112] M. V. Costache, S. M. Watts, M. Sladkov, C. H. Van Der Wal, and B. J. Van Wees. Large cone angle magnetization precession of an individual nanopatterned ferromagnet with dc electrical detection. *Applied Physics Letters*, 89:232115, 2006.

[113] Y. S. Gui, S. Holland, N. Mecking, and C.-M. Hu. Resonances in ferromagnetic gratings detected by microwave photoconductivity. *Physical Review Letters*, 95:056807, 2005.

[114] J. Cao, J. Kanak, T. Stobiecki, P. Wisniowski, and P. P. Freitas. Effect of buffer layer texture on the crystallization of CoFeB and on the tunnel magnetoresistance in MgO based magnetic tunnel junctions. *IEEE Transactions on Magnetics*, 45:3464, 2009.

[115] J. C. Slonczewski. Currents, torques, and polarization factors in magnetic tunnel junctions. *Physical Review B*, 71:024411, 2005.

[116] J. C. Slonczewski and J. Z. Sun. Theory of voltage-driven current and torque in magnetic tunnel junctions. *Journal of Magnetism and Magnetic Materials*, 310:169, 2007.

[117] J. S. Moodera, L. R. Kinder, T. M. Wong, and R. Meservey. Large magnetoresistance at room temperature in ferromagnetic thin film tunnel junctions. *Physical Review Letters*, 74:3273, 1995.

[118] W. J. Gallagher, S. S. P. Parkin, Y. Lu, X. P. Bian, A. Marley, K. P. Roche, R. A. Altman, S. A. Rishton, C. Jahnes, T. M. Shaw, and G. Xiao. Microstructured magnetic tunnel junctions (invited). *Journal of Applied Physics*, 81:3741, 1997.

[119] W. F. Brinkman, R. C. Dynes, and J. M. Rowell. Tunneling conductance of asymmetrical barriers. *Journal of Applied Physics*, 41:1915, 1970.

[120] A. A. Kovalev, G. E. W. Bauer, and A. Brataas. Perpendicular spin valves with ultrathin ferromagnetic layers: Magnetoelectronic circuit investigation of finite-size effects. *Physical Review B*, 73:054407, 2006.

[121] T. Taniguchi, S. Yakata, H. Imamura, and Y. Ando. Penetration depth of transverse spin current in ferromagnetic metals. *IEEE Transactions on Magnetics*, 44:2636, 2014.

[122] D. X. Wang, C. Nordman, J. M. Daughton, Z. H. Qian, and J. Fink. 70% TMR at room temperature for SDT sandwich junctions with CoFeB as free and reference layers. *IEEE Transactions on Magnetics*, 40:2269, 2004.

[123] T. Miyazaki and N. Tezuka. Giant magnetic tunneling effect in Fe/Al2O3/Fe junction. *Journal of Magnetism and Magnetic Materials*, 139:L231, 1995.

[124] R. Stratton. Volt-current characteristics for tunneling through insulating films. *Journal of Physics and Chemistry of Solids*, 23:1177, 1962.

[125] K. Uchida, S. Takahashi, K. Harii, J. Ieda, W. Koshibae, K. Ando, S. Maekawa, and E. Saitoh. Observation of the spin Seebeck effect. *Nature*, 455:778, 2008.

[126] S. Y. Huang, W. G. Wang, S. F. Lee, J. Kwo, and C. L. Chien. Intrinsic Spin-Dependent Thermal Transport. *Physical Review Letters*, 107:216604, 2011.

[127] J.-C. Le Breton, S. Sharma, H. Saito, S. Yuasa, and R. Jansen. Thermal spin current from a ferromagnet to silicon by Seebeck spin tunnelling. *Nature*, 475:82, 2011.

[128] N. Liebing, S. Serrano-Guisan, K. Rott, G. Reiss, J. Langer, B. Ocker, and H. W. Schumacher. Tunneling magnetothermopower in magnetic tunnel junction nanopillars. *Physical Review Letters*, 107:1, 2011.

[129] X. B. Chen, D. P. Liu, W. H. Duan, and H. Guo. Photon-assisted thermoelectric properties of noncollinear spin valves. *Physical Review B*, 87:85427, 2013.

[130] J.-P. Jan. Galvamomagnetic and Thermomagnetic Effects in Metals. *Solid State Physics*, 5:1, 1957.

[131] D. M. Pozar. *Microwave Engineering*. (Wiley, 2011), 4th ed.

[132] E. McCann and V. I. Fal'Ko. Magnetothermopower and magnon-assisted transport in ferromagnetic tunnel junctions. *Applied Physics Letters*, 81:3609, 2002.

[133] M. Czerner, M. Bachmann, and C. Heiliger. Spin caloritronics in magnetic tunnel junctions: Ab initio studies. *Physical Review B*, 83:132405, 2011.

[134] C. Shang, J. Nowak, R. Jansen, and J. Moodera. Temperature dependence of magnetoresistance and surface magnetization in ferromagnetic tunnel junctions. *Physical Review B*, 58:R2917, 1998.

[135] A. A. Tulapurkar, Y. Suzuki, A. Fukushima, H. Kubota, H. Maehara, K. Tsunekawa, D. D. Djayaprawira, N. Watanabe, and S. Yuasa. Spin-torque diode effect in magnetic tunnel junctions. *Nature*, 438:339, 2005.

[136] J. Faure-Vincent, C. Tiusan C. Bellouard, E. Popova, M. Hehn, F. Montaigne, and A. Schuhl. Interlayer magnetic coupling interactions of two ferromagnetic layers by spin polarized tunneling. *Physical review letters*, 89:107206, 2002.

[137] J. C. Leutenantsmeyer, M. Walter, V. Zbarsky, M. Münzenberg, R. Gareev, K. Rott, A. Thomas, G. Reiss, P. Peretzki, H. Schuhmann, M. Seibt, M. Czerner, and Heiliger. C. Parameter Space for Thermal Spin-Transfer Torque. *Spin*, 3:1350002, 2013.

[138] N. Mecking, Y. S. Gui, and C.-M. Hu. Microwave photovoltage and photoresistance effects in ferromagnetic microstrips. *Physical Review B*, 76:224430, 2007.